



Cavity electro-optics in thin-film lithium niobate

Citation

Holzgrafe, Jeffrey Cole. 2022. Cavity electro-optics in thin-film lithium niobate. Doctoral dissertation, Harvard University Graduate School of Arts and Sciences.

Permanent link

<https://nrs.harvard.edu/URN-3:HUL.INSTREPOS:37372220>

Terms of Use

This article was downloaded from Harvard University's DASH repository, and is made available under the terms and conditions applicable to Other Posted Material, as set forth at <http://nrs.harvard.edu/urn-3:HUL.InstRepos:dash.current.terms-of-use#LAA>

Share Your Story

The Harvard community has made this article openly available.
Please share how this access benefits you. [Submit a story](#).

[Accessibility](#)

HARVARD UNIVERSITY
Graduate School of Arts and Sciences



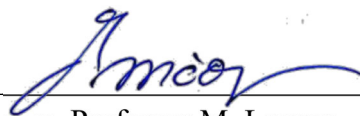
DISSERTATION ACCEPTANCE CERTIFICATE


The undersigned, appointed by the

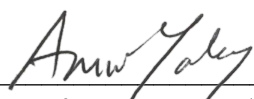
Harvard John A. Paulson School of Engineering and Applied Sciences
have examined a dissertation entitled:

“Cavity electro-optics in thin-film lithium niobate”

presented by: Jeffrey Cole Holzgrafe

Signature  _____
Typed name: Professor M. Loncar

Signature  _____
Typed name: Professor E. Hu

Signature  _____
Typed name: Professor A. Yacoby

April 15, 2022

Cavity electro-optics in thin-film lithium niobate

A dissertation presented

by

Jeffrey Cole Holzgrafe

to

The John A. Paulson School of Engineering and Applied Sciences

in partial fulfillment of the requirements

for the degree of

Doctor of Philosophy

in the subject of

Applied Physics

Harvard University

Cambridge, Massachusetts

April 2022

©2022 – Jeffrey Cole Holzgrafe
All rights reserved.

Cavity electro-optics in thin-film lithium niobate

Abstract

Quantum networks of superconducting qubits linked by optical channels could leverage both the quantum information processing capabilities of superconducting circuits and the long communication distances provided by optical photons. Such networks would require high efficiency, low noise, and wide bandwidth transducers between microwave and optical frequencies. Transducers based on the Pockels electro-optic (EO) effect are particularly promising in this application for their direct conversion mechanism and potential for strong performance. EO transducers could also be used for sensitive optical modulators and low-noise detection of microwave and millimeter-wave signals.

This dissertation presents recent work to create cavity EO transducers in thin-film lithium niobate, an integrated photonics platform that provides low optical loss and strong EO coupling. I first describe the theory of cavity electro-optics and how it can be used to generate high-efficiency transduction between microwave and optical fields. An initial device is presented and characterized, demonstrating per-photon on-chip transduction efficiencies of up to $(2.7 \pm 0.3) \times 10^{-5}$.

A key benefit of the device described here, which is based on photonic molecule modes, is the ability to use a static electro-optic bias to trim the transducer into resonance. However, we find the migration of free carriers in thin-film lithium niobate reduces the EO response of the device to static fields, making such trimming ineffective. This carrier migration is a key challenge for enabling the promise of low-power electro-optics provided by thin-film lithium niobate devices. I characterize the low-frequency electro-optic response, which suggests that conduction occurs on the etched surface of lithium niobate. I show how this conduction can be reduced – and low-frequency EO performance improved – by changing the electrode design and annealing the devices.

Following this, I describe the design and initial characterization of an improved transducer device. Finally, I describe a scheme by which even relatively low-efficiency transducers could be used to generate remote entanglement using an optically heralding scheme. Demonstration of such a system appears possible with current devices, suggesting that small optically-mediated quantum networks of superconducting qubits may be feasible soon.

Contents

Title page	i
Copyright page	ii
Abstract	iii
Table of contents	iv
Author list	vi
Listing of figures	vii
Acknowledgments	ix
1 Introduction	1
1.1 Quantum transducers between microwave and optical fields	4
1.2 Cavity electro-optics	5
1.3 Thin-film lithium niobate	8
1.4 Dissertation outline	10
2 Theory of cavity electro-optics	12
2.1 Hamiltonian description of cavity electro-optics	13
2.2 Open-system description of cavity electro-optics	25
3 Microwave-to-optical transduction using cavity electro-optics in thin-film lithium niobate	36
3.1 Introduction	36
3.2 Device design and characterization	37
3.3 Microwave to optical transduction	40
3.4 Discussion	46
4 Charge carrier effects in thin-film lithium niobate	49
4.1 Measurement setup	50
4.2 Dielectric relaxation	52
4.3 Temperature dependence	55
4.4 Electrode interface variation	58
4.5 Annealing	60

4.6	Discussion and Conclusion	61
5	Preliminary characterization of an optimized transducer	65
5.1	Transducer optimization	67
5.2	Bias response under optical pumping	71
5.3	Characterization of thermal microwave noise	72
5.4	Discussion	76
6	Outlook: optically heralded generation of remote microwave entanglement	78
6.1	Heralded generation of remote microwave entanglement using cavity electro-optics	79
6.2	Future work	85
	Appendix A Definitions	89
A.1	Acronyms	89
A.2	Mathematical notation	90
	Appendix B Additional theory results	92
B.1	Bidirectional resonator coupling	92
B.2	Double resonance transduction	93
	Appendix C Microwave resonators	96
C.1	Capacitive coupling	96
C.2	Niobium nitride resonator of Chapter 3	99
	Appendix D Experimental methods	102
D.1	Setup for Chapter 3	102
D.2	Device packaging and optical coupling	104
D.3	Device fabrication	105
	References	124

Author list

Portions of Chapter 2 are adapted from the supplemental material to:

J. Holzgrafe, N. Sinclair, N. Sinclair, D. Zhu, D. Zhu, A. Shams-Ansari, M. Colangelo, Y. Hu, Y. Hu, M. Zhang, M. Zhang, K. K. Berggren, and M. Lončar, "Cavity electro-optics in thin-film lithium niobate for efficient microwave-to-optical transduction," *Optica* 7, 1714–1720 (2020).

The content of Chapter 3 largely appeared in:

J. Holzgrafe, N. Sinclair, N. Sinclair, D. Zhu, D. Zhu, A. Shams-Ansari, M. Colangelo, Y. Hu, Y. Hu, M. Zhang, M. Zhang, K. K. Berggren, and M. Lončar, "Cavity electro-optics in thin-film lithium niobate for efficient microwave-to-optical transduction," *Optica* 7, 1714–1720 (2020).

The content of Chapter 4 includes portions of the following manuscript in preparation:

E. Puma, J. Holzgrafe, R. Cheng, H. Warner, A. Shams-Ansari, R. Shankar, and M. Lončar, "Examining the sub-megahertz frequency response of electro-optic phase modulators in X-cut thin film lithium niobate on insulator," (2022).

The content of Chapter 6 includes portions of the following publications:

Matthew J. Reagor, Jeffrey Cole Holzgrafe, and Marko Loncar, "Photonic Quantum Networking for Large Superconducting Qubit Modules," U.S. patent application.

S. Krastanov, H. Raniwala, J. Holzgrafe, K. Jacobs, M. Lončar, M. J. Reagor, and D. R. Englund, "Optically Heralded Entanglement of Superconducting Systems in Quantum Networks," *Phys. Rev. Lett.* 127, 040503 (2021).

Listing of figures

1.1	Comparison between single and double optical mode transduction schemes. . . .	6
1.2	Comparison between a traditional waveguide in bulk LN and a ridge waveguide in thin film lithium niobate.	9
2.1	The normalized dependence of the hybridization parameters on the optical mode detuning.	18
2.2	The penalty for using non-degenerate modes as a function of the fractional change in the mode splitting compared to the degenerate case.	19
2.3	Power transmission for two hybrid modes with frequency splitting of 2 and internal and external coupling rates of 0.2 in normalized frequency units.	29
2.4	Impact of cooperativity and detuning on conversion efficiency for red side pumping.	32
2.5	Calculated EIT spectra for different system parameters	33
3.1	Design and optical characterization of a superconducting cavity electro-optic transducer on thin-film lithium niobate.	38
3.2	Piezoelectric loss in thin-film lithium niobate.	41
3.3	Detuning dependence of microwave-to-optical photon transduction.	42
3.4	Power dependence of microwave-to-optical photon transduction.	45
4.1	Characterization setup for low-frequency electro-optic response in thin-film lithium niobate.	51
4.2	Measurement and modeling of low-frequency electro-optic response in thin-film lithium niobate.	52
4.3	Device characterization at cryogenic temperatures.	56
4.4	Low-frequency response for etched-cladding devices.	59
4.5	Low-frequency response of annealed devices.	60
4.6	Atomically resolved transmission electron microscope image of the LN etch interface.	63
5.1	Design of coupled adiabatic racetrack resonators.	66
5.2	Design of a side-contact electrode geometry for the optimized transducer.	69
5.3	Characterization of optical and microwave resonators in an improved transducer.	70
5.4	Comparison of the photonic link gain during bias voltage sweep of two different devices.	71
5.5	Measurement of thermal microwave noise.	73

6.1	Remote entanglement of superconducting qubits using an optical channel.	80
6.2	Performance of an on-chip integrated filter array based on tunable add/drop ring resonators.	83
B.1	Comparison of unidirectional and bidirectional coupling to a microwave mode. .	92
C.1	Capacitive coupling of microwave resonators in a high-density transducer layout.	97
C.2	Dependence of microwave resonator loss on resonance frequency.	100
C.3	Power dependent microwave transmission.	101
D.1	Simplified diagram of the transduction measurement setup.	103
D.2	Setup for packaging and mounting device from Chapter 5.	106

Acknowledgments

I want to express my immense gratitude to Marko Lončar for being such an excellent advisor. I first met Marko almost eight years ago for a summer internship in the lab, when the program director introduced me and said "I think you're really going to mesh with Marko's approach." After two summers, a "sabbatical" in the UK, and five more years working in Marko's group, I guess she must have been right! Marko's emphasis on both a deep understanding of physical law and the sometimes ineffable knowledge of craftsmanship is a lesson I will take to the rest of my career. This, combined with his sometimes wild dreams and constant enthusiasm, has created a wonderful environment where curiosity and collaboration can direct our work. Besides these qualities, Marko has been an unfailingly supportive presence throughout my time here. He's been patient, enthusiastic, and invested in all the details – inside the lab and out, highs and lows– along my journey. I will always cherish the lessons I've learned from Marko.

I am also grateful to my other committee members – Evelyn Hu and Amir Yacoby – for their advice and careful feedback on my dissertation. Additionally, the close ties between our research groups have been invaluable when we need to borrow a cup of TMAH from a neighbor.

This dissertation would have been possible without the support and wisdom of my outstanding colleagues. I would particularly like to thank all the many members of the Lončar group over many years.

I was lucky to have many excellent senior students and postdoctoral fellows to show me the ropes. I-Chun Huang and Srujan Meesala were my first mentors in the lab as an undergraduate and I will always appreciate the patience and support they showed when teaching me new skills and ideas. Cheng Wang is responsible for a great deal of the excitement in the field of thin-film lithium niobate devices. Mian Zhang initiated the cavity electro-optics project and was a wonderful resource as I first started learning about photonics. Mian's hard work and persistence showed me the value of rapid iteration when faced with problems that seem almost intractable. Christian Riemer is living evidence that scientific productivity and time spent chatting over coffee are directly correlated – I am grateful for the many things I learned from those conversations. Like many others in our lab, I owe a great deal to Amirhassan Shams-Ansari for his patient instruction in both the physics and metaphysics of device fabrication. Amir's experience and knowledge of seemingly every tool and process were essential to the work described here. Perhaps most important, his positive attitude was a huge boon to office levity. Boris Desiatov seemed to possess both a mind and a desk drawer that contained everything there was worth having, and I am grateful for his generosity with both. Linbo Shao was incredibly generous with his knowledge of cryogenics and electronics. Although it seemed like every idea Mengjie Yu and I talked about turned out less promising than we initially hoped, I am grateful for those chances to learn from her huge experience in front of a whiteboard.

Neil Sinclair and Di Zhu were the post-docs who most directly supported the work here, and I'm not sure how I can thank them properly. Neil's knowledge of quantum optics and experimental skills are perhaps only surpassed by his endless enthusiasm for our field. His friendly resolve and support were essential during some of the harder setbacks that occurred in the course of this work. Everyone in our lab knows that it is no exaggeration to say Di Zhu has every quality one could ask for in a post-doc. His work ethic, humility, and ability to learn just about anything made him an essential resource for many in the lab. During the coronavirus lockdowns when I was one of the few from our group permitted to work in the cleanroom, Di stepped up and made a huge contribution to this project by leading the measurement efforts in the lab.

I also want to thank the many colleagues I've been able to work with who made coming into the lab (at least when we were allowed to!) a joy, including Hana Warner, David Barton III, Eric Puma, Rebecca Cheng, Yaowen Hu, Graham Joe, Smarak Maity, Dylan Renaud, Benjamin Pingault, Soumya Ghosh, Sophie Ding, Michelle Chalupnik, Eliza Cornell, Cleaven Chia, Bart Machielse, Daniel Ramos, Michael Haas, Matthew Ye, and Chen Jie Xin. Without exception they were always ready and happy to help, teach, learn and brainstorm. The problems we all work on are difficult, but the support of so many talented people makes it a pleasure. In particular, I want to thank Hana, David, and Eric for making the many hours spent together in the lab and the cleanroom both enlightening and enjoyable.

We are lucky to have a kind and supportive administrative staff, including Kathleen Masse, Jeff Derr, Stacia Zatsiorsky, and Adam Gillis. From truly Herculean efforts over several months to fix the paperwork on a lost package, to immediately taking care of mysterious flooding that threatened our equipment, and, on one notable occasion, helping me ambush Marko, they have been essential to this work.

After experiences at other institutions, coming to Harvard has shown me how important skilled technical staff are to productive scientific work. The staff members in the Center for Nanoscale Systems, the Physics machine shop, and the electronic shop have been an excellent source of knowledge and more than a little wisdom. Despite the best efforts of students (including me!) to find creative new ways to break things, they do a great job keeping their domains in working order. I particularly want to thank Mughees Kahn, Jiangdong Deng, Ed Macomber, Steve Paolini, David LaFleur, Jason Tresback, Jim MacArthur, Stan Cotreau, and Andrew Dimambro.

Getting to know and work with a wide range of collaborators outside our lab has been one of the highlights of my experience. I am grateful to Matthew Reagor, Norman Lippok, Ben Vackoc, Marco Colangelo, Karl Berggren, and Jack Yanjie Qiu for sharing their expertise and excitement.

I also want to thank the following funding agencies for their financial support of the work described here, as well as the philanthropic organizations and American people who support these programs in turn: National Science Foundation (NSF), National Institutes of Health (NIH), Air Force Research Labs (AFRL), and Harvard University.

My family and friends were an invaluable source of support and occasional distraction while completing this work. In particular, I want to thank my parents Don and Lisa Holzgrafe for teaching me what focus looks like and giving me the chance to follow my passion, as well as my brother Matthew for keeping me grounded.

Finally and most importantly, I want to thank my incredible husband Brendan Quinlivan for the love and encouragement he shares with me every day.

Chapter 1

Introduction

Light has long been seen as an excellent tool for transmitting information over long distances. Aeschylus, writing in 458 BCE, uses the lighting of a signal flare to convey the fall of Troy to his characters in the first few lines of the *Orestia*. Since then, optical communication technology has advanced substantially and today serves as the backbone of our information society. In the *Orestia*, just one bit of information could be transmitted from the battlefield to the palace, presumably at great cost in manpower and firewood. Today, lasers, modulators, optical fibers, and photodetectors transmit roughly 500 terabytes of internet traffic every second [1].

Light has several attractive properties that have led to its wide adoption as a carrier of information. The high speed at which light moves enables low latency even for large networks. Light can be guided for long distances in low-cost and small-diameter optical fibers [2, 3]. The long attenuation lengths available in optical fibers (roughly 20 km at wavelengths near 1550 nm) mean information can be transmitted over long distances with minimal power and few repeater stages [4]. In free space, optical power falls off only polynomially with distance¹, enabling even longer distance line-of-sight connections [5]. The high carrier frequency of light (e.g. 200 THz at a wavelength of 1550 nm) allows for exceptionally wide communication bandwidth. Wavelength division multiplexing techniques [6] can provide a communication

¹At least, on a clear day or in vacuum.

bandwidth of several terahertz through a single optical fiber. The high optical frequency also makes thermal noise negligible at room temperature, allowing the creation of low noise, nearly quantum-limited optical amplifiers such as erbium-doped fibers [7].

As the field of quantum information science has developed, it has become clear that many of these considerations would also apply to future quantum networks. Quantum networks comprise a system of nodes and interconnects capable of distributing entanglement across the network [8, 9]. There are currently two primary motivations for the development of quantum networks:

First, such networks could be used to perform quantum cryptographic communication – which can provide security guarantees from interception – over long distances and large scales [10–12]. Quantum cryptography relies on the no-cloning theorem, which states that arbitrary quantum states cannot be faithfully copied [13]. This restriction ensures that, for a well-designed protocol, an interceptor can be identified if quantum states are used to communicate. Quantum cryptography was first proposed almost 40 years ago [14] and has seen rapid development since then. Today, quantum cryptography systems are commercially available [15]. To ensure security, weak single-photon-scale signals must be used without amplifier-based repeaters [16]. This requirement means that the communication rates achievable using the relatively simple repeaterless systems currently available suffer greatly from loss in the channel, limiting communication range. This range can be extended using networks of classical nodes [16], but this weakens the security guarantees as the nodes must be trusted. Alternatively, quantum networks possessing long-lived memories could be used for long-distance quantum communication without requiring trusted nodes. In such a quantum repeater system, entanglement is distributed from node to node until two distant nodes use the entanglement resource to perform quantum communication [10, 11]. Although errors would compound over such a network, entanglement distillation techniques can be used to compensate for such errors [17].

Second, quantum networks are being explored as a potentially practical vision for scaling quantum computers [9, 18–20]. In this vision, well-characterized and relatively small quantum

nodes would be combined into a high-connectivity network to perform distributed quantum computing. This architecture could provide many of the same extensibility and reliability benefits as modern classical distributed computing techniques.

Optical frequencies are useful for quantum networks for several reasons above and beyond those described earlier for classical networks. The negligible thermal noise at room temperature means single-quanta level signals can be faithfully transmitted across an optical channel [21]. The existence of excellent high-efficiency, fast rise-time single-photon detectors with low dark counts – such as superconducting nanowire single-photon detectors [22] – enables effective heralding protocols for creating quantum networks [11].

For these reasons, a great deal of work has been done to develop methods and devices to interface between photons and long-lived quantum memories such as atomic and nuclear spins. This research direction has led to many valuable advances in recent years, including the demonstration of nonclassical correlations [23], entanglement [21] and gates [24] between photons and atomic degrees of freedom, the use of optical modes to generate remote entanglement between memories [25], a loop-hole free test of Bell’s inequality [26], and memory-enhanced quantum communication [12]. Several promising quantum technology platforms have been investigated for this purpose, including quantum dots [27], neutral atoms [28], atomic ensembles [29], ions [19], and solid-state defects [30].

However, many otherwise promising quantum technologies do not provide direct coupling to optical fields. In particular, superconducting quantum devices have shown rapid advancement, including improvements in coherence properties [31], the demonstration of quantum supremacy [32], and quantum error correction that can improve qubit coherence times [33]. These advancements, as well as the facts that superconducting qubits operate at easy-to-use microwave frequencies and are formed from potentially scalable electrical circuits, have created a great deal of interest in building systems with larger numbers of superconducting qubits [34–36]. However, it is difficult to shrink individual circuit elements like microwave resonators smaller than millimeter-scale. This density restriction limits the scale of superconducting quantum processors that can be made on a single chip.

To create larger-scale superconducting quantum devices, some form of network is likely required. The most natural way to create such a network would be to take advantage of the coupling between superconducting qubits and microwave photons and use microwave-frequency channels. Significant progress has been made toward this goal in recent years [37–39]. However, the microwave channels must be cooled below 100 mK to prevent thermal noise from interfering with the communication. This makes the channels bulky, expensive, and infeasible for long-distance applications.

1.1 Quantum transducers between microwave and optical fields

Quantum interconnects based on optical links have been explored as an alternative for creating superconducting qubit quantum networks, motivated by the previously discussed benefits of optical fields, including long attenuation lengths, negligible thermal noise, and high bandwidth [40]. Connecting optical networks with superconducting quantum technologies requires a quantum transducer capable of converting single photons between microwave and optical frequencies [41, 42]. Such a transducer offers a promising route toward both large-scale distributed superconducting quantum networks [43] and the scaling of superconductor quantum processors beyond single cryogenic environments [19, 20].

Besides the quantum networking applications described above, single-photon microwave-to-optical transduction can be used to create high-efficiency optical modulators [44], low-noise detectors for microwave or millimeter-wave fields [45], and multiplexed readout of cryogenic electronics [46].

An ideal quantum transducer performs a unitary transformation on microwave and optical modes. Practically, this level of performance implies efficiency approaching 100%, low noise, and enough bandwidth for the desired signals [47]. In early work, transducers based on mechanical and optical resonators were proposed for interfacing with superconducting qubits [48]. Since then, a wide variety of creative transduction schemes have been explored in the search

for high efficiency and low noise. Comprehensive reviews of these explorations can be found elsewhere [41, 42, 49]. Some of the most promising approaches have used electro- or piezo-optomechanical devices [50–61], nonlinear crystals that display a Pockels electro-optic (EO) effect [62–67], trapped atoms [68, 69], crystals doped with rare-earth ions [70, 71], and opto-magnonic devices [72]. Although near-unitary performance has proved challenging to realize, the optomechanical approach has been used to demonstrate bidirectional operation [50], high efficiency [51, 58], and noise levels below a single photon [59, 73]. Optomechanical devices provide strong interactions with both microwave and optical fields, but their reliance on an intermediate mechanical mode in the transduction process creates several challenges for near-unitary operation. The low frequency (MHz) mechanical modes used in membrane electro-optomechanical transducers [50, 51] result in strong thermal noise even at temperatures below 100 mK, and make the transducers susceptible to low-frequency technical noise sources. Although piezo-optomechanical devices that use GHz frequency mechanical modes [52–61] are not susceptible to these issues, such devices display optical-pump-induced heating of the mechanical resonator that adds to the transduction noise. This heating is difficult to avoid in piezo-optomechanical devices due to their colocalization of optical and mechanical modes, as well as their suspended nature that leads to high thermal resistance [74]. Pump-induced heating can be addressed using pulsed-pump schemes [75], but this approach requires trade-offs between efficiency, noise, and repetition rate [59, 73].

1.2 Cavity electro-optics

The desire for lower noise, higher efficiency, and faster repetition rates has motivated research into cavity-based EO transducers [62–66, 76–79], in which microwave fields directly modulate light using an EO nonlinearity of the host material. Cavity EO devices were originally developed for compact optoelectronic oscillators to generate low-noise microwave signals [62, 80]. Their use in quantum technologies is motivated by several factors [76, 77]. First, the direct conversion mechanism avoids any intermediate stages, reducing device complexity and elim-

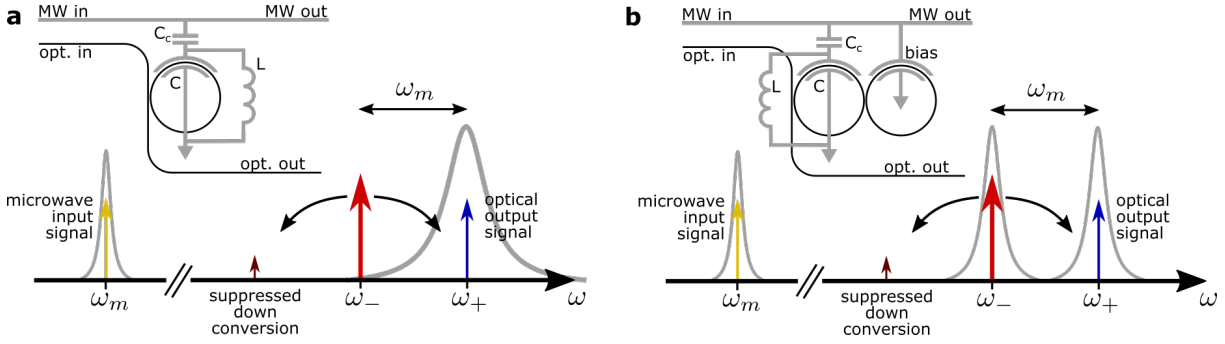


Figure 1.1: Comparison between single and double optical mode transduction schemes. (a) Single optical mode transduction. A microwave LC oscillator modulates an optical pump at ω_- , generating an upconverted optical signal at ω_+ . (b) Double optical mode transduction. By using hybrid optical modes formed by evanescent coupling between two ring resonators, the optical pump field can be resonantly enhanced while still providing for suppressed down conversion.

inating some sources of loss and noise. Second, these devices can have spatially separated microwave and optical resonators with low thermal thermal resistance to the cryostat base temperature, potentially offering much lower optically-induced thermal noise than suspended devices based on colocalized optical and mechanical modes.

Figure 1.1 shows two simple cavity EO devices. In Figure 1.1a, a microwave LC resonator gates an optical resonator made from a Pockels EO material. This gating creates a parametric interaction between the two resonators: a voltage on the microwave resonator induces a shift in the resonance frequency of the optical mode. If a microwave frequency input signal is sent into the device resonant with the microwave mode, an optical pump signal can be modulated. The upconversion of optical light can be resonantly enhanced by placing the optical pump on the so-called "red sideband" of the optical mode (i.e. one microwave frequency below the optical resonance frequency, ω_- in the figure). This upconversion is accomplished by the addition of two photons at the microwave and optical pump frequencies. It represents a conversion of the microwave input field to optical frequencies. The red sideband pump configuration also has the benefits of suppressing optical downconversion, eliminating spontaneous parametric downconversion that can act as a noise process in some schemes, and enabling conversion of the microwave field into a single optical tone.

This conversion process can be made highly efficient if the interaction between the microwave and optical modes is large, the loss rates of the modes are weak, and the optical

pump is strong so that one microwave photon has many possible optical photons to interact with. The key figure of merit is the cooperativity

$$C = \frac{4g_0^2 n_{\text{pump}}}{\kappa_o \kappa_m}, \quad (1.1)$$

where g_0 is the single-photon interaction rate that quantifies the jitter of the optical resonance frequency induced by vacuum fluctuations in the microwave resonator, n_{pump} is the number of pump optical photons in the optical resonator, and $\kappa_{o,m}$ are the optical and microwave mode loss rates (see Chapter 2 for more details). Typical values of the key device rates for current cavity EO devices such as those described here are $\{g_0, \kappa_o, \kappa_e\} = \{1 \text{ kHz}, 100 \text{ MHz}, 10 \text{ MHz}\}$. These rates imply that a double-resonance approach like that shown in Fig. 1.1a would require large optical pump power of order 1 W to reach near-unity efficiency ($C = 1$), which makes compatibility with the cryogenic environment needed for superconducting qubits difficult.

Luckily, the double optical cavity design shown in Figure 1.1b can significantly enhance the circulating optical pump power by allowing the pump field to be resonantly enhanced along with the upconverted field. Double optical cavity systems have been explored in other parametrically coupled resonator systems such as optomechanics and optical parametric oscillators [81, 82]. In cavity EO devices, several methods have been investigated for double optical cavity transduction. In some early investigations, neighboring longitudinal modes separated by one free spectral range (FSR) were used, but this approach provides little tunability of the splitting between optical modes, and the existence of another longitudinal mode near the downconversion frequency provides limited downconversion suppression [62]. In our devices, we use instead hybrid optical modes formed by two evanescently coupled ring resonators [82, 83]. Importantly, the optical mode splitting can be tuned easily by applying a DC voltage across a bias capacitor on one of the ring resonators. This means that small fabrication-induced variations in the mode frequencies can be overcome using active tuning without any static power dissipation.

Previous EO transducers have used bulk lithium niobate [62–64], aluminum nitride [66] and

hybrid silicon-organic [79] platforms. Recent work on EO transducers has shown promise for low-noise operation due to the efficient cooling of microwave modes in these systems [84–86]. Devices based on bulk lithium niobate whispering gallery mode resonators have shown particularly promising performance, including roughly 10% total transduction efficiency with sub-quanta noise levels [87] and entanglement between microwave and optical fields [88]. This performance is enabled by the exceptionally high optical quality factor ($Q \sim 10^8$) available in whispering gallery mode resonators [89] and the large thermal conductance provided by a millimeter-scale 3D microwave resonator [85]. However, these devices suffer from relatively weak EO interaction strength due to the difficulty of placing electrodes near optical modes in whispering gallery resonators.

The desire to enhance the interaction strength and scalability of EO transducers has motivated the development of cavity EO devices in thin-film EO photonics platforms [66,86,90–93]. To date, EO transducers in thin-film devices have demonstrated bidirectional operation and on-chip efficiency as high as 2% for a relatively large ~ 10 mW optical pump [66], yet power-normalized efficiencies remain low and would require large (~ 1 W) optical pump powers to reach near-unity efficiency.

1.3 Thin-film lithium niobate

To improve efficiency, reduce noise, and lower optical pump power requirements of cavity EO transducers, here we use a thin-film lithium niobate device platform.

Lithium niobate (LN) is an excellent Pockels EO material ($r_{33} = 32$ pm/V) that has been studied for nonlinear and electro-optics applications since the 1960s. Traditional integrated LN devices such as waveguides and modulators are usually formed in bulk LN wafers by proton exchange or titanium diffusion, which creates a weak index contrast ($\Delta n \sim 0.02$) and hence large optical modes, as shown in Figure 1.2a. The low index contrast, large mode size, and wide bending radius requirements make dense integration difficult in traditional LN devices. Furthermore, the size of the optical mode limits the spacing between gate electrodes which

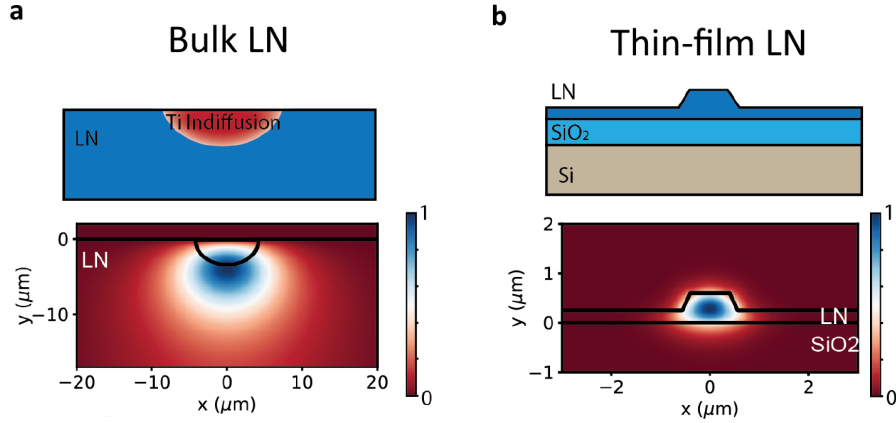


Figure 1.2: Comparison between (a) a traditional waveguide in bulk LN and (b) a ridge waveguide in thin film lithium niobate. Lower color plots show the electric field distribution. Note the factor of 10 difference in plot length scales. Figure adapted from Ref. [94]

reduces the EO coupling. Nonetheless, because of their stability and wide bandwidth, traditional LN devices are widely used for EO modulators in telecommunications applications [95].

Recently, thin-film lithium-niobate-on-insulator (TFLN) wafers have become commercially available². These wafers are typically made using the crystal ion slicing process, originally developed for the fabrication of silicon-on-insulator (SOI) wafers [96] and later adapted to LN starting in the late 1990s [97]. The large index contrast provided by this platform ($\Delta n \sim 0.7$ for silicon dioxide cladding) enables smaller waveguides for higher integration density and stronger EO coupling [94]. To create waveguides in TFLN, some form of lateral index contrast is required. This has been accomplished using proton exchange [98], dielectric loading [99], and directly etching the LN film using laser ablation and chemical-mechanical polishing [100], CF_4 -based reactive ion etching [101], and physical argon plasma etching [102, 103]. In this work, we use argon plasma etching to produce ridge waveguides like that shown in Figure 1.2b. Reactive ion etching of LN with fluorine-based chemistry leaves behind nonvolatile LiF compounds that lead to high etch roughness [104]. Instead, purely physical argon plasma etching has been shown to produce the smooth sidewalls required for low loss optical waveguides, with optical quality factors as high as $Q \sim 10^7$ recently demonstrated [105].

This combination of thin-film wafers and new fabrication techniques has enabled a wide va-

²Devices described in this dissertation are made on wafers purchased from NanoLN.

riety of novel and high-performance device demonstrations in recent years. These include low- $V\pi$ high-speed EO modulators [103], wide bandwidth EO frequency comb generation [106], low-power second harmonic generation [107], and efficient acousto-optic devices [108].

In short, TFLN provides a large EO coefficient of 32 pm/V, tight confinement of the optical mode to enable a strong EO coupling and good integration density for high-complexity design [103], and the ability to realize low-loss optical resonators with demonstrated quality factors (Q) of 10^7 . These properties make lithium niobate a compelling platform for improving transduction efficiency with EO transducers.

1.4 Dissertation outline

This current Chapter 1 "Introduction" describes the motivation for and history of cavity EO devices, particularly in thin-film lithium niobate.

In Chapter 2 "Theory of cavity electro-optics", a quantitative description of cavity EO devices is developed, particularly for triple-resonance devices. These results will be used throughout the rest of the dissertation. This chapter is tutorial in nature for new students and others new to the field of cavity electro-optics.

Chapter 3 "Microwave-to-optical transduction using cavity electro-optics in thin-film lithium niobate" describes the design, characterization, and transduction performance of a first-generation transducer. This transducer displays relatively modest transduction efficiency, but we identify several important device design considerations, including the role of piezoelectric coupling in microwave resonator loss and the impact of free carrier effects in lithium niobate. We also identify several paths to improve device performance.

Chapter 4 "Charge carrier effects in thin-film lithium niobate" describes a series of experiments investigating the role that free charge carriers play in the low-frequency behavior of TFLN optical devices. Free carriers can create several effects in TFLN, including dielectric relaxation which reduces low-frequency EO response, photoconductivity, and photorefractivity which creates changes in the optical index and generates optical index gratings that interfere

with normal device operation. We analyze the origin of free carriers in our devices and demonstrate several fabrication techniques to reduce free-carrier migration.

Chapter 5 "Preliminary characterization of an optimized transducer" builds on Chapter 3 and describes the design of an improved cavity EO transducer. This chapter also describes measurements of transduction noise in both first- and second-generation devices.

Chapter 6 "Outlook: optically heralded generation of remote microwave entanglement" offers an outlook on the use of cavity EO transducers in TFLN for quantum networking applications. It describes a heralded scheme by which even relatively low efficiency but high bandwidth transducers could be used to generate remote entanglement between quantum nodes.

Finally, several appendices provide supplemental technical details and discussion for the main part of the dissertation.

Chapter 2

Theory of cavity electro-optics

Cavity electro-optic devices are one example of a wider class of parametrically coupled resonator systems. Such similar systems span a large range of sizes, frequencies, and physical phenomena, and include mechanical systems [109], cavity opto- or electro-mechanical devices [110], optical and microwave parametric oscillators [81], and magnonic devices [111], among others. These disparate systems can be understood using remarkably similar models because they are all composed of a few harmonic modes that interact through simple parametric couplings¹.

The quantum theory of such systems has been well studied both in general [112, 113], and for electro-optic systems in particular [62, 76, 77, 114]. In this chapter, we apply these models to our system of coupled optical and microwave resonators to develop the theoretical foundations for the experiments described in this work. We begin by introducing the basic Hamiltonian description of the electro-optic interaction in Section 2.1. Section 2.2 includes the effects of loss and coupling to input and output fields. Note that many of these topics are covered in detail in the literature [76, 77, 110]. This chapter is designed to provide a tutorial introduction to the topic, aimed at those who are new to the field. As such we use footnotes to provide further information and consider some important problems using multiple levels of abstraction

¹Parametric coupling, in this context, refers to a situation in which the state of one harmonic mode controls a parameter of another mode. For example, in our devices, the voltage (state) in the microwave resonator can change the frequency (parameter) of an optical mode.

to provide a better understanding.

2.1 Hamiltonian description of cavity electro-optics

The variety of parametrically coupled systems mentioned above can be accurately modeled² using a simple Hamiltonian containing a small number of boson modes and parameters. In this section, we will apply such a Hamiltonian model to our cavity electro-optic devices.

2.1.1 Phenomenological approach

To help develop physical intuition, in this section we will first consider the concrete case of our device. This device is illustrated in Fig. 1.1b and is composed of two evanescently coupled optical ring resonators and a microwave LC resonator whose capacitor also serves as a gate on the optical rings. Later in Section 2.1.2, we will consider the more general case of cavity electro-optics with arbitrary electromagnetic modes from first principles.

Assuming that the free spectral range (FSR) of the ring resonators is large compared to the microwave frequency, we can restrict our analysis to two optical modes in ring 1 and ring 2 that are closely spaced in frequency. The linear, non-interacting Hamiltonian including the microwave mode can be written as

$$H_0 = \omega_1 \hat{a}_1^\dagger \hat{a}_1 + \omega_2 \hat{a}_2^\dagger \hat{a}_2 + \omega_m \hat{b}^\dagger \hat{b} + \mu \left(\hat{a}_1^\dagger \hat{a}_2 + \hat{a}_1 \hat{a}_2^\dagger \right), \quad (2.1)$$

where we set $\hbar = 1$ for simplicity. Here, \hat{a}_i is an annihilation operator for the optical modes in resonator $i=\{1, 2\}$ that has frequency ω_i , \hat{b} is the annihilation operator for the microwave mode with frequency ω_m , and μ is the evanescent coupling rate between the two optical modes³.

The nonlinear interaction is due to the Pockels electro-optic effect. In our devices, the electric fields of the optical and microwave modes are mostly aligned along the Z-axis of the lithium niobate crystal. This configuration means that a non-zero gate voltage will linearly

²At least, within a lossless, closed system approximation.

³Note that for degenerate resonator modes with $\omega_1=\omega_2$, the splitting between the hybridized optical modes will be 2μ under this Hamiltonian.

change the effective index of the optical modes and hence also shift the resonance frequency [115]. We can write the resonance frequency as $\omega_i(V)=\omega_i(0) + G_i V$, where G_i is the electro-optic susceptibility and V is the applied gate voltage. This effect gives the interaction Hamiltonian:

$$H_I = \left(G_1 \hat{a}_1^\dagger \hat{a}_1 + G_2 \hat{a}_2^\dagger \hat{a}_2 \right) \hat{V}. \quad (2.2)$$

Rewriting this interaction Hamiltonian in terms of the zero-point fluctuation voltage V_{ZPF} and the microwave resonator's field operators so that $V = V_{\text{ZPF}}(b + b^\dagger)$, we find

$$H_I = \left(g_1 \hat{a}_1^\dagger \hat{a}_1 + g_2 \hat{a}_2^\dagger \hat{a}_2 \right) (\hat{b} + \hat{b}^\dagger), \quad (2.3)$$

where $g_i = G_i V_{\text{ZPF}}$ is the vacuum electro-optic coupling rate between the microwave mode and each optical mode. The total Hamiltonian $H = H_0 + H_I$ defines the complete closed-system dynamics.

2.1.1.1 The electro-optic coupling rate

Before investigating these dynamics, we can gain a sense the timescales by estimating the electro-optic coupling rate from device parameters. Consider a single ring resonator with circumference l , effective mode index n_{eff} and resonance frequencies

$$f_k = \frac{kc}{ln_{\text{eff}}}, \quad (2.4)$$

where k is a mode index, and c is the free-space speed of light. When we apply a voltage to a gate on this ring, a particular optical resonance frequency $f_o=f_k$ will shift linearly at a rate given by

$$\frac{df_o}{dV} = \frac{G}{2\pi} \approx -\alpha \frac{f_o}{n_g} \frac{\partial n_{\text{eff}}}{\partial V}, \quad (2.5)$$

where α is the effective fraction of the ring covered by the electrodes, and n_g is the group velocity of the optical mode⁴.

We can make a several assumptions to help us estimate the electro-optic response $\frac{\partial n_{\text{eff}}}{\partial V}$. First, we can approximate the electric field created by the gate voltage V as uniform within the waveguide and aligned with the Z axis of the LN crystal. Second, we can neglect all the electro-optic tensor components except the dominant r_{33} term. Finally, we can define an effective capacitor gap d_{eff} which sets the magnitude of the gate electric field $E = V/d_{\text{eff}}$. Using these assumptions, we find

$$\frac{\partial n_{\text{eff}}}{\partial V} = \frac{\partial n_{\text{eff}}}{\partial n_e} \frac{\partial n_e}{\partial E} \frac{dE}{dV} = -\Gamma n_g \frac{r_{33} n_e^2}{2} \frac{1}{d_{\text{eff}}}, \quad (2.6)$$

where n_e is the extraordinary index of LN, $\Gamma = \frac{\partial n_{\text{eff}}}{\partial n_e} \frac{n_e}{n_g}$ is an optical confinement factor, and $\frac{\partial n_e}{\partial E} = -\frac{1}{2} r_{33} n_e^3$. The electro-optic susceptibility is thus

$$\frac{G}{2\pi} = \frac{n_e^2 r_{33} f_o \alpha \Gamma}{2d_{\text{eff}}}. \quad (2.7)$$

In a lumped-element model, the zero-point voltage fluctuation in the LC resonator depends only on the microwave resonance frequency and the total capacitance⁵:

$$V_{\text{ZPF}} = \sqrt{\frac{\hbar \omega_m}{2C}}. \quad (2.8)$$

Combining these results we find that for a particular ring i ,

$$g_i = \frac{n_e^2 r_{33} \omega_o \alpha_i \Gamma}{2d_{\text{eff}}} \sqrt{\frac{\hbar \omega_m}{2C}}. \quad (2.9)$$

In our devices, typical values of the key parameters for determining g_0 are $\Gamma \approx 1$, $\alpha = 0.5$, $d_{\text{eff}} = 10 \mu\text{m}$, $\omega_m/2\pi = 5 \text{ GHz}$, and $C = 100 \text{ fF}$, leading to $g_0/2\pi \approx 1 \text{ kHz}$. Comparing this value to

⁴The group velocity appears here because n_{eff} depends on both the applied voltage and the optical frequency. The fact that the optical frequency of the mode changes when you apply a voltage means you cannot simply assume $\frac{df_o}{dV} = \frac{df_o}{dn_{\text{eff}}} \frac{dn_{\text{eff}}}{dV}$.

⁵Note that the zero point electrical energy is $\frac{1}{2} \hbar \omega_m$. The total capacitance of an LC resonator can be considered as the lumped-element analog of mode volume.

typical optical and microwave mode loss rates of 100 MHz and 10 MHz, respectively, we see that the interaction rate is significantly smaller, which would make it difficult to directly observe the coupling. As described in Chapter 1, we can overcome this large difference using optical pumping and a double ring structure. The linearization and enhancement of the interaction strength by optical pumping are described in Section 2.1.3.

More accurate calculations of g_i – useful for device design and analysis – can be obtained without resorting to the assumptions made in the derivation of G above by using the full theory of waveguide-based Pockels modulators. This theory is covered in detail in previous work [116, 117], but we briefly review the key results here.

The effective index shift of the mode when applying a voltage to the gate electrodes can be calculated using perturbation theory as

$$\Delta n_{\text{eff}} = \frac{1}{c} \int_{\text{LN}} dA \vec{E}_o^* \Delta \bar{\epsilon} \vec{E}_o, \quad (2.10)$$

where E_o is the cross-sectional electric field of the optical mode, normalized so that

$$\int dA (E_o \times H_o^* + E_o^* \times H_o) \cdot \hat{z} = 1, \quad (2.11)$$

and $\Delta \bar{\epsilon}$ is the permittivity perturbation created by the applied voltage. This perturbation can be calculated from the electric field profile E generated by the applied voltage V :

$$\Delta \bar{\epsilon}_{ij} = \sum_k \epsilon_{ii} \epsilon_{jj} r_{ijk} E_k / \epsilon_0, \quad (2.12)$$

where ϵ_0 is the permittivity of free space. We can calculate the electro-optic susceptibility G using Equations 2.10 and 2.5 and finite element modeling to calculate the optical and microwave fields E and E_o . we can compare the resulting value of G to Equation 2.7 and define an equivalent d_{eff} parameter, which is used throughout the rest of this work.

2.1.1.2 Hybrid optical modes

The interaction Hamiltonian in Eq. 2.3 is given in terms of the ring optical modes $\hat{a}_{1,2}$. However, due to the evanescent coupling, the true optical eigenmodes of our system are hybrid modes that are delocalized between the two ring resonators. We will now transform the Hamiltonian into the basis of these hybrid optical modes.

For convenience, we write the Hamiltonian as

$$\begin{aligned} H_0 &= \omega_m \hat{b}^\dagger \hat{b} + (\omega_o + \delta) \hat{a}_1^\dagger \hat{a}_1 + (\omega_o - \delta) \hat{a}_2^\dagger \hat{a}_2 + \mu \left(\hat{a}_1^\dagger \hat{a}_2 + \hat{a}_1 \hat{a}_2^\dagger \right), \\ H_I &= \left(g_1 \hat{a}_1^\dagger \hat{a}_1 + g_2 \hat{a}_2^\dagger \hat{a}_2 \right) (\hat{b} + \hat{b}^\dagger), \end{aligned} \quad (2.13)$$

where $\omega_{1,2} = \omega_o \pm \delta$, i.e. 2δ is the detuning between the ring modes and ω_o is the center frequency between the ring modes. The optical part of this Hamiltonian can be diagonalized into two hybrid modes \hat{a}_+ and \hat{a}_- . Since these new eigenmodes are orthogonal, we can write a generic Bogoliubov transformation

$$\begin{aligned} \hat{a}_+ &= u \hat{a}_1 - v \hat{a}_2, \\ \hat{a}_- &= v \hat{a}_1 + u \hat{a}_2. \end{aligned} \quad (2.14)$$

Note that \hat{a}_+ and \hat{a}_- must obey a bosonic commutation relation $[\hat{a}_i, \hat{a}_j] = \delta_{ij}$, which requires that $u^2 + v^2 = 1$. To enforce this condition, we set $u = \cos \frac{\theta}{2}$, $v = \sin \frac{\theta}{2}$, where θ is a hybridization parameter to be determined by the detuning and coupling strength. The linear optical part of the Hamiltonian will be diagonalized for $\tan \theta = \frac{\mu}{\delta}$. This transformation yields the Hamiltonian

$$\begin{aligned} H_0 &= \omega_+ \hat{a}_+^\dagger \hat{a}_+ + \omega_- \hat{a}_-^\dagger \hat{a}_- + \omega_b \hat{b}^\dagger \hat{b} \\ H_I &= \left(\hat{b}^\dagger + \hat{b} \right) \left[(v^2 g_1 + u^2 g_2) \hat{a}_-^\dagger \hat{a}_- + (u^2 g_1 + v^2 g_2) \hat{a}_+^\dagger \hat{a}_+ + uv (g_1 - g_2) \left(\hat{a}_-^\dagger \hat{a}_+ + \hat{a}_- \hat{a}_+^\dagger \right) \right]. \end{aligned} \quad (2.15)$$

where $\omega_\pm = \omega_o \pm \sqrt{\delta^2 + \mu^2}$ are the frequencies of the hybrid modes. The first two terms in the brackets proportional to $\hat{a}_-^\dagger \hat{a}_-$ and $\hat{a}_+^\dagger \hat{a}_+$ represent frequency modulation of the opti-

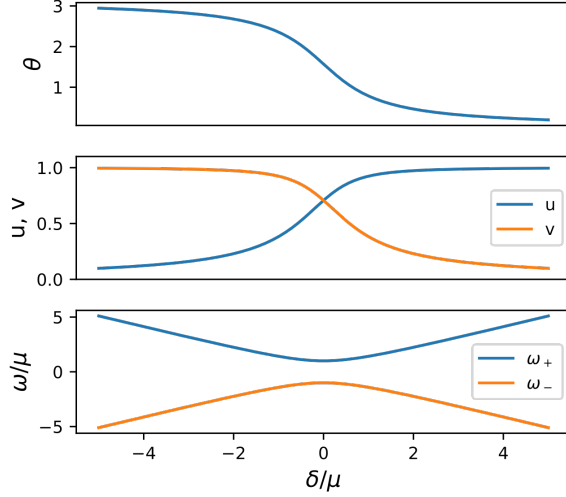


Figure 2.1: The normalized dependence of the hybridization parameters on the optical mode detuning δ , showing θ (top), u and v (middle) and ω_{\pm} (bottom).

cal modes, and can be neglected in the resolved-sideband regime where the optical mode linewidth is much smaller than the microwave frequency. The second term in the brackets represents the desired triple-resonance sum and difference frequency generation processes, with single-photon interaction rate

$$g_0 = uv(g_1 - g_2) = \frac{n_e^2 r_{33} \omega_o \alpha \Gamma \sin \theta}{4d_{\text{eff}}} \sqrt{\frac{\hbar \omega_m}{2C}}, \quad (2.16)$$

where we assumed g_1 and g_2 have opposite sign, and $\alpha = \alpha_1 + \alpha_2$ is a total device electrode coverage factor with maximum value of 2. The hybridization parameters and optical frequencies of the hybrid modes are shown in Figure 2.1, illustrating the anticrossing between the two ring modes.

We can gain a better understanding of this Hamiltonian by considering the degenerate ring mode case where $\delta=0$. In this case $u=v=\frac{1}{\sqrt{2}}$, the hybrid optical modes \hat{a}_+ and \hat{a}_- are symmetric and antisymmetric equal superpositions of the ring modes (see Eq. 2.14), and the interaction Hamiltonian is

$$H_I = (\hat{b}^\dagger + \hat{b}) \left[\frac{1}{2} (g_1 + g_2) (\hat{a}_+^\dagger \hat{a}_+ + \hat{a}_-^\dagger \hat{a}_-) + \frac{1}{2} (g_1 - g_2) (\hat{a}_+^\dagger \hat{a}_- + \hat{a}_+ \hat{a}_-^\dagger) \right]. \quad (2.17)$$

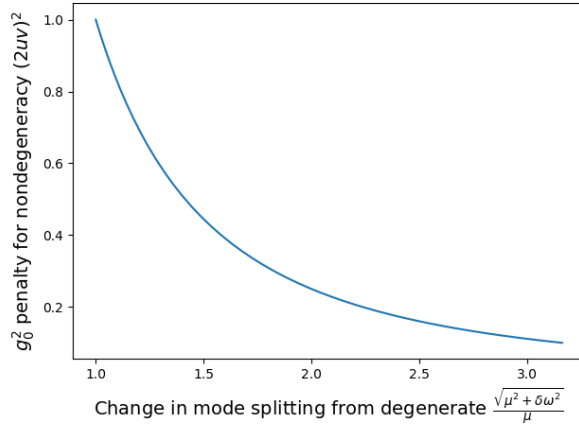


Figure 2.2: The penalty for using non-degenerate modes as a function of the fractional change in the mode splitting compared to the degenerate case.

We see immediately that the interaction rate will be maximized for antisymmetric driving, i.e. $g_2 = -g_1$. This makes intuitive sense: in a microwave-to-optical transduction process, for example, we might want to drive a transition from the symmetric to antisymmetric optical modes, which requires an antisymmetric drive to overcome the difference in parity.

Comparing degenerate ($\delta=0$) and nondegenerate ($\delta \neq 0$) cases we see that the exchange interaction strength is penalized for nondegeneracy by a factor of $2uv = \sin \theta$. Figure 2.2 shows the quantitative effect of this nondegeneracy on the experimentally relevant⁶ parameter g_0^2 .

2.1.2 First principles approach

Above, we derived the interaction Hamiltonian starting from the phenomenological fact that the ring resonators in our device have a resonance frequency that depends linearly on their gate voltage due to electro-optic changes in refractive index. This approach is physically concrete and works well for our particular devices that use Z-oriented electric fields in lithium niobate. However, that phenomenological approach is not always easy to apply to all cavity electro-optic devices. For example, devices that rely on microwave-induced transduction between different polarization modes, such as those in Ref. [66], cannot be understood by modulation of a scalar optical index.

⁶Relevant to the cooperativity $C = \frac{4g_0^2 n_{\text{pump}}}{\kappa_o \kappa_m}$, which sets transduction efficiency, for example.

It is useful, then, to consider a more general first-principles approach in which we directly investigate the coupling between different electromagnetic modes caused by the nonlinear susceptibility of the material [118]. This will also allow us to see the connection between the formalisms used in electro-optical devices and that used in nonlinear optics. To do so, we will first determine the nonlinear energy density inside a $\chi^{(2)}$ material under the application of electromagnetic fields. Then, we will carefully define and quantize the fields in our device. Finally, we will integrate the energy density produced by these fields to derive the nonlinear interaction Hamiltonian.

In a $\chi^{(2)}$ material, an applied electric field \vec{E} induces a nonlinear dielectric polarization \vec{P} . For simplicity, we will consider a scalar model where the electric field points along the Z-axis of LN and only the $\chi_{333}^{(2)}$ nonlinear coefficient is significant. In this case, the dielectric polarization can be written $P = \epsilon_0 \chi^{(2)} E^2$. In a scalar dipolar approximation, we can write the nonlinear energy density as ⁷

$$dU = dE \cdot P. \quad (2.18)$$

The electromagnetic modes can be quantized in the usual way [119]:

$$E_k(r, t) = \sqrt{\frac{\hbar\omega_k}{2\epsilon_{NL,k}V_k}} \left(\psi_k(r) \hat{a}_k e^{-i\omega_k t} - \psi_k^*(r) \hat{a}_k^\dagger e^{i\omega_k t} \right), \quad (2.19)$$

where again we assume the electric field points along the Z-axis of LN, $V_k = \int dV \frac{\epsilon_k(\vec{r})}{\epsilon_{NL,k}} |\psi_k(r)|^2$ is the mode volume, ψ_k is a unitless mode profile⁸, and $\epsilon_{NL,k}$ is the dielectric permittivity inside the nonlinear material.

We will now apply this approach to our devices with three modes (two optical- and one microwave-frequency) that can be described by the electric field distributions $\{E_+, E_-, E_m\}$ respectively. It is convenient to use a more specific parameterization of the microwave resonator mode to connect this mode directly to device parameters that are easy to calculate. To

⁷It is tempting to think that the energy density should be simply $U = \vec{E} \cdot \vec{P}$. That would be true for permanent dipoles, but here the polarization is induced. Because this induced polarization is nonlinear as well, not even the usual linear dielectric result of $U = \frac{1}{2} \vec{E} \cdot \vec{P}$ can be applied. Instead, we resort to the infinitesimal form and do the integration to find that $U = \frac{1}{3} \vec{E} \cdot \vec{P}$.

⁸Note that ψ can be scaled arbitrarily because it is normalized by V .

do so, we fix $|\psi_m| = 1$ in the optical mode and assume the microwave resonator can be described by a lumped-element model. By equating the electrical energy density in the lumped-element model and dimensional model (Eq. 2.19), we find $V_m = \frac{Cd_{\text{eff}}^2}{\epsilon_{NL,m}}$. To quantitatively describe the mode profiles ψ_k , we define a synthetic dimension x that corresponds to the circumferential distance along the ring resonators of a point located near the optical waveguide, where $x > 0$ for locations inside ring 1 and $x < 0$ for locations inside ring 2. We also define a two-dimensional displacement vector \vec{s} that corresponds to the location of the point in cross section. Finally, we define a boxcar function $\Pi(x)$ such that $\Pi(x \in [0, l]) = 1$ and $\Pi(x \notin [0, l]) = 0$. Using these tools, we can write the mode profiles as

$$\psi_m = \Pi(x) - \Pi(-x) \quad (2.20)$$

$$\psi_+ = \Phi(\vec{s})e^{ikx} (v\Pi(-x) - u\Pi(x)) \quad (2.21)$$

$$\psi_- = \Phi(\vec{s})e^{ikx} (u\Pi(-x) + v\Pi(x)), \quad (2.22)$$

where $\Phi(\vec{s})$ is the cross sectional optical mode profile.

In our device, all modes have electric fields inside the lithium niobate which point primarily along the Z crystal axis within the region of the waveguide, so the scalar approximations made above are reasonably accurate. Integrating the nonlinear energy density in Equation 2.18 with a total electric field $E = \sum_k E_k$, we find

$$\begin{aligned} U = \epsilon_0 \chi^{(2)} & \left(\frac{1}{3} E_m^3 + \frac{1}{3} E_-^3 + \frac{1}{3} E_+^3 \right. \\ & + E_m E_-^2 + E_m E_+^2 + E_- E_m^2 + E_- E_+^2 + E_+ E_m^2 + E_+ E_-^2 \\ & \left. + 2E_m E_- E_+ \right). \end{aligned} \quad (2.23)$$

The last term in this Hamiltonian creates the desired mixing between microwave and optical modes. Neglecting the other terms for being non-resonant, inserting the modes described by

Equation 2.19, and keeping resonant terms, the energy density is

$$U = \frac{\hbar\epsilon_0\chi^{(2)}\omega_{\text{opt}}}{\epsilon_{LN,\text{opt}}V_{\text{opt}}d_{\text{eff}}}\sqrt{\frac{\hbar\omega_m}{2C}}\left(\psi_m\psi_-\psi_+^*\hat{b}\hat{a}_-\hat{a}_+^\dagger + \text{h.c.}\right), \quad (2.24)$$

where $\omega_{\text{opt}} \approx \omega_{\pm}$, $V_{\text{opt}} \approx V_{\pm}$, and $\epsilon_{LN,\text{opt}} \approx \epsilon_{LN,\pm}$ are parameters for the optical modes.

The interaction Hamiltonian can be found by integrating this energy density. Assuming that the field created by the microwave resonator is constant across the cross section of the optical mode, we find:

$$H_I = -\frac{\hbar\epsilon_0\chi^{(2)}\omega_{\text{opt}}\Gamma uv\alpha}{\epsilon_{\text{opt}}d_{\text{eff}}}\sqrt{\frac{\hbar\omega_m}{2C}}\left(\hat{b}\hat{a}_-\hat{a}_+^\dagger + \text{h.c.}\right), \quad (2.25)$$

where $\Gamma = \frac{V_{\text{opt,LN}}}{V_{\text{opt}}}$ is the optical confinement factor and $V_{\text{opt,LN}} = \int_{LN} dV \frac{\epsilon_{\pm}(\vec{r})}{\epsilon_{NL,\pm}} |\psi_{\pm}(r)|^2$ is the mode volume integral taken only over the nonlinear material. Noting that $\chi^{(2)} = \frac{r_{33}n^4}{2}$, this result is identical to that found by the phenomenological approach taken above.

2.1.3 Linearization of the interaction Hamiltonian

For all currently studied electro-optic devices, the single-photon interaction rate g_0 , which has a typical magnitude of 1 Hz to 1 kHz, is much slower than the microwave and optical decay rates. This makes the interaction between the microwave and optical fields difficult to detect when working with quantum-level signals. Luckily, however, the microwave-optical interaction rate can be enhanced by applying a strong pump laser. This technique is commonly used in traditional electro-optic modulators. If a modulator was driven with just a few optical and microwave photons, the probability that any of the photons would interact to produce modulation would be vanishingly small. However, by using a strong optical drive, even very weak microwave signals can produce measurable optical modulation.

We now seek to understand how the Hamiltonian described above will behave under optical pumping near the triple resonance condition. Starting with the Hamiltonian Eq. 2.15, we first move the optical modes to a frame rotating at the laser frequency using the transformation $U = e^{i\omega_L(\hat{a}_-\hat{a}_- + \hat{a}_+^\dagger\hat{a}_+)}t$ where ω_L is the laser frequency. This transformation yields the new

Hamiltonian⁹

$$H = -\Delta_- \hat{a}_-^\dagger \hat{a}_- - \Delta_+ \hat{a}_+^\dagger \hat{a}_+ + \omega_m \hat{b}^\dagger \hat{b} + (\hat{b}^\dagger + \hat{b}) \left[g_- \hat{a}_-^\dagger \hat{a}_- + g_+ \hat{a}_+^\dagger \hat{a}_+ + g_0 (\hat{a}_-^\dagger \hat{a}_+ + \hat{a}_- \hat{a}_+^\dagger) \right], \quad (2.26)$$

where $\Delta_\pm = \omega_L - \omega_\pm$ is the detuning of each mode from the laser frequency¹⁰, and $g_{+,-,0}$ are the interaction strengths for the given terms of the Hamiltonian. The first and second terms within the brackets are the standard interaction terms typically seen in systems of two parametrically coupled resonators with frequency modulation, such as optomechanics. These terms can in principle give rise to interactions between each optical mode individually and the microwave mode, seen in Chapter 3 and described in Appendix B.2. However, for now we will neglect these terms, as the third term is the desired interaction, and it will be dominant under triple resonance conditions.

2.1.3.1 Red sideband pumping

Now let's consider what happens when we pump the \hat{a}_- mode, i.e. red side pumping. In this case when $\omega_L \approx \omega_-$, the \hat{a}_- mode will be driven by a strong coherent state and we can neglect small single-photon level dynamics of this mode, replacing the mode operators with a classical field amplitude¹¹ $\hat{a}_- \rightarrow \alpha_- = \sqrt{n_-}$, which we take to have phase $\angle \alpha_- = 0$. Note that α_- depends on the optical pump power and enhancement due to the optical resonance, and can be calculated using the open resonance analysis of section 2.2.1. In this approximation the Hamiltonian becomes

$$H = -\Delta_+ \hat{a}_+^\dagger \hat{a}_+ + \omega_m \hat{b}^\dagger \hat{b} + (\hat{b}^\dagger + \hat{b}) \left[g_- |\alpha_-|^2 + g_+ \hat{a}_+^\dagger \hat{a}_+ + g (\hat{a}_+ + \hat{a}_+^\dagger) \right], \quad (2.27)$$

where $g = \alpha_- g_0$ is the pump-enhanced interaction strength.

As discussed above, we can neglect the first two terms in the bracket, so there are a total

⁹Via the transformation $H = U H_{\text{old}} U^\dagger - i\hbar U \frac{\partial U^\dagger}{\partial t}$.

¹⁰Defined this way so that negative detuning indicates a laser frequency lower than the resonance frequency.

¹¹I.e. complex number.

of four interaction terms $H_I = g \left(\hat{b}^\dagger \hat{a}_+ + \hat{b} \hat{a}_+^\dagger + \hat{b}^\dagger \hat{a}_+^\dagger + \hat{b} \hat{a}_+ \right)$. The first two terms represent a beam-splitter type interaction. The second two terms represent parametric amplification and can result in two-mode squeezing. If we are pumping on the red optical mode \hat{a}_- while near the triple resonance condition $\Delta_+ \approx -\omega_m$, the parametric amplification terms can be neglected under a rotating wave approximation¹² and the Hamiltonian can be approximated as

$$H_{\text{red}} = -\Delta_+ \hat{a}_+^\dagger \hat{a}_+ + \omega_m \hat{b}^\dagger \hat{b} + g \left(\hat{b}^\dagger \hat{a}_+ + \hat{b} \hat{a}_+^\dagger \right). \quad (2.28)$$

This Hamiltonian is the mechanism by which a cavity electro-optic device can be used as a microwave-optical transducer [48, 77]. The beamsplitter interaction means that photons can be transferred between the microwave and optical resonators. For example, in the strong coupling regime where the pumped enhanced interaction strength g is larger than the decay rates of the microwave and optical modes, an excitation in one mode (\hat{a}_+ or \hat{b}) would be transferred into the other mode in a Rabi-flopping process. However, demonstrated cavity electro-optic devices have not yet reached this regime. Nonetheless, by coupling these resonators to waveguides, we can still create a high-efficiency converter between flying microwave and optical qubits, as described in Section 2.2 below.

2.1.3.2 Blue sideband pumping

If we were instead to pump the a_+ mode ($\omega_L \approx \omega_+$), then we could repeat the above steps to find

$$H_{\text{blue}} = -\Delta_- \hat{a}_-^\dagger \hat{a}_- + \omega_m \hat{b}^\dagger \hat{b} + g \left(\hat{b}^\dagger \hat{a}_-^\dagger + \hat{b} \hat{a}_- \right), \quad (2.29)$$

where $\Delta_- = \omega_L - \omega_-$ is the detuning of the ω_- mode from the pump. This Hamiltonian represents parametric amplification, or a two-mode squeezing interaction [77]. In the weak op-

¹²To show this: If you remove the independent-cavity terms of the Hamiltonian proportional to number operators by moving to the rotating frame represented by the transformation $U = e^{-i\Delta_+ a_+^\dagger a_+ t} e^{i\omega_b b^\dagger b t}$, then the interaction terms will have a time dependence. You will find that the beamsplitter terms rotate slowly at a frequency $\omega_m + \Delta_+$ and the parametric terms rotate rapidly at $\omega_m - \Delta_+$. Recall that for red mode pumping $\Delta_+ < 0$.

tical pumping regime it can be used to generate correlated microwave-optical photons pair. In Chapter 6 we describe how this effect can be used to generate heralded remote entanglement between two transducers. With stronger optical pumping this parametric amplification interaction can be used to generate continuous variable entanglement between microwave and optical fields [120].

2.2 Open-system description of cavity electro-optics

To use a cavity electro-optic device as a quantum transducer, we must have a way to both insert and retrieve quantum states. This requires coupling to the outside world that is not covered in the Hamiltonian description of Section 2.1. Indeed, besides the intentional extrinsic coupling to well-defined input and output channels, real devices always have unintended (and often undesired) coupling to the environment in the form of intrinsic loss. As mentioned above, these loss rates are typically larger than the electro-optic interaction rates of the system, so they play a large role in the dynamics of the system and lead to qualitative changes in behavior that would not be expected in the Hamiltonian model. In this section, we begin by reviewing the open system analysis of a single resonant mode based on an input-output formalism [121]. We then apply this theory to the operation of cavity electro-optic transducer and develop the electro-optic scattering matrix. Finally, we extend our results to include noise generated in the microwave resonator (for example, caused by optical absorption). The results in this section will be used to analyze measured device performance throughout this dissertation.

2.2.1 Resonators with loss and waveguide coupling

First, we will review the modeling of a lossy resonator with input-output formalism. Selecting a single mode and neglecting all others, we can use Heisenberg-Langevin input-output formal-

ism to write the equation of motion for the field amplitude of that mode¹³ [121]:

$$\dot{\hat{a}} = i\Delta\hat{a} - \frac{\kappa}{2}\hat{a} + \sqrt{\kappa_e}\hat{a}_{\text{in}} + \sqrt{\kappa_i}\hat{f}_{\text{in}}, \quad (2.30)$$

where $\Delta = \omega_l - \omega_0$ is the laser detuning relative to the mode, \hat{a}_{in} is the input field, \hat{f}_{in} is the environmental noise operator, and κ , κ_e , and κ_i are the total, extrinsic, and intrinsic decay rates, respectively¹⁴. The input fields are normalized so that $P = \hbar\omega_l \langle \hat{a}_{\text{in}}^\dagger \hat{a}_{\text{in}} \rangle$. Note that these input field operators have units, and $\langle \hat{a}_{\text{in}}^\dagger \hat{a}_{\text{in}} \rangle$ is the rate of photons arriving at the cavity. The field that is transmitted through the coupling waveguide is given by the input-output relationship

$$\hat{a}_{\text{out}} = \hat{a}_{\text{in}} - \sqrt{\kappa_e}\hat{a}. \quad (2.31)$$

It is useful to consider a simpler semi-classical picture, in which we ignore the quantum nature of the field operators, and instead treat them as complex amplitudes of the electric field of the modes. This approximate model is accurate when the fields contain many photons. This approximation is equivalent to looking at the expectation value of the field operators. We can find the steady-state ($\dot{\hat{a}} \rightarrow 0$) field inside the cavity under CW laser excitation using Equation 2.30:

$$\langle \hat{a} \rangle = \frac{\sqrt{\kappa_e} \langle \hat{a}_{\text{in}} \rangle}{\kappa/2 - i\Delta}. \quad (2.32)$$

The steady state number of photons circulating in the resonator is given by

$$n_{\text{cav}} = |\langle \hat{a} \rangle|^2 = \frac{\kappa_e}{\Delta^2 + (\kappa/2)^2} \frac{P}{\hbar\omega_l}. \quad (2.33)$$

This useful result allows us to calculate the pump-enhanced interaction strength described earlier, $g = \sqrt{n_{\text{opt}}}g_0$.

¹³This equation of motion is given in a rotating frame produced by the unitary transformation $U = e^{i\omega_L \hat{a}^\dagger \hat{a} t}$, which is equivalent to applying the transformation $\hat{a}_{\text{old}} = e^{-i\omega_L t} \hat{a}$ to all field operators.

¹⁴Throughout this work we use the energy decay rate, so that for example, $Q = \omega/\kappa$.

The transmission amplitude is now easily found using Equations 2.31 and 2.32 to be

$$t = \frac{\langle \hat{a}_{\text{out}} \rangle}{\langle \hat{a}_{\text{in}} \rangle} = \frac{(\kappa_i - \kappa_e) / 2 - i\Delta}{(\kappa_i + \kappa_e) / 2 - i\Delta}. \quad (2.34)$$

The power transmission is

$$T = |t|^2 = \frac{(\kappa_i - \kappa_e)^2 / 4 + \Delta^2}{(\kappa_i + \kappa_e)^2 / 4 + \Delta^2} \quad (2.35)$$

Note that for the resonator with a single input and output channel described here, the power transmission T displays an ambiguity between κ_i and κ_e . These quantities are interchangeable in Eq. 2.35. This leads to the well-known challenge of extracting the loss rates from measured power transmission spectra [122]. A wide range of techniques can be used to overcome this ambiguity, including measuring the phase of transmission and measuring multiple devices with different coupling geometry to change κ_e independent of κ_i .

2.2.2 Lossy hybrid optical modes

The analysis above applies to single optical modes. The hybrid optical modes used in our devices display coupling to extrinsic and intrinsic channels that depends on the degree of hybridization. For example, in the far-detuned regime $\delta \gg \mu$ where hybridization is negligible, we expect one mode will reside primarily in the coupled "bright" ring resonator and be visible, whereas the other mode will be confined to the uncoupled "dark" ring, making it difficult to detect in transmission measurements. In this section, we study the coupling of such hybrid optical modes to their environment.

We seek to study the optical modes \hat{a}_{\pm} , which each have their own frequency ω_{\pm} , extrinsic loss rate $\kappa_{\pm,e}$, and intrinsic loss rate $\kappa_{\pm,i}$. Our task is to determine what these parameters are in terms of the properties of the (non-hybridized) ring resonator modes. From here on, we take mode \hat{a}_1 to be the bright ring mode that couples to the waveguide, and \hat{a}_2 to be a dark ring mode that has only intrinsic loss. Intuitively, we would expect the loss rates of each hybrid mode to be an average of the loss rates of the ring resonator modes, weighted by the fraction of the hybrid mode energy contained in the each ring resonator. Since the fraction of

energy in each ring is given by u^2 and v^2 (see Eq. 2.14) we expect

$$\begin{aligned}\kappa_{+,j} &= u^2\kappa_{1,j} + v^2\kappa_{2,j} \\ \kappa_{-,j} &= v^2\kappa_{1,j} + u^2\kappa_{2,j},\end{aligned}\tag{2.36}$$

where $j = e, i$ is an index denoting intrinsic or extrinsic rates, and $\kappa_{1,e} = \kappa_e$ for the bright mode while $\kappa_{2,e} = 0$ for the dark mode.

Combined with the hybrid mode frequencies in Eq. 2.15, we now have all the parameters for hybrid modes needed to write down their equations of motion:

$$\dot{\hat{a}}_{\pm} = i\Delta_{\pm}\hat{a}_{\pm} - \kappa_{\pm}\hat{a}_{\pm} + \sqrt{\kappa_{\pm,e}}\hat{a}_{\text{in}} + \sqrt{\kappa_{\pm,i}}\hat{f}_{\pm}.\tag{2.37}$$

The above intuitively-derived equations of motion are accurate in our case, but it is interesting to consider the rigorous approach to solve this problem. Such an approach would involve directly diagonalizing the the full equations of motion for $\hat{a}_{1,2}$. We can estimate the scale of the differences between this rigorous approach and the approach taken in Eq. 2.37 without performing the full calculation by applying the closed-system transformation Eq. 2.14 to the equations of motion for $\hat{a}_{1,2}$. Doing so, we find

$$\dot{\vec{a}} = \begin{bmatrix} i\Delta_- - \kappa_- & \mathcal{O}(\kappa) \\ \mathcal{O}(\kappa) & i\Delta_+ - \kappa_+ \end{bmatrix} \vec{a} + \text{force terms}.\tag{2.38}$$

The off-diagonal terms in the matrix represent dissipative coupling between the closed-system hybrid modes. These exist because the hybrid modes we have chosen are based on our diagonalization of the closed system (Equation 2.14). In reality, the true eigenmodes of the system are the result of diagonalizing the open system equations of motion. However, our system is in the resolved-sideband limit (meaning $|\Delta_+ - \Delta_-| \gg \kappa$), so the off-diagonal terms in the above matrix will have a negligible second-order effect on the dynamics of the system. This being the case, for simplicity we neglect the dissipative coupling and use the closed-system diagonalization for the open system as well.

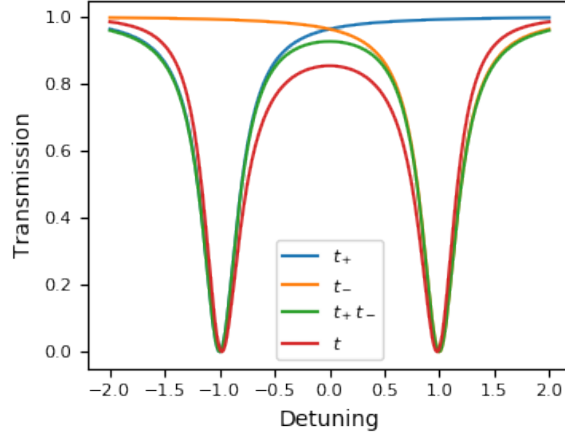


Figure 2.3: Power transmission for two hybrid modes with frequency splitting of 2 and internal and external coupling rates of 0.2 in normalized frequency units.

The input-output relationship of Eq. 2.31 generalizes for multiple modes as

$$a_{\text{out}} = a_{\text{in}} - \sum_j \sqrt{\kappa_{e,j}} a_j. \quad (2.39)$$

We apply this result and the equations of motion in Eq. 2.37 to derive the transmission

$$t = t_+ t_- - \frac{\kappa_{e+} \kappa_{e-}}{(\kappa_+ - i\Delta_+) (\kappa_- - i\Delta_-)}, \quad (2.40)$$

where t_{\pm} is the single-mode transmission (Eq. 2.34 applied to the a_{\pm} mode). The last term represents interference between fields transmitted through the two modes, which have different phases due their different detunings Δ_{\pm} . In the resolved-sideband limit, this extra term typically only has a small effect on the transmission (see Figure 2.3).

2.2.3 The electro-optic scattering matrix

We now consider the dynamics of the electro-optically coupled system. For concreteness, we begin by analyzing an experiment in which a strong pump laser is tuned near resonance with the \hat{a}_- (red) optical mode, while we also excite the system with a weak microwave input and a weak optical probe sideband at frequency ω_{probe} that can be swept over the \hat{a}_+ (blue) optical mode. As seen in Eq. 2.28, the pump laser creates a strong interaction between the \hat{a}_+ and

\hat{b} modes. This interaction causes several effects, including changes in the transmission of the probe fields and transduction between the probe fields.

Under the action of the beamsplitter Hamiltonian (Equation 2.28), the Heisenberg-Langevin equations of motion for the fields in the \hat{a}_+ and \hat{b} modes are:

$$\frac{d\hat{a}_+}{dt} = - \left(-i\Delta_+ + \frac{\kappa_+}{2} \right) a_+ - ig\hat{b} + \sqrt{\kappa_{+,e}}\hat{a}_{\text{in}}e^{-i\omega_p t}, \quad (2.41)$$

$$\frac{d\hat{b}}{dt} = - \left(i\omega_m + \frac{\kappa_m}{2} \right) \hat{b} - ig\hat{a}_+ + \sqrt{\kappa_{m,e}}\hat{b}_{\text{in}}e^{-i\omega_{\text{bin}} t}, \quad (2.42)$$

where $\omega_p = \omega_{\text{probe}} - \omega_L$ is the detuning of the optical probe from the pump, ω_{bin} is the frequency of the microwave excitation, and we have neglected thermal and vacuum fluctuations that will not contribute the average amplitude. These coupled linear equations can be solved for the field amplitude inside the resonators in the frequency domain¹⁵. Combining these results with the input-output relations,

$$\hat{a}_{\text{out}} = \hat{a}_{\text{in}} - \sqrt{\kappa_{+,e}}\hat{a}_+, \quad \hat{b}_{\text{out}} = \hat{b}_{\text{in}} - \sqrt{\kappa_{b,e}}\hat{b}, \quad (2.43)$$

we find the scattering matrix for this process

$$\begin{bmatrix} \hat{a}_{\text{out}} \\ \hat{b}_{\text{out}} \end{bmatrix} = \begin{bmatrix} 1 - \frac{\kappa_{+,e}}{-i(\Delta_+ + \omega_p) + \frac{\kappa_+}{2} + \frac{g^2}{i(\omega_m - \omega_p) + \kappa_m/2}} & \frac{ig\sqrt{\kappa_{+,e}\kappa_{b,e}}}{[i(\omega_m - \omega_{\text{bin}}) + \frac{\kappa_m}{2}][-i(\Delta_+ + \omega_{\text{bin}}) + \frac{\kappa_+}{2}] + g^2} \\ \frac{ig\sqrt{\kappa_{+,e}\kappa_{b,e}}}{[i(\omega_m - \omega_p) + \frac{\kappa_m}{2}][-i(\Delta_+ + \omega_p) + \frac{\kappa_+}{2}] + g^2} & 1 - \frac{\kappa_{b,e}}{i(\omega_m - \omega_{\text{bin}}) + \frac{\kappa_m}{2} + -i(\Delta_+ + \omega_{\text{bin}}) + \kappa_+/2} \end{bmatrix} \begin{bmatrix} \hat{a}_{\text{in}} \\ \hat{b}_{\text{in}} \end{bmatrix} \quad (2.44)$$

$$= \begin{bmatrix} S_{\text{oo}} & S_{\text{oe}} \\ S_{\text{eo}} & S_{\text{eo}} \end{bmatrix} \begin{bmatrix} \hat{a}_{\text{in}} \\ \hat{b}_{\text{in}} \end{bmatrix}. \quad (2.45)$$

This scattering matrix is a complete description of the transduction and reflection of CW

¹⁵To show this, consider one excitation at a time, either optical or microwave. The linearity of the problem ensures the principle of superposition applies. Then transform both field operators into a frame rotating at the excitation frequency and take the time derivatives to be zero in the steady state.

microwave and optical-probe fields. Note that this simple description does not include the effect of noise in the transduction process, which is discussed below.

2.2.3.1 Electro-optic transduction

The off-diagonal elements of the electro-optic scattering matrix represent bidirectional frequency conversion. This conversion is symmetric, and the on-chip transduction efficiency can be written as

$$\eta_{\text{transduction}}(\omega) = |S_{\text{eo}}|^2 = |S_{\text{oe}}|^2 = \frac{\kappa_{m,e}\kappa_{+,e}}{\kappa_m\kappa_+} \frac{4C}{\left| C + \left[\frac{-2i(\Delta_+ + \omega)}{\kappa_+} + 1 \right] \left[\frac{2i(\omega_m - \omega)}{\kappa_m} + 1 \right] \right|^2}, \quad (2.46)$$

where ω is the excitation frequency and $C = \frac{4g_0^2 n_{\text{pump}}}{\kappa_+ \kappa_m}$ is the cooperativity. Near the triple-resonance condition, this efficiency takes the form

$$\nu_{\text{transduction}}(\omega) = \underbrace{\frac{\kappa_{b,e}\kappa_{+,e}}{\kappa_m\kappa_+}}_{\text{extraction efficiency}} \times \underbrace{\frac{4C}{(1+C)^2}}_{\text{internal efficiency}}. \quad (2.47)$$

Conventionally, this transduction efficiency is broken into two terms highlighted above: the extraction efficiency, which describes the fraction of the energy in the resonators that couples to the extrinsic waveguides, and the internal efficiency, which represents the transduction efficiency between the two resonator modes. In the CW transduction experiment described here, the transduction efficiency is maximized for $C = 1$. As shown in Figure 2.4 the bandwidth of conversion scales as $(1+C)\kappa_m$ in the weak coupling regime where $g < \kappa_m, \kappa_o$. This bandwidth corresponds to the electro-optically enhanced linewidth of the microwave resonator. In the weak coupling regime, the transduction of microwave fields to optical frequencies adds an extra loss mechanism that increases the loss rate of the microwave resonator.

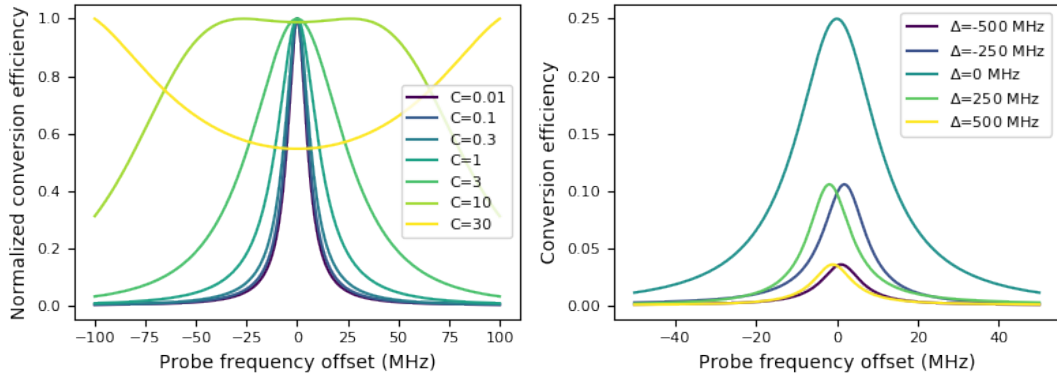


Figure 2.4: Impact of cooperativity and detuning on conversion efficiency. Left: the impact of cooperativity on the conversion efficiency spectrum. Note that the conversion efficiency is normalized to better display the spectrum. Right: the impact of optical mode detuning $\Delta = \Delta_+ + \omega_m$ on the conversion efficiency for $C = 1$. Both plots use the parameters $Q_{i,o}=2 * 10^6$, $Q_{i,m}=700$, $\omega_m/2\pi=4$ GHz, $\Delta_+=4$ GHz, and critical coupling of optical and microwave modes, except where otherwise noted.

2.2.3.2 Electromagnetically induced transparency

The coupling between microwave and optical fields under a strong red-detuned pump causes electromagnetically induced transparency in the transmission of the weak optical probe \hat{a}_{out} through the system. Figure 2.5 shows a plot of the optical probe transmission $|S_{o o}|^2$ for different values of electro-optic cooperativity, optical coupling ratios, and triple-resonance detunings. The EIT resonance feature can take a variety of shapes depending on the regime of the experiment. As one example, in a triple resonance condition with a critically coupled optical mode and low cooperativity $C < 1$ we observe a small transparency window with linewidth $\kappa_{\text{transparency}} = (1 + C)\kappa_m$ and amplitude

$$T_{\text{transparency}} = \frac{1 + C - 2 \frac{\kappa_{+,e}}{\kappa_+}}{1 + C}. \quad (2.48)$$

In the low-cooperativity regime, this transparency window can be seen as originating from an additional narrow-band optical loss mechanism caused by the transduction of optical fields into the microwave mode. As the cooperativity increases, the transparency window grows until two distinct resonance features can be seen. This corresponds to the onset of strong coupling where $g > \kappa_m, \kappa_o$ and distinct hybrid electro-optic modes can be observed.

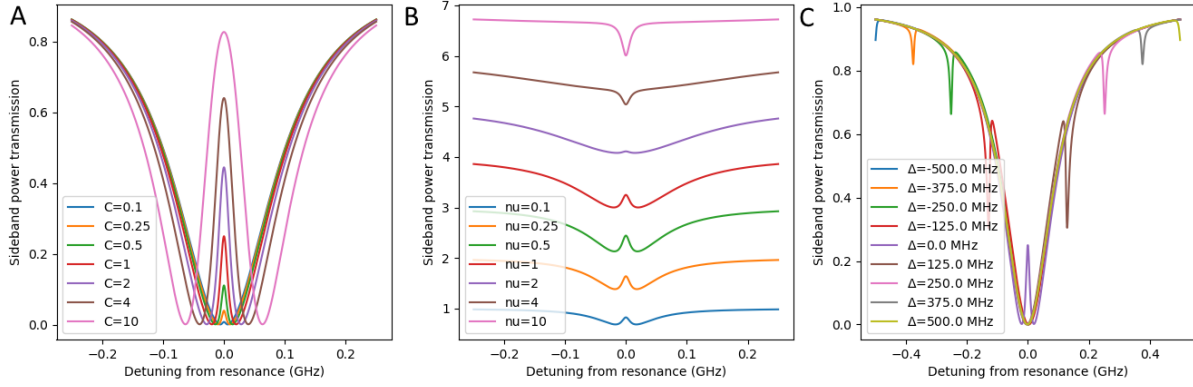


Figure 2.5: Calculated EIT spectra for different system parameters. All plots show $\kappa_m = 2\pi * 8\text{MHz}$, and $\kappa_{+,i} = 200\text{MHz}$. A) Sweep of cooperativity for optical critical coupling and exact triple resonance condition. B) Sweep of optical coupling factor $\nu = \frac{\kappa_{+,e}}{\kappa_{+,i}}$ for $C = 1$ and exact triple resonance condition. C) Sweep of triple resonance detuning Δ for $C = 1$ and optical critical coupling. See ideal_EIT.py.

2.2.3.3 Device Performance

One key metric for achieving useful device performance is the cooperativity C . Here, we will summarize the results required to predict the cooperativity of a particular device.

The pump-enhanced interaction strength is given by

$$g = g_0 \sqrt{n_{\text{pump}}} \quad (2.49)$$

where $n_{\text{pump}} = \frac{\kappa_{-,e}}{\Delta_-^2 + (\kappa_-/2)^2} \frac{P}{\hbar\omega_-}$ is the circulating field in the pumped mode, and P is the pump power in the coupling waveguide.

In the case of resonant pumping, the cooperativity reduces to

$$C = \frac{4g_0^2}{\kappa_+ \kappa_m} \frac{4\kappa_{-,e} P}{\kappa_-^2 \hbar\omega_-}. \quad (2.50)$$

The pump power required to realize a cooperativity of $C = 1$ is

$$P(C = 1) = \frac{\kappa_+ \kappa_- \kappa_m}{16g_0^2} \frac{1 + \nu_-}{\nu_-} \hbar\omega_-, \quad (2.51)$$

where $\nu_- = \kappa_{-,e}/\kappa_{-,i}$ is the optical coupling ratio. This pump power is a key figure of merit for electro-optic transducers because high pump power adds heat load to the cryostat sys-

tem¹⁶ and can cause optical-absorption related noise in the microwave resonator. We see from Equation 2.51 that to achieve high transduction efficiency while minimizing pump power, it is critical to create a device with strong electro-optic coupling and low losses in the microwave and optical resonators.

2.2.4 Thermal microwave noise

The strong pump light field can be absorbed in the waveguide or chip packaging, increasing the local device temperature above the base temperature measured using a temperature probe in the cryostat. Additionally, scattered pump light can be absorbed in the superconducting resonator, creating a quasiparticle bath that leads to excess loss and high thermal noise inside the microwave mode. In this section, we calculate the thermal occupation and radiation from a transducer connected to thermal baths with elevated temperatures. These results will be used to analyze thermal noise measurements in Chapter 5.

For simplicity, we consider the low-cooperativity limit where we can focus on the dynamics of the microwave mode given by the Fourier-domain Heisenberg-Langevin equation (compare Eq. 2.42)

$$\hat{b}[\omega] = \frac{-\sqrt{\kappa_{m,e}}\hat{b}_{wg}[\omega] - \sqrt{\kappa_{m,i}}\hat{b}_f[\omega]}{i\Delta - \kappa_m/2}, \quad (2.52)$$

where \hat{b}_{wg} is the field input from the waveguide¹⁷ and \hat{b}_f is the fluctuation operator corresponding to bath modes that are intrinsically coupled to the resonator. The power spectral density of the microwave mode is given by

$$\langle \hat{b}^\dagger[\omega]\hat{b}[\omega] \rangle = \frac{\kappa_{m,e}N_{wg} + \kappa_{m,i}N_f}{\Delta^2 + \frac{\kappa_m^2}{4}}, \quad (2.53)$$

where $N_i = \langle \hat{b}_i^\dagger[\omega]\hat{b}_i[\omega] \rangle$, $i = \{wg, f\}$ is the power spectral density of the input operators¹⁸.

¹⁶The typical cooling power of a dilution refrigerator is $100 \mu\text{W}$ at the low temperatures $T \sim 100 \text{mK}$ required to perform transduction at the microwave ground state.

¹⁷Note that \hat{b}_{wg} is the same as \hat{b}_{in} defined earlier. We use slightly different notation here to emphasize the physical origin of this noise source.

¹⁸Note that the power spectral densities $N_{\{wg,f\}}$ are dimensionless quantities, but should be thought

The average thermal occupation of the microwave mode N_m can be calculated by applying an inverse Fourier transform, yielding

$$N_m = \frac{\kappa_{m,e}}{\kappa_m} N_{wg} + \frac{\kappa_{m,i}}{\kappa_m} N_f \quad (2.54)$$

Unsurprisingly, the microwave mode occupancy N_m is simply an average of the occupancy of the thermal baths it is connected to, weighted by the relevant loss rates. This microwave mode occupancy is an important parameter because we typically require $N_m \ll 1$ to observe few-photon quantum effects with high fidelity (such as those described in Chapter 6).

The noise spectrum at the microwave output waveguide port can be calculated by combining Eq. 2.52 with the input-output relationship in Eq. 2.43 to find

$$N_{\text{out}}(\Delta) = \left\langle \hat{b}_{\text{out}}^\dagger[\omega] \hat{b}_{\text{out}}[\omega] \right\rangle = N_{wg} + \frac{\kappa_{m,i} \kappa_{m,e}}{\Delta^2 + \kappa_m^2/4} (N_f - N_{wg}). \quad (2.55)$$

This Lorentzian relationship can be used to infer the microwave mode occupancy from the measured output noise spectrum. Note that the microwave resonators in our actual devices are coupled to traveling modes propagating in two directions. Nonetheless, the theory described above can still be used to analyze our devices with a simple change of variables, as described in Appendix B.1.

of as the power coming from the thermal bath with units of photons/sec/Hz

Chapter 3

Microwave-to-optical transduction using cavity electro-optics in thin-film lithium niobate

3.1 Introduction

In this chapter, we describe an electro-optic transducer made from a thin-film lithium niobate photonic molecule [83, 123] integrated with a superconducting microwave resonator and demonstrate an on-chip transduction efficiency of greater than $10^{-6}/\mu\text{W}$ of optical pump power for continuous-wave signals.

Despite the promising properties of the thin-film lithium niobate platform, this power-normalized efficiency is comparable to that achieved in previous electro-optic transducers [64, 66, 84]. This is partly due to parasitic piezoelectric coupling that causes excess microwave resonator loss. Our transducer is designed to reduce this coupling, but doing so requires a sub-optimal electrode layout and still yields a relatively low microwave $Q \sim 10^3$. However, we show that with straightforward improvements — including better acoustic engineering — the efficiency can be increased to near unity for $\sim 100 \mu\text{W}$ of optical pump power. Outside

its potential for high transduction efficiency and low noise, our platform has several other advantages for making a practical microwave-optical transducer. First, the small footprint ($\sim 1\text{mm}^2$) compared to bulk electro-optic transducers enables multiplexed designs for high rate quantum communication [19, 20]. Second, the triple-resonance photonic molecule design of our device makes it easy to design for a particular transduction frequency. Finally, low-loss tunable filters can be integrated on-chip with our device to reduce filtering losses in transduction protocols [124].

3.2 Device design and characterization

The operating principle of our transducer is illustrated in Fig. 3.1(a). Two lithium niobate optical ring resonators are evanescently coupled to create a pair of hybrid photonic-molecule modes, with a strong optical pump signal tuned to the red optical mode at ω_- . A superconducting microwave resonator with resonance frequency ω_m modulates the optical pump signal, upconverting photons from the microwave resonator to the blue optical mode at ω_+ .

This transduction process is phase-coherent and can be described by a beamsplitter interaction Hamiltonian

$$H_I = \hbar g_0 \sqrt{n_-} (b^\dagger a_+ + b a_+^\dagger), \quad (3.1)$$

where g_0 is the single-photon electro-optic interaction strength, n_- is the number of (pump) photons in the red optical mode, while b and a_+ are the annihilation operators for the microwave and blue optical modes, respectively. The interaction strength g_0 is determined by the microwave resonator's total capacitance, the overlap between microwave and optical modes, as well as the electro-optic coefficient of the host material. We use a thin-film superconducting LC resonator and an integrated lithium niobate racetrack resonator [103] to optimize this interaction strength, which we estimate to be $g_0 = 2\pi \times 850\text{ Hz}$. The on-chip transduction efficiency η for continuous-wave signals depends on both this interaction strength and the loss

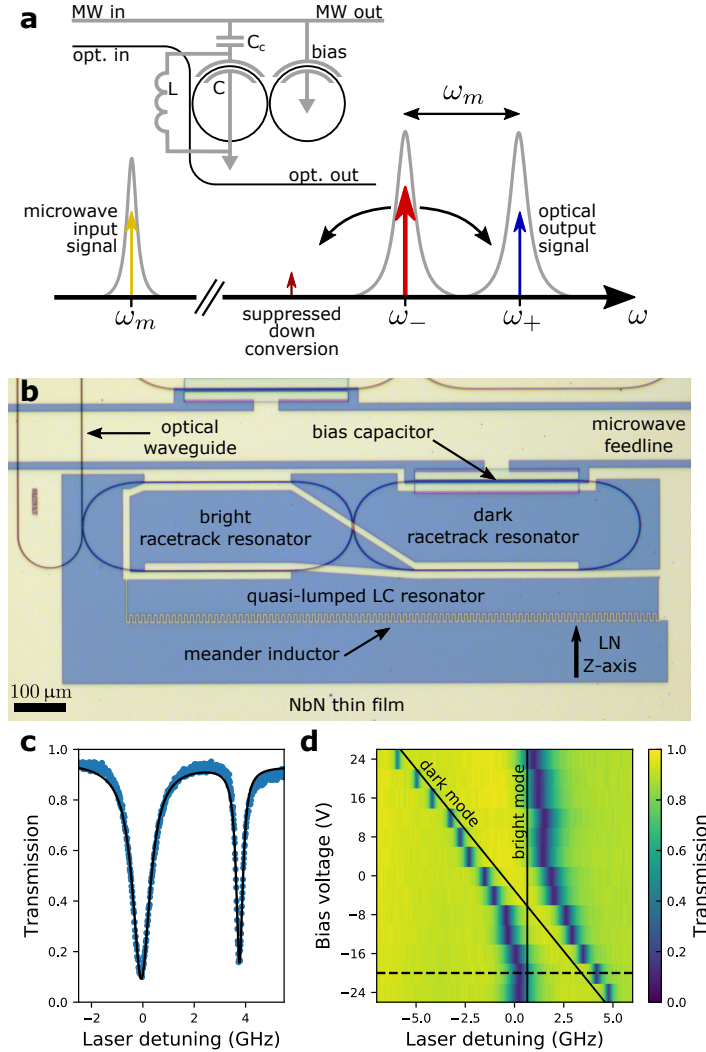


Figure 3.1: A superconducting cavity electro-optic transducer on thin-film lithium niobate. (a) Top: Device schematic. Black and grey lines represent optical waveguides and superconducting wires, respectively. The coupled optical ring resonators are modulated by a microwave (MW) resonator (made from inductor L and capacitor C) that is capacitively coupled to the bus (C_c). The optical resonance frequencies can be tuned by a bias capacitor. Bottom: Frequency-domain diagram of the transduction scheme. A pump laser is tuned into resonance with the red optical mode at ω_- . Photons in the microwave resonator at ω_m can be upconverted to the blue optical mode at ω_+ by sum-frequency generation. (b) Optical micrograph of the transducer, showing optical waveguides (black) and the niobium nitride superconducting film (light yellow). The capacitor of the quasi-lumped LC resonator modulates the optical racetrack resonators. A DC voltage on the microwave feedline controls the detuning between optical modes. (c) Optical transmission spectrum near 1586 nm of a pair of photonic-molecule optical modes with a -20 V bias. (d) Optical transmission spectra at other bias voltages display an anticrossing between modes in the bright and dark racetrack resonators. Dashed line shows data in (c).

rates of the modes (see Chapter 2),

$$\eta = \frac{\kappa_{m,\text{ex}}\kappa_{+,\text{ex}}}{\kappa_m\kappa_+} \times \frac{4C}{(1+C)^2}, \quad (3.2)$$

where $(\kappa_{m,\text{ex}}, \kappa_m)$ and $(\kappa_{+,\text{ex}}, \kappa_+)$ are the external and total loss rates for the microwave and blue optical modes, respectively, and $C = \frac{4g_0^2 n_-}{\kappa_m \kappa_+}$ is the cooperativity. The first term in Equation (3.2) represents the efficiency of a photon entering and exiting the transducer. To maximize this photon coupling efficiency, the resonators in our device are overcoupled.

A microscope image of our device is shown in Fig. 3.1(b). Light with TE-polarization is coupled from an optical fiber array onto the chip using grating couplers with ≈ 10 dB insertion loss. The photonic molecule optical modes are created using evanescently coupled racetrack resonators made from 1.2 μm -wide rib waveguides in thin-film lithium niobate atop a 4.7 μm -thick amorphous silicon dioxide layer on a silicon substrate. The optical waveguides are cladded with a 1.5 μm -thick layer of amorphous silicon dioxide. The fabrication process for these optical resonators is described in Appendix D.3.1. To create the superconducting resonator, a ≈ 40 nm-thick niobium nitride film is deposited on top of the cladding by DC magnetron sputtering [125] and patterned using photolithography followed by CF_4 reactive ion etching. Details of the design and properties of the LC resonator are provided in Appendix C.2. The detuning between the optical modes can be controlled using a bias capacitor on the dark (i.e. not directly coupled to the bus waveguide) racetrack resonator.

The optical transmission spectrum displayed in Fig. 3.1c shows a typical pair of quasi-TE photonic-molecule optical modes. As shown in Fig. 3.1d, we observe a clear anticrossing between bright and dark resonator modes when tuning the bias voltage and measure a minimum optical mode splitting of 3.1 GHz. By measuring the resonance linewidths as a function of bias voltage (see Eq. 2.36), we infer that the unhybridized bright and dark optical modes have internal loss rates of $\kappa_{\text{bright,in}} = 2\pi \times 350$ MHz and $\kappa_{\text{dark,in}} = 2\pi \times 150$ MHz, respectively, and that the bright mode has an external loss rate $\kappa_{\text{bright,ex}} = 670$ MHz. In this work, we use several pairs of optical modes for microwave to optical transduction measurements. To understand the variability of optical loss across resonances in our device, we performed similar mea-

measurements on quasi-TE resonances between 1584 – 1593 nm and found the mean and standard deviation of the loss rates to be $\kappa_{\text{bright,in}} = 2\pi \times (170 \pm 70)$ MHz, $\kappa_{\text{dark,in}} = 2\pi \times (200 \pm 60)$ MHz, and $\kappa_{\text{bright,ex}} = (830 \pm 300)$ MHz. These results correspond to an average internal quality factor of $Q_i \approx 10^6$.

Lithium niobate has a strong piezoelectric susceptibility, which gives the microwave resonator a loss channel to traveling acoustic modes [126]. To investigate this loss mechanism, we perform a two-dimensional simulation of a cross section of the waveguide and resonator capacitor (see Appendix C.2). The simulated intrinsic microwave quality factor due to piezoelectric loss displays a strong frequency dependence, as shown in Fig. 3.2(a). This frequency dependence is caused by low quality-factor bulk acoustic modes — illustrated in Fig. 3.2(b) — that form in the thin-film layers of our device, which resonantly enhance the coupling between the microwave resonator and acoustic fields. Lower loss can be achieved by designing the microwave resonance frequency to avoid the bulk acoustic resonances. The relative orientation of the capacitor and the lithium niobate crystal axes also influences the microwave loss. Figure 3.2(c) shows that the intrinsic microwave quality factor is maximized when the electric field produced by the capacitor is oriented close to the Z-axis of the lithium niobate crystal, which is also the condition that maximizes electro-optic response. Using these considerations, we designed a microwave resonator that has a measured intrinsic quality factor of $Q_i = 1100$ at a temperature of 1 K, as shown in Fig. 3.2(d). In addition to piezoelectric effects, we also estimate that dielectric loss in the amorphous silicon dioxide cladding contributes an added loss of $Q_{\text{clad}} \sim 2000$ to the resonator (see Appendix C.2). This dielectric loss can be reduced by changing the electrode design to minimize the participation fraction of the amorphous cladding, or using lower loss cladding materials [127].

3.3 Microwave to optical transduction

To measure the transduction efficiency of our device, we locked the frequency of the pump to be near-resonant with the red optical mode (side-of-fringe locking) and sent a resonant mi-

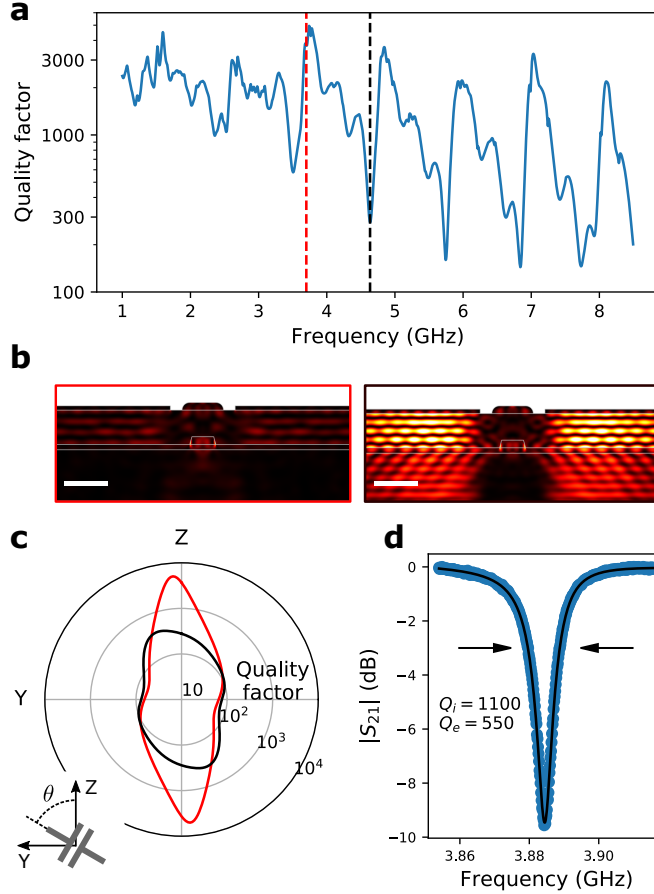


Figure 3.2: Piezoelectric loss in thin-film lithium niobate. (a) Frequency dependence of the simulated microwave resonance loss caused by piezoelectric coupling to acoustic modes. Frequencies near bulk acoustic wave modes (e.g. black dashed line at 4.6 GHz) display strong loss, but relatively low-loss performance can be achieved for frequencies far detuned from bulk acoustic modes (e.g. red dashed line at 3.7 GHz). (b) Simulated acoustic energy density profiles of the device cross section for 3.7 GHz (red border) and 4.6 GHz (black border). White scale bars are $2\ \mu\text{m}$ long. (c) Simulated microwave quality factor for different orientations of the capacitor with respect to the crystal axes of lithium niobate, at 3.7 GHz (red) and 4.6 GHz (black). (d) The measured microwave transmission spectrum of the microwave resonator at a temperature $T = 1\ \text{K}$.

crowave signal into the device. The pump and upconverted optical signal were collected and sent to an amplified photodetector, which produced a beat note at the input microwave frequency. We inferred the on-chip transduction efficiency from this beat note power by calibrating the input optical power, system losses, and detector efficiency (see Section D.1). During this transduction efficiency measurement, we swept the bias voltage in a triangle waveform with a period of $\approx 1\ \text{min}$ to vary the splitting between the optical modes. The pump light re-

mained locked to the red optical mode throughout the measurement. Figure 3.3(a) illustrates the optical modes and signals throughout the bias voltage sweep.

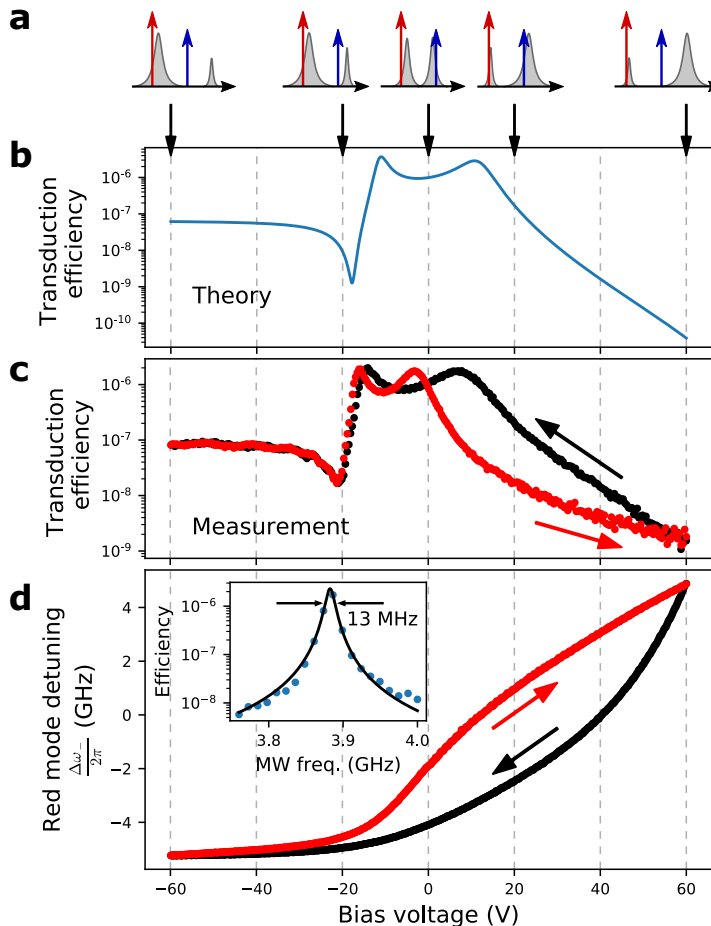


Figure 3.3: Detuning dependence of microwave-to-optical photon transduction. (a) Frequency-domain illustrations of the optical modes for the bias voltages indicated by the downward-facing arrows. (b) Predicted dependence of the on-chip transduction efficiency on the bias voltage. This prediction is based on a model that includes transduction into both the red and blue optical modes, and independently measured and calculated device parameters. (c) Measured dependence of the on-chip transduction efficiency on the bias voltage. Red and black traces correspond to sweeps of increasing and decreasing voltage, respectively. (d) The red optical mode frequency detuning induced by the bias voltage during the transduction experiment. Inset: The dependence of the highest on-chip transduction efficiency on the frequency of the microwave drive displays a wide bandwidth of 13 MHz. All data shown for -30 dBm on-chip optical pump power.

The results of this measurement are depicted in Fig. 3.3. The two maxima in transduction efficiency near ± 10 V (Figs. 3.3(b) and (c)) correspond to the cases where the triple-resonance condition is met and the upconverted light is resonant with the blue optical mode. The shape

of the optical anticrossing ensures this triple-resonance condition is met twice in the voltage sweep. For large negative bias voltages, the blue mode is far-detuned, and most of the upconverted light is generated in the red optical mode by a double-resonance process involving just the red optical mode and the microwave mode (see Appendix B.2). This process does not depend on the resonance frequency of the blue optical mode, so the transduction efficiency is nearly independent of the bias voltage in this regime. Destructive interference of upconverted light produced in the red and blue optical modes (created by double- and triple-resonance processes, respectively) causes the transduction efficiency minimum near -20V . For large positive bias voltage, the red optical mode is undercoupled and has a narrow linewidth, so the double-resonance transduction process is weak. The measured data presented in Fig. 3.3(c) shows good correspondence to our analytical model shown in Fig. 3.3(b) (Eq. in Appendix B.2), which is based on independently measured and estimated device parameters.

As shown in Fig. 3.3(d), the frequency of the optical modes displays hysteresis when changing the bias voltage, which also causes the efficiency hysteresis in Fig. 3.3(c). We observed that this hysteresis could be reduced by lowering the optical pump power and sweeping the voltage bias faster. Based on the slow timescale (seconds for -30 dBm on-chip optical pump power), we attribute the hysteresis to photoconductive and photorefractive effects in lithium niobate [128]. These effects are caused by optical excitation of charge carriers from defects in the lithium niobate waveguide. These carriers migrate and create built-in electric fields that shift the optical resonance frequencies through the electro-optic effect. Such photorefractive and photoconductive effects are known to be stronger and to operate at faster timescales in thin-film lithium niobate than in bulk devices [129, 130]. In practice, these effects can be overcome by using pulsed-pump schemes to reduce carrier generation (see high power measurements below), modulating the bias voltage to prevent complete shielding of the bias field, and locking the laser to the optical resonances. We study the impact of photoconductive and photorefractive effects on the low-frequency electro-optic response of thin-film lithium niobate devices in Chapter 4.

We measured the bandwidth of the transducer by varying the frequency of the input mi-

crowave drive and measuring the highest transduction efficiency reached during a bias voltage sweep. The inset of Fig. 3.3(d) shows that our transducer has a 3 dB bandwidth of 13 MHz, slightly larger than the measured 10 MHz linewidth of the microwave resonator. This discrepancy is caused by the nonlinear response of the NbN microwave resonator for high microwave power, which leads to an apparent resonance broadening [131] (see Section C.2.1). To reduce measurement noise, here we use a relatively large microwave power (-38 dBm on-chip), which causes a small degree of nonlinear broadening. This nonlinearity also leads to reduced transduction efficiency for large input microwave powers (Fig. 3.4(a) inset).

Figure 3.4(a) shows the highest on-chip transduction efficiency measured during a bias voltage sweep for different optical pump powers. During this measurement, we found that the zero-bias detuning between the optical modes could change by several GHz when the optical pump power was varied, likely due to the photoconductive and photorefractive effects described earlier. To measure the transduction efficiency at the triple-resonance point for each power level, we performed measurements on several pairs of photonic-molecule modes. For the highest optical pump powers used in this study (denoted by crosses in Fig. 3.4(a)), we modulated the optical pump to extinction at a rate of 20 kHz and with a 10% duty cycle. The lower average power in these modulated-pump measurements resulted in smaller power-dependent detunings and more stable resonances.

In the low-power regime (< -30 dBm) we observe that the transduction efficiency scales linearly with pump power at a rate of $(1.9 \pm 0.4) \times 10^{-6}/\mu\text{W}$. From this and the measured loss rates of the resonators, we estimate the single-photon coupling rate of our transducer to be $g_0 = 2\pi \times 650 \pm 80$ Hz.

Table 3.1: Transducer device parameters for calculating the electro-optic interaction strength

Parameter	Value	Estimation method
Γ	0.93	Optical mode simulation
α	0.72	Calculated from device geometry
d_{eff}	15 μm	EO cross section simulation
C	120 fF	Full-wave simulation as in [132]
θ	0.7π	Inferred from hybrid mode splitting

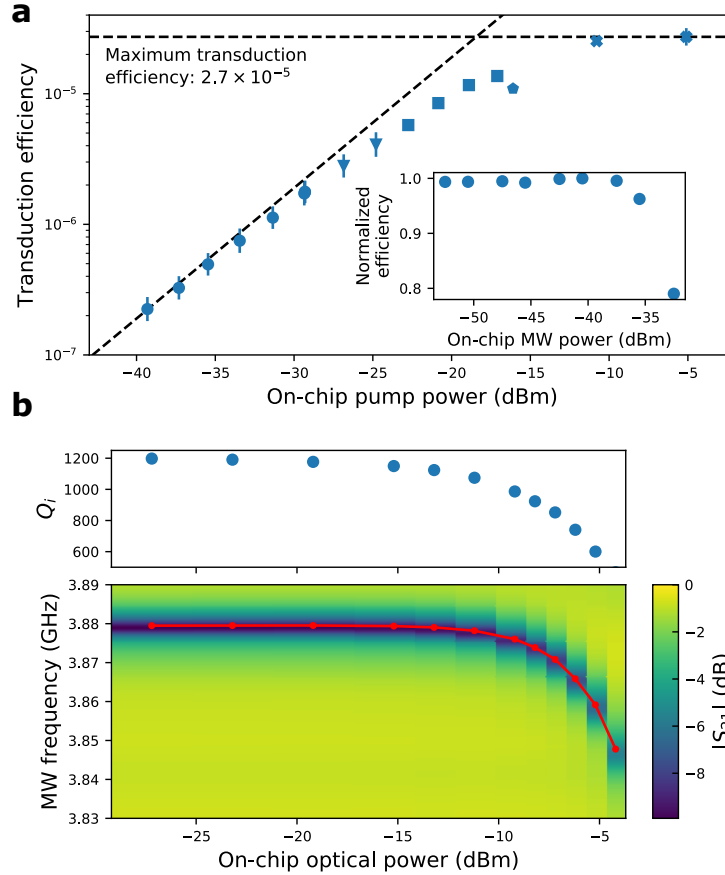


Figure 3.4: Power dependence of microwave-to-optical photon transduction. (a) The maximum on-chip transduction efficiency measured during a sweep of the bias voltage for different optical pump powers. The different markers (circles, triangles, etc.) correspond to sets of measurements performed on different optical modes - see main text for details. Inset: The dependence of the transduction efficiency on microwave input power for -30 dBm on-chip optical pump power. (b) Degradation of the microwave resonator due to absorption of pump light. The plots show the optical power dependence of the microwave transmission spectrum (bottom, red line denotes resonance frequency) and the inferred intrinsic microwave quality factor (top).

This measured coupling rate is comparable to the value of $g_0 = 2\pi \times 850$ Hz estimated using Eq. 2.16 and the device parameters in Table 3.1, yet slightly lower than expected. This difference is likely due to variations in the as-fabricated geometry of the device.

The on-chip transduction efficiency begins to saturate at $(2.7 \pm 0.3) \times 10^{-5}$, the highest-measured efficiency for this transducer. This saturation is caused by optical absorption in the microwave resonator, which generates quasiparticles that shift the resonance frequency and increase the loss rate of the resonator [133]. Figure 3.4(b) shows the optical-power dependence

of the microwave resonator’s properties. We find that the quasiparticle-induced changes in the microwave resonator are independent of whether the pump laser is tuned on- or off-resonance with an optical mode, which suggests that the absorbed light does not come from the optical resonator itself. Instead, stray light scattered at the fiber array and grating couplers is the dominant contribution to the quasiparticle loss.

Note that although we did not demonstrate optical-to-microwave transduction (only microwave-to-optical) due to a low signal-to-noise ratio, the electro-optic transduction process is fully bidirectional (as shown in Chapter 2).

3.4 Discussion

The transduction efficiency demonstrated here falls well below the requirements for a useful quantum transducer. However, the straightforward changes to the transducer shown in Table 3.2 can greatly improve this figure of merit. First, optical quality factors above 10^7 have been demonstrated in thin-film lithium niobate [105], suggesting that the optical loss rates seen here can be reduced by roughly 10-fold, leading to a 100-fold improvement in transduction efficiency. Second, the microwave resonator loss rate can be reduced through improved engineering of the bulk acoustic waves to which the microwave resonator couples and the elimination of amorphous cladding materials. For example, simulations suggest that suspending the lithium niobate layer can reduce the microwave loss by more than 10-fold. Third, the optically-induced quasiparticle losses can be greatly reduced by changing the design of the sample mount and optical fiber coupling to shield the microwave resonator from stray scattered light. Fourth, the electrode coverage fraction of the microwave resonator can be improved by at least 2-fold, for example by using a higher aspect ratio racetrack resonator, extending coverage to curved sections of the waveguides, and integrating the bias capacitor with the resonator. Fifth, using single-sided microwave coupling (as opposed to the two-sided coupling used here, where the cavity field is coupled to both right and left propagating modes) would eliminate an effective loss channel. Sixth, the capacitance of the microwave resonator

can be reduced, increasing the single-photon electro-optic coupling rate. Straightforward ways to do this might include using higher-impedance spiral inductors or nesting the two optical resonators to reduce overall device size and parasitic capacitance. Photonic crystal modulators [134] could enable significantly smaller device footprint and microwave capacitance (in conjunction with high-impedance inductors), but may involve trade-offs in terms of optical loss and photoconductive effects. Finally, the optical pump can be tuned on-resonance with the optical mode, increasing the pump-enhanced coupling rate.

By implementing these changes (see Table 3.2 for details), we predict that near-unity transduction efficiency can be achieved for optical pump powers of $\sim 100 \mu\text{W}$.

Table 3.2: Predicted improvements in device parameters

Parameter	Improvement factor	Efficiency enhancement	Notes
κ_{optical}	10	10^2	Optical quality factor $Q = 10^7$ By suspending lithium niobate layer
κ_m	10	10	
Block scattered light	-	10	For 100 μW of on-chip pump power
Electrode coverage	2	4	
Single-sided MW coupling	2	2	Improves effective MW loss
Microwave capacitance	2	1.5	Using a high-impedance inductor
Resonant optical pump	-	1.5	
Total		$\sim 10^5$	

In this chapter, we have demonstrated transduction between microwave and optical frequencies using a thin-film lithium niobate device. The photonic molecule design of our transducer enables straightforward tuning of the optical modes using a bias voltage, ensures strong suppression of the downconverted light that acts as a noise source, and takes full advantage of the large electro-optic coefficient in lithium niobate. We have described how the piezoelectric coupling of the microwave resonator to traveling acoustic waves can be engineered to minimize loss in the microwave resonator. The advantages of an electro-optic transducer — namely the

system simplicity, the promise for low-noise operation, and the possibility for on-chip filter integration — and the opportunities for improved transduction efficiency motivate further development of thin-film lithium niobate cavity electro-optics.

Chapter 4

Charge carrier effects in thin-film lithium niobate

The free-carrier effects on the low-frequency and DC electro-optic response in thin-film lithium niobate identified in Chapter 3 pose an important challenge to the use of cavity electro-optic transducers. Stable operation at or near the triple-resonance condition is critical to future large-scale applications of such transducer. However, this requires that the electro-optic response of the bias capacitor persists for long periods. Free carrier migration makes this challenging because any applied electric field will be shielded over long timescales. In this chapter, we measure the dielectric relaxation timescale on which the applied field is screened to be $O(1\text{ ms})$ in fully cladded devices. This decay of electro-optic tuning is a problem for any device in TFLN where DC phase offset control is required, such as amplitude and IQ modulators [103, 135]. While other methods such as thermo-optic tuning can be used in room-temperature devices [136], this comes at the cost of higher power and lower tuning bandwidth. For this reason, improving the low-frequency electro-optic response is a key challenge toward realizing the potential of TFLN integrated devices in general.

Poor low-frequency EO response and drift due to charge carrier migration have been widely studied in bulk LN devices [137–142], as well as other electro-optic photonic material platforms [143, 144]. In TFLN devices, the frequency at which EO response is suppressed is much

higher than in bulk devices [136, 145], which is consistent with the observation of faster photorefractive response in TFLN [129]. However, to date, there has been little study of the underlying mechanism or how the EO bias response can be improved at low frequencies.

In this chapter, we aim to address these questions and explore the causes and amelioration of the observed drop in the electro-optic response of TFLN devices at low frequencies. By measuring devices with different electrode geometries, using finite element models to estimate the frequency response, and comparing our estimated device conductivities with previous studies in bulk LN, we find evidence that the carrier migration occurs primarily at the top surface of the LN film in cladded device, in a thin layer with surface conductivity of approximately $\kappa_s \sim 10^{-11}$ S. We perform temperature-dependent measurements to help validate charge carriers as the origin of the reduced EO response and measure the activation energy of the conductivity, which may help determine the microscopic origin of the free carriers. Finally, we study several ways in which the low-frequency EO response can be improved, including different electrode designs, annealing procedures, and operation at low temperatures. We find that these interventions can enhance effective operation frequency by several orders of magnitude. Although further work can be done to verify the surface-based origin of charge conduction and develop better techniques to enhance low-frequency EO response, here we identify several interventions that make the use of low-power electro-optic tuning in TFLN devices at low frequency feasible.

4.1 Measurement setup

To probe the electro-optic frequency response of our devices, we use a Mach-Zehnder optical amplitude modulator (MZM) illustrated in Figure 4.1b as an example testbed device. Figure 4.1a shows the fabrication process for our devices. Using argon-based reactive ion etching, we define $1.5 \mu\text{m}$ wide waveguides into a commercial thin-film lithium niobate wafer from NanoLN with 600 nm LN film thickness, a $4.7 \mu\text{m}$ silicon dioxide buried cladding layer formed by thermal growth, and a $525 \mu\text{m}$ thick high resistivity ($> 10 \text{ k}\Omega\text{cm}$) silicon substrate. After

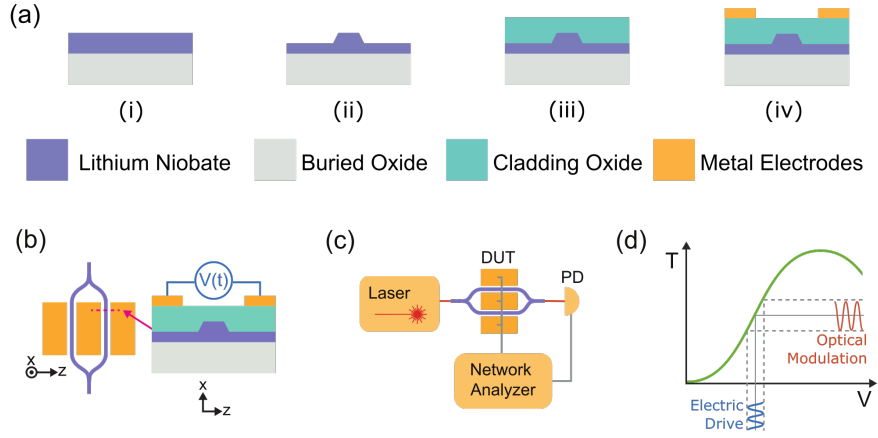


Figure 4.1: Characterization setup for low-frequency electro-optic response in thin-film lithium niobate. (a) Device fabrication steps: (i) the initial TFLN substrate, (ii) a ridge waveguide is patterned and etched into the optical layer, (iii) an oxide cladding is deposited to cover the waveguide, (iv) metal electrodes are deposited. (b) Left: A schematic top view of a Mach-Zehnder amplitude modulator in TFLN. Right: Cross-section of the electrode. A voltage drive signal $V(t)$ is applied to the electrodes to induce an optical phase change in each arm, which can be measured as a change in optical intensity at the output of the Mach-Zehnder modulator. (c) A schematic of the experimental setup, where polarized light is injected into the device-under-test (DUT), a network analyzer applies a probe signal to the device, and the device’s electro-optic response is read out as intensity fluctuations on a photodetector (PD). (d) The transfer function of the modulator. In these experiments, a single-tone weak electrical drive is applied around the quadrature point of the modulator (where the electro-optic amplitude response is approximately linear) and the optical modulation is measured.

etching, we use plasma-enhanced chemical vapor deposition to clad the device with $1.2 \mu\text{m}$ of silicon dioxide and deposit 15 nm of titanium and 800 nm of gold for electrodes that are $100 \mu\text{m}$ wide with $5.5 \mu\text{m}$ gaps between them.

Figure 4.1c shows the experimental setup. Polarized CW laser light (wavelength 1550 to 1630 nm) is injected onto the chip, passes through the device, and is collected at a photodetector. Light is coupled to and from the device via a fiber array and on-chip grating couplers with roughly 10 dB insertion loss per coupler. A network analyzer is used to electrically drive the modulator (drive amplitude $|V| < 0.1V_\pi$) and record the modulation response (illustrated in Fig. 4.1d) on the photodetector V_{PD} to calculate the electro-optic response, which we define as $G = V_{\text{PD}}/V$. The sinusoidal EO transfer function of our MZM is shown in Fig. 4.1d. To consistently measure the relative EO-response across devices, we operate each device at the quadrature point, where the linear EO-response (slope of transfer function) is maximized. We use an MZM with unbalanced arm lengths so that the quadrature point can be reached

by changing the laser wavelength instead of using a DC bias. We consistently find across all devices that the electro-optic response is nearly constant at high frequencies (measured at 100 kHz to 1 MHz), and use this high-frequency value of G to normalize the data for comparison across devices, except where otherwise noted.

4.2 Dielectric relaxation

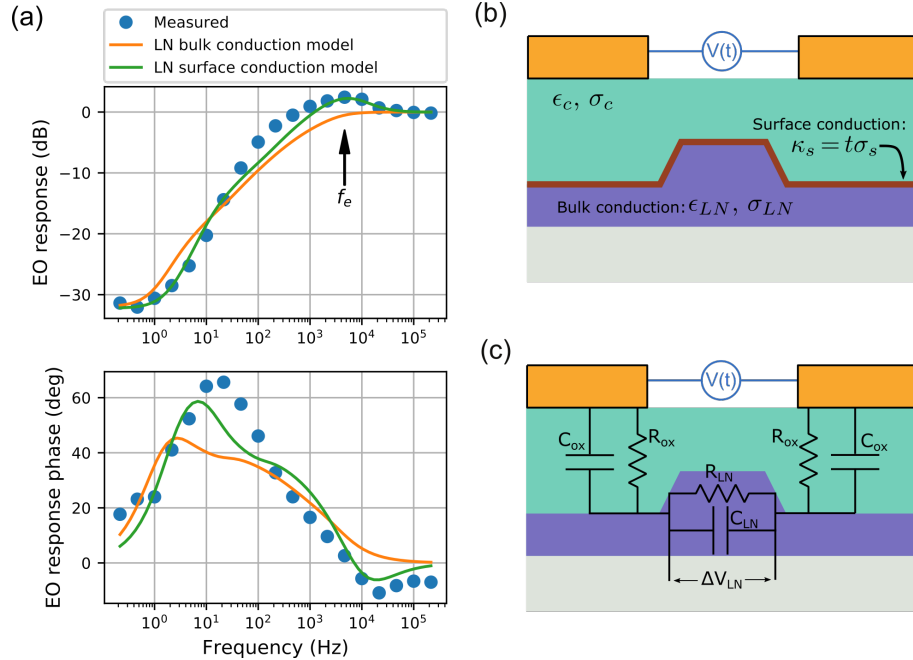


Figure 4.2: Measurement and modeling of low-frequency electro-optic response in thin-film lithium niobate. (a) Measured EO response (circles) of a device in the low-frequency regime. We observe strong suppression of EO response at frequencies below 100 Hz and poor response flatness at frequencies near the enhancement feature at frequency f_e . Solid lines show the results of two-dimensional finite element models of our devices using either bulk conductivity ($\sigma_{LN} \neq 0$) or surface conductivity ($\kappa_s \neq 0$) models. (b) Schematic of our finite element model showing material parameters. (c) Schematic of a lumped-element model to explain the impact of bulk conduction on the EO response. We model the capacitive and resistive properties of the silicon oxide cladding and LN waveguide using lumped-element parameters $C_{ox,LN}$ and $R_{ox,LN}$, respectively. The voltage drop across the LN waveguide ΔV_{LN} is proportional to the electric field applied to the waveguide.

Figure 4.2a shows the frequency dependence of the electro-optic response for a fully cladded device. At frequencies below roughly 100 Hz the EO response is strongly suppressed. In the time domain, this means the electro-optic effect induced by an applied electrode voltage decays over a few milliseconds. Furthermore, even for frequencies above 100 Hz, we observe poor

response flatness around an enhancement feature near frequency f_e , where the EO response amplitude is enhanced compared to the high-frequency value by roughly 2.5 dB. This poor frequency flatness can be difficult to compensate for in some applications. This chapter seeks to explain these two effects – the low-frequency suppression and poor flatness of EO response – and develop methods by which they can be eliminated or improved.

Building on previous work in bulk LN modulators, we attribute these effects to the movement of charge carriers within our device [137, 138]. Carriers can screen applied electric fields at timescales below the dielectric relaxation time $\tau = \epsilon_r \epsilon_0 / \sigma$ (where σ is the conductivity, and $\epsilon_r \epsilon_0$ is the permittivity) of the material. This screening effect leads to reduced EO response in our devices.

Here we will quantitatively compare two possible models for carrier migration in our devices: conduction within the bulk of the LN layer, and conduction at the top etched surface of the LN layer at the cladding interface. If we can determine where and how carrier migration occurs, this information can guide the development of devices with improved low-frequency EO response. It has been shown in previous work that the location of free charge carriers within bulk LN devices can be determined by comparing measured and predicted EO response [142].

To compare these models to our measured data, we use a two-dimensional numerical simulation and fit the simulated EO response to our measured data in Fig. 4.2a. Figure 4.2b illustrates the material parameters used in our simulation, where σ_i and ϵ_i are the conductivity and relative permittivity of different material layers in our device and $i = \{c, LN, s\}$ is an index referring to the cladding oxide, LN, or surface layer, respectively. The surface layer conductivity is defined as $\kappa_s = t\sigma_s$, where t is the thickness of the conducting surface layer, which is assumed to be small compared to other dimensions in our device.

Previous work on the low-frequency response of electro-optic devices has typically used lumped-element models like that shown in Fig. 4.2, which corresponds to the bulk conductivity model. In this lumped model, each material in the electrode region is treated as a parallel RC network. The time constant $\tau_i = R_i C_i$ can be compared to the dielectric relaxation

timescale in a dimensional model. The voltage drop across the waveguide ΔV_{LN} is proportional to the electric field in the waveguide. At high frequencies, the admittance of the capacitors dominates that of the resistors, and relatively large values of ΔV_{LN} can result because the geometry of the electrodes ensures $C_{ox} \sim C_{LN}$. However, in the low-frequency regime, resistive admittance dominates so that the waveguide voltage drop is $\Delta V_{LN} = \frac{R_{LN}}{R_{LN} + 2R_{ox}} V$. If the cladding resistivity is also much higher than that of the LN ($R_{ox} \gg R_{LN}$), then $V_{LN} \ll V$ and the electro-optic response will be suppressed. In a dimensional picture, this corresponds to charge carriers inside the LN migrating to the cladding interface and shielding the applied electric field inside the waveguide.

We can quantitatively connect this lumped-element model with the material parameters used in our dimensional model by treating the RC network as a complex capacitance network where the complex permittivity ϵ^* of each capacitor is given by $\epsilon_i^* = \epsilon_i + \frac{i\sigma_i}{\epsilon_0\omega}$. This permittivity is connected to the lumped-element parameters by the total complex capacitance $C^* = \epsilon_0 A_i \epsilon_i^* / d_i$, where A_i and d_i are the area and plate separation of a lumped-element parallel plate capacitor. Using these definitions, the EO response in the lumped-element model is given by

$$G = \alpha \frac{\Delta V_{LN}}{V} = \alpha \frac{\epsilon_{ox}^*}{\beta \epsilon_{LN}^* + \epsilon_{ox}^*}, \quad (4.1)$$

where α is an experimental proportionality constant, and $\beta = A_{LN} d_{ox} / A_{ox} d_{LN}$ is a geometric parameter. The key assumption in the lumped-element model is that the geometric parameter β is independent of the material permittivities. We test this assumption by using the finite element model to calculate the value of β for our device geometry using Eq. 4.1. We find that β can vary by more than 10-fold over the frequency range of interest with reasonable material parameters. This variability in β is caused by the reorientation of electric fields near the electrodes as the material permittivity changes, something that cannot happen in the lumped-element model. This reorientation causes significant quantitative differences between the predicted G in the lumped-element and dimensional models and motivates using a dimensional model when fitting measurement results to estimate material parameters, contrary to previous

work.

The solid lines in Fig. 4.2a show fits of our measured data to the simulations. The bulk conduction model assumes $\kappa_s=0$ and uses $\{\sigma_{LN}, \sigma_c\}$ as free parameters, while the surface conduction model takes $\sigma_{LN}=0$ and $\{\kappa_s, \sigma_c\}$ as free parameters.

The fit to the bulk conduction model yields estimates $\sigma_{LN}\sim 6*10^{-6}$ S/m and $\sigma_c\sim 2*10^{-10}$ S/m and qualitatively reproduces the strong reduction in EO response. However, the bulk conduction model does not explain the EO response enhancement feature that we observe near frequency f_e . Here we use a simple model for the complex permittivity of the LN layer based on frequency-independent values for the dielectric constant and conductivity. It is unlikely that a more complicated model of permittivity in the LN layer alone (for example, including Debye relaxation effects observed in bulk LN [146]) could explain the observed enhancement. This is because dielectric relaxation processes of all kinds tend to increase the permittivity of materials at lower frequencies [147], which would cause a reduction in EO response.

The fit to the surface conduction model yields estimates $\kappa_s\sim 10^{-11}$ S and $\sigma_c\sim 4 * 10^{-10}$ S/m and reproduces both the enhancement feature at f_e and reduction in EO response for low frequencies. The enhancement in EO response, in this case, is caused by a similar conductive-slab effect to that which can be achieved using doped silicon slot waveguides [79], although in our devices the conductive layer fully covers the waveguide and so acts as a Faraday shield at low frequencies, leading to strongly suppressed EO response. A complete discussion of the evidence for the surface and bulk conduction models is given in Section 4.6, but a comparison of the simulation results suggests the surface conduction model better reproduces the measured data.

4.3 Temperature dependence

To help validate charge conduction as the origin of the suppressed low-frequency response, we performed several measurements at cryogenic temperatures. These measurements also help us to better understand the low-frequency EO response in our transducers, which are typically

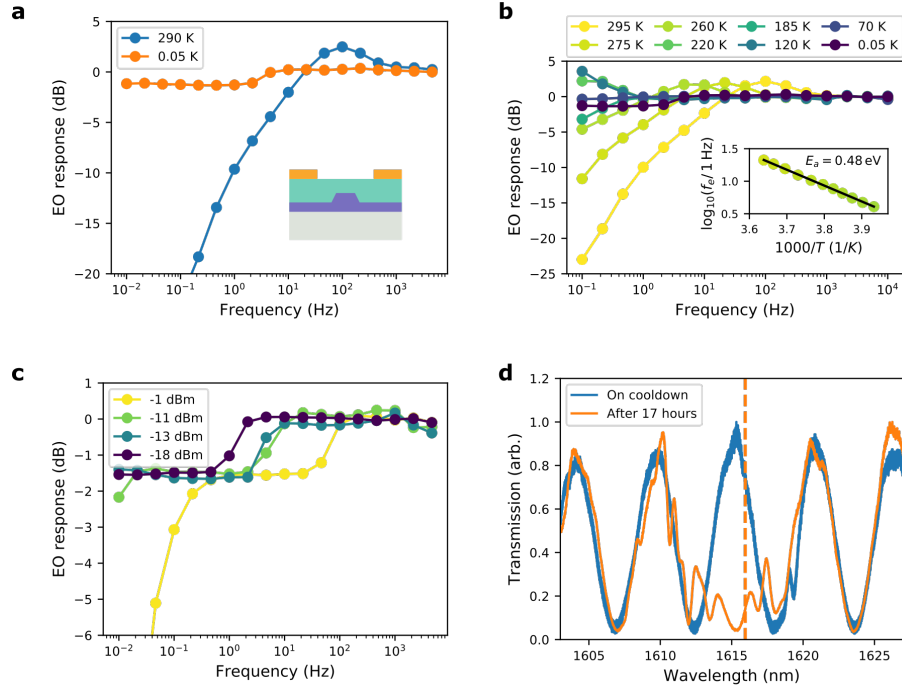


Figure 4.3: Device characterization at cryogenic temperatures. (a) Comparison of the low-frequency EO response of our devices at room temperature and 0.05 K. Inset: device cross section. (b) Impact of temperature on the EO response. Inset: dependence of the enhancement feature frequency f_e on temperature T . A fit to an Arrhenius model (black line) yields an activation energy $E_a=0.48 \text{ eV}$. (c) Impact of optical power on the EO response at a base temperature of 0.05 K. The legend shows the on-chip input optical power. (d) Illustration of photorefractivity induced optical gratings at a base temperature of 0.05 K. Blue curve shows the transmission spectrum shortly after cooldown to base temperature. Orange curve shows the transmission spectrum after 17 hours of measurement with the laser at a fixed wavelength (dashed vertical orange line) and -11 dBm on-chip input power.

operated at temperatures below 1 K. Besides electro-optic transducers, other devices such as modulators and optomechanical devices are also being investigated in thin-film lithium niobate for use at cryogenic temperatures, so the improvement of the EO response under such conditions is valuable for a variety of device applications [58,148].

In the dielectric relaxation model, we expect the EO response to improve at low temperatures, because most charge carriers should freeze out and become bound to defect sites, creating a corresponding increase in resistivity and preventing dielectric relaxation from occurring on the measured timescales. Figure 4.3a shows that we do observe the expected improvement after cooling down our devices to 0.05 K in a dilution refrigerator with active fiber alignment. Figure 4.3b shows the results of a temperature sweep, illustrating that both the low-frequency

response and frequency flatness are improved, although even at the lowest temperatures we observe a transition in EO response amplitude near 3 Hz.

The inset of Fig. 4.3b shows the temperature dependence of the enhancement feature frequency f_e . A fit to an Arrhenius model yields an activation energy of $E_a=0.48$ eV for the enhancement frequency. This activation energy is comparable to the value of 0.4 to 0.5 eV that is typically measured for the activation of conductivity in amorphous LN, which is typically attributed to the transport of lithium ions [149].

The improvement in low-frequency EO response at low temperatures is beneficial for the operation of cavity EO transducers. However, we show in Fig. 4.3c that at low temperature the EO response depends on the optical power in the device, and low-frequency EO response is suppressed at moderate optical power levels. We measured the optical-power dependence of the EO response at room temperature and did not see any significant changes up to 0 dBm on-chip power. This optical-power dependence is likely due to the strong photoconductivity of thin-film lithium niobate, whereby the optical field excites mobile free carriers [129, 130]. While this effect could also be due to optical heating, we find this unlikely because the cryostat remains at a low temperature during these experiments ($T < 1$ K), and comparison with Fig. 4.3b suggests that local temperatures of $T\sim 100$ K would be required to reach the 0.1 Hz cutoff frequency observed for -1 dBm on-chip pump power.

Indeed, in other measurements shown in Fig. 4.3d, we see evidence for photorefractive effects, which implies strong photoconductivity in our devices. Figure 4.3d shows optical transmission spectra of our unbalanced MZM devices at roughly 0.1 K. Immediately after cooldown, the transmission spectrum (blue) appears as expected, except for a small dip near 1619 nm where the laser was used to monitor optical coupling during cooldown. After parking the laser near 1616 nm (dashed orange line) for 17 hours with an on-chip optical power of -11 dBm, the optical transmission spectrum changes dramatically, showing a window of reduced transmission roughly 10 nm wide imposed onto the usual MZM spectrum. After removing the parked laser, we observe that the transmission spectrum remains stable for at least several hours. These changes in the transmission spectrum can be reversed by warming the device up to

$T > 200$ K or by repeatedly scanning the laser at high power over a wide wavelength range. We attribute these findings to the creation of photorefractive Bragg gratings within the waveguide, which has previously been observed in ring resonators [150]. A full explanation of this effect can be found in Ref. [150], but in short weak optical standing wave patterns (generated, for example by reflection at the grating couplers) can create a photorefractive index grating which in turn enhances the standing wave pattern amplitude. This feedback effect can lead to relatively strong Bragg back reflection. This effect creates some challenges for using TFLN devices at cryogenic temperatures, but the ability to create in-situ photorefractive index changes in non-resonant devices as demonstrated here could also be a useful tool for trimming devices as well. Furthermore, previously demonstrated techniques for reducing the photorefractive effect in TFLN could be used to avoid this challenge [151]. Note that while performing all measurements at low temperatures, we were careful to avoid this photorefractive index grating effect by not leaving the laser at one wavelength for long enough to generate changes in the optical transmission spectrum. Optical transmission spectra were checked before and after each measurement to ensure that this effect did not impact the measurement.

4.4 Electrode interface variation

While we have demonstrated some degree of improved low-frequency EO response for modulators operated at cryogenic temperatures, we are also interested in improved frequency response at room temperature. Based on the dielectric relaxation model above, we posit that low-frequency EO performance could be restored at room temperature by removing the oxide layer and making good electrical contact directly to lithium niobate, which would prevent dielectric screening from occurring by eliminating Maxwell-Wagner polarization at the LN-oxide interface. To test this theory, we use reactive ion etching to create windows in the cladding silicon dioxide of our modulators to expose lithium niobate before depositing metal electrodes, as shown in Fig. 4.4a. To understand the influence of LN surface preparation on the low-frequency EO response, we characterize devices subject to two different types of

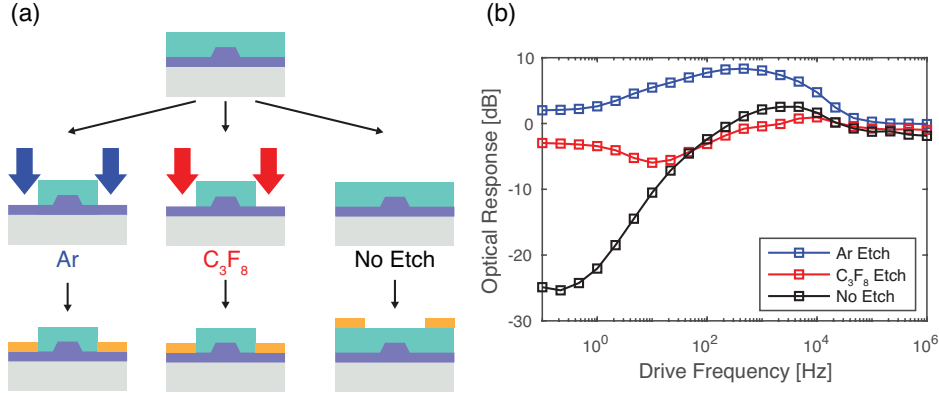


Figure 4.4: Low frequency response for etched-cladding devices. (a) An illustration of the different cladding-etch procedures for the measured devices. We test three different etch conditions: Argon terminated, C₃F₈ terminated, and no etch. (b) The frequency dependence of the EO response. While all devices exhibit similar response at high frequency (1MHz), the response amplitude in the intermediate frequency (1Hz to 100kHz) and low frequency (sub-1Hz) ranges differs significantly between the three devices. Note that here we normalize the EO response to the V_{π} of each device measured at 200 kHz to accurately compare devices with different electrode geometry.

etching plasma (Ar and C₃F₈ based plasmas) and also compare them to the fully cladded approach discussed previously.

Figure 4.4b shows the measured EO frequency response of the three electrode-interface conditions, each on a different chip. At MHz drive frequency, each device has roughly equivalent response, even across process variations. The intermediate frequency regime (1Hz to 100kHz) shows varied behavior between etch conditions. For example, the argon etched device shows a broad enhancement of the EO response, with a peak response at 500Hz a full 6dB greater than the MHz response. The C₃F₈ pre-condition shows turning points at similar frequencies. At sub-Hz frequencies, the C₃F₈-etched device has relatively good performance, but still loses a few decibels of response relative to MHz drive. The argon-etched device in this frequency range shows nearly identical response at MHz and sub-Hz frequencies. Both etched devices show marked improvement over the low-frequency performance of the fully cladded device, validating the idea that direct electrical contact between the electrodes and LN layer can improve EO response.

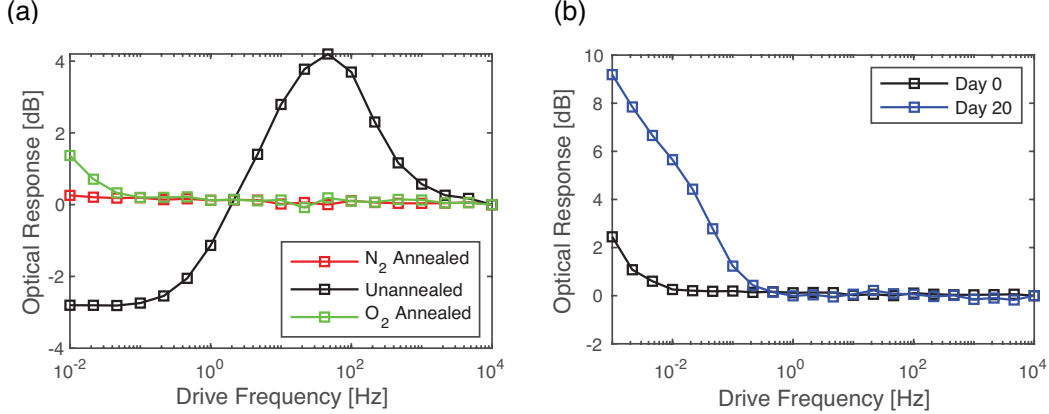


Figure 4.5: Low-frequency response of annealed devices. (a) We study the effects of annealing on electro-optic frequency response. The response of an uncladded, annealed control device is shown in black, where the extent of the mid-frequency anomalously enhanced response is clear. The response of a nitrogen-annealed device, in red, shows that the frequency response is flattened significantly to less than 0.2dB variation across the measured frequency range. An oxygen-annealed device, in green, also shows an improved response. (b) The response of an oxygen-annealed device is measured over weeks, revealing that at the lowest frequencies (sub-Hz), there is a noticeable change in the response over time.

4.5 Annealing

Another approach to improve the low-frequency performance would be to somehow reduce the conductivity of materials in the electrode region. We introduce a high-temperature annealing step into the baseline fabrication process in an attempt to reduce the density of bulk and surface defects and reduce conductivity. Annealing in oxidizing and reducing environments is commonly used in bulk LN to control types and density of intrinsic defects [141, 152–155]. To ensure exposure of the lithium niobate to gas during the anneal, we omit the cladding oxide altogether. We fabricate a set of identical chips, up to the etching of the optical waveguides (figure 4.1c(ii)), then introduce chips to an annealing process under either oxygen or nitrogen gas flow for 1hr at 500°C in a tube furnace, and deposit electrodes on each. This annealing procedure is similar to that utilized in Ref. [151], where annealing in nitrogen gas was demonstrated to reduce the magnitude of the photorefractive effect in TFLN optical ring resonators.

Figure 4.5a compares the frequency response of the annealed and unannealed devices in the intermediate frequency regime (0.1Hz to 10kHz). The unannealed device displays poor frequency flatness with an enhancement feature at a similar frequency to that observed in the

fully cladded devices. Both the annealed devices, in contrast, have excellent frequency flatness within the measured frequency range ($< 0.2\text{dB}$ variation above 1 Hz). At the lowest measured frequencies, we observe a small enhancement in the EO response of the oxygen annealed device. We find that oxygen annealed devices display an aging response. Figure 4.5b shows the EO response of the same oxygen annealed device remeasured after being stored in ambient conditions for 20 days. We observe substantial EO response amplitude enhancement at the low end of the measured frequency range.

4.6 Discussion and Conclusion

4.6.1 Origins of the change in EO response at low frequencies

Further work is required to confidently identify the microscopic origins of the EO response anomalies we observe. However, based on the results described above, we attribute the reduction in EO response at low frequencies observed in cladded devices to a thin conductive surface layer on top of the etched LN slab, as described in Section 4.2 above. In this section, we outline the evidence for surface conduction as the origin of the EO response anomalies.

Besides the LN bulk and surface conduction models described earlier, the dielectric properties of the cladding or substrate could also explain the measured response. However, the observation of EO response anomalies even in the etched-cladding and uncladded devices in Figs. 4.4 and 4.5 suggests the top cladding does not play a critical role. The buried cladding is a high-quality thermal silicon dioxide layer which we expect to behave as a near-ideal dielectric within the measured frequency range. The substrate is separated from the waveguide by the $4.7\ \mu\text{m}$ buried cladding, and simulations suggest dielectric relaxation in the substrate has a negligible impact on the measured EO response. Based on these considerations, we attribute the measured EO anomalies to properties of the LN bulk or surface.

The dependence of the measured EO response on the etch chemistry used in Section 4.4 suggests the importance of the LN surface layer to the EO response. However, this alone is not conclusive because even in the bulk conduction model, the electrical interface between the

electrodes and LN bulk could influence the measured EO response.

As described in Section 4.2, both the surface and bulk conduction models qualitatively reproduce the reduction in EO response at low frequencies, but only the surface model can explain the observed enhancement of EO response near f_e . To assess the validity of these two models, we can also compare the conductivities estimated from the numerical models with previously reported measurements on comparable materials.

The estimated conductivity of the PECVD oxide cladding ($\sigma_c \sim 2 * 10^{-10}$ S/m and $\sigma_c \sim 4 * 10^{-10}$ S/m for the bulk and surface models, respectively) is comparable to that previously measured in low-temperature PECVD oxide cladding [156].

The estimated LN conductivity of $\sigma_{LN} \sim 6 * 10^{-6}$ S/m in the bulk model is comparable to the resistivity that has been observed in bulk LN wafers that have been annealed in vacuum or hydrogen gas to chemically reduce the LN [153, 154]. Conduction in reduced lithium niobate is attributed to a system of bound and free polarons in LN [155]. These polarons have wide optical absorption bands that create the black color of reduced lithium niobate [152] and can be removed by annealing LN in oxygen, which can reverse the optical absorption created by reduction. The fact that annealing TFLN devices in oxygen and vacuum have been observed to lower and raise the optical attenuation, respectively [157], suggests that polarons may play a role in thin-film lithium niobate devices. However, previous results suggest that the conductivity estimated in the bulk conductivity model is only possible for LN with a high density of polarons that would display substantial optical absorption at the wavelengths used in this study. For example, bulk LN wafers annealed in a 10% hydrogen gas environment at 692 °C had a DC conductivity of $\sigma = 2.1 * 10^{-7}$ S/m, roughly comparable to that measured here [153]. However, a similar wafer annealed under 5% hydrogen gas at 590 °C displayed optical absorption of 105 dB/cm near wavelengths of 1.5 μ m, substantially higher than the roughly 0.1 dB/cm waveguide attenuation observed in our devices [158]. Hence, the low optical loss in our devices is inconsistent with bulk conduction due to polarons in LN. Other conduction mechanisms in undoped crystalline LN have much lower conductivity than that predicted for our bulk conductivity model [159].

The estimated surface conductivity of $\kappa_s \sim 10^{-11}$ S in the surface conduction model corresponds to a bulk conductivity of $5 * 10^{-3}$ S/m for a layer with thickness $t=2$ nm. This conductivity is comparable to that observed in amorphous lithium niobate [149]. Indeed, as mentioned earlier, the activation energy $E_a=0.48$ eV for the enhancement frequency also matches with previous measurements on amorphous LN [149].

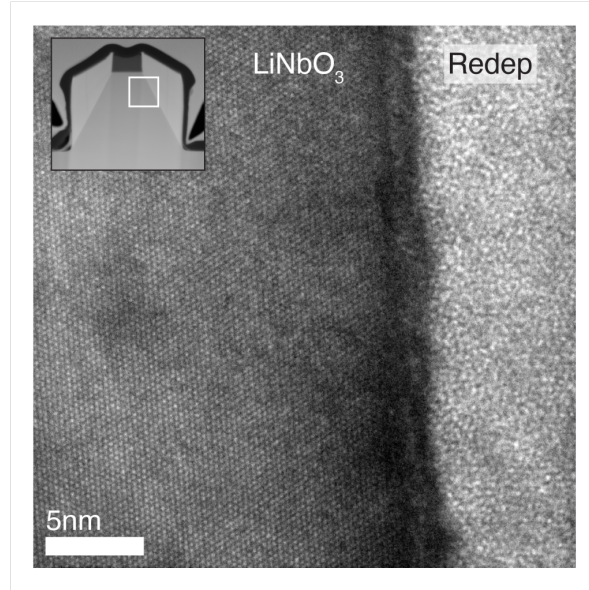


Figure 4.6: Atomically resolved transmission electron microscope (TEM) image of the LN etch interface. A cross section of an etched LN waveguide parallel to the Z-crystal axis was taken using focused ion beam milling. The figure shows a bright-field TEM image of the waveguide surface at the location indicated in the inset scanning transmission electron microscope image. The waveguide edge can be seen as a vertical demarcation between the crystalline LN region and the disordered redeposition region. Separating these two regions a dark band with a thickness of roughly 2 nm is observed that does not have a clear crystalline structure.

Figure 4.6 shows a transmission electron microscope (TEM) image of a cross section of an LN waveguide created using a similar fabrication process to the devices shown here. The TEM image is taken on a sample that was etched but not cleaned, so the amorphous redeposition region is still present on the device. We observe a dark amorphous region roughly 2 nm thick separating the redeposited material from the crystalline LN. This imaging provides some direct evidence for the possible existence of thin amorphous layers in our devices. However, imaging on a device more similar to those studied here (after cleaning and cladding) is required to determine whether the amorphous layer can be seen in our final devices.

A conductive LN surface layer – possibly composed of amorphous LN created during the LN etch process – explains many of the observations described above, including the existence and activation energy of the enhancement feature near f_e , the suppression of EO response at low frequencies, and the strong dependence of EO response on oxide plasma etch chemistry. While bulk LN conductivity can explain some of the EO response anomalies, the required conductivity has not been observed in bulk LN measurements without optical losses much higher than those observed in our devices. For these reasons, we attribute the observed low-frequency EO response effects to a conductive LN surface layer.

4.6.1.1 Future work

Nonetheless, further work is required to confirm this model. Here we estimate the material resistivities in our device by fitting EO response data to numerical simulations of the full device. The imperfect correspondence between the measured and modeled EO response and the existence of several materials and interfaces that could harbor multiple types of charge carriers makes further work important to verify the model. Direct transport or dielectric relaxation measurements on individual materials could be used to independently verify material parameters. Direct imaging of the surface layer of a complete MZM device could verify its existence, thickness, and composition.

In addition to further study of the origin of the low-frequency EO response in TFLN devices, more device interventions can be investigated to improve the low-frequency EO stability. While we find that the interventions described here can reliably produce devices with stable DC tuning over hour-long timescales, we observe significant drift and decay of the DC bias points in devices on longer timescales (i.e. multiple hours). Although measurements on such long timescales are beyond the scope of the present investigation, further improvements in EO response stability will be required to create devices capable of long-term operation. Methods to further enhance stability could include exploration of other annealing procedures, the study of the electrical interface between the metal electrodes and LN slab, and the use of conducting top cladding materials [160].

Chapter 5

Preliminary characterization of an optimized transducer

In Chapter 3 we presented an initial transducer in thin-film lithium niobate. Although the performance was modest, we described several straightforward improvements that could be made to the device to improve efficiency and power requirements. In this present chapter, we report on progress toward those improvements and characterize an improved transducer which we predict to have almost 100-fold higher transduction efficiency for a given optical pump power.

Additionally, in this chapter, we describe the use of near quantum-limited microwave amplifiers to characterize the microwave noise in our transducer created by optical absorption. We show that relatively large on-chip optical power of order 10 μW can be used while keeping the thermal occupation of the microwave mode low (< 1 photon).

These results suggest that with further improvements, a device like the one shown here may be useful for the remote entanglement generation scheme presented in Chapter 6.

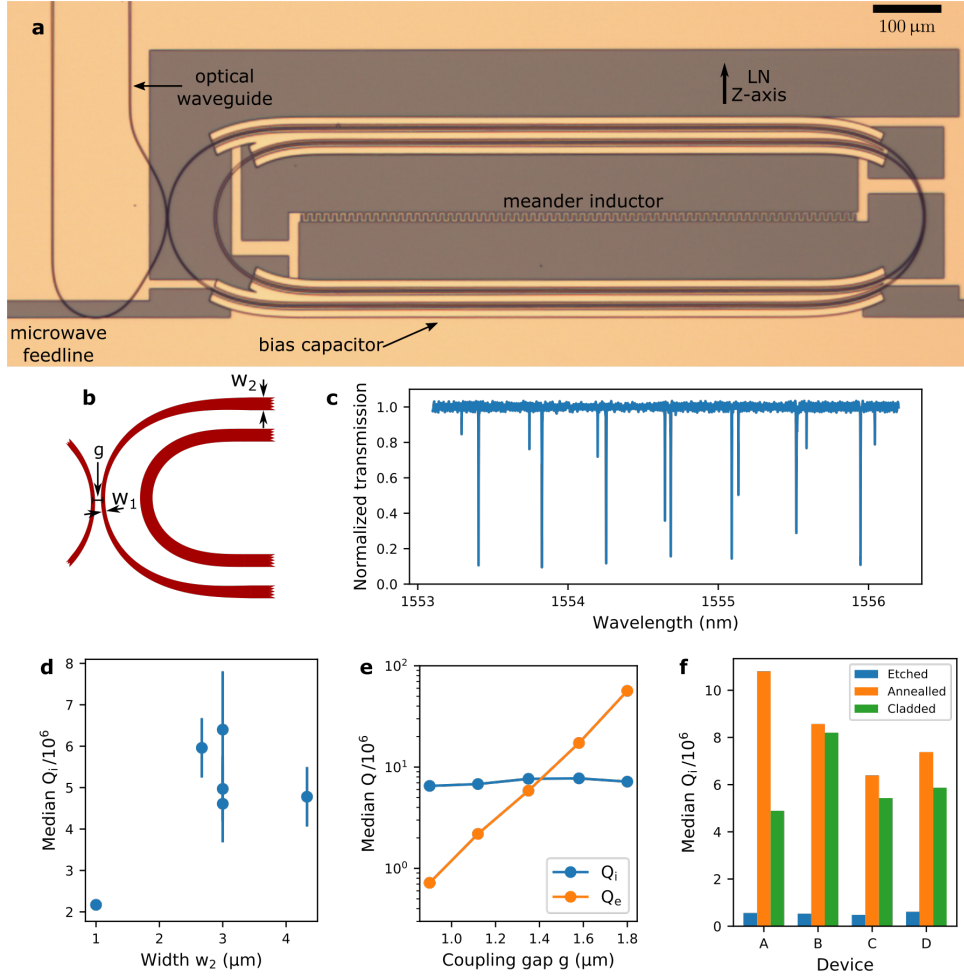


Figure 5.1: Design of coupled adiabatic racetrack resonators. (a) Optical microscope image of the optimized device, showing Nb thin-film (tan color) and optical waveguides (black). The bright (i.e. coupled to a bus waveguide) optical resonator is evanescently coupled to a bus waveguide on the left. (b) Schematic of the coupling region of the adiabatic racetrack resonators. The racetrack resonators taper adiabatically from a narrow width w_1 in the curved coupling regions to a wide width w_2 in the straight regions. The bus waveguide is symmetric to the resonator in the coupling region and the two are separated by a gap g . In our devices, $w_1=1 \mu\text{m}$, $w_2=3 \mu\text{m}$, and $g=0.85 - 1.3 \mu\text{m}$. (c) Optical transmission spectrum, showing several coupled optical modes. (d) Dependence of the median intrinsic quality factor of optical modes measured in a 10 nm band near $\lambda=1580 \text{ nm}$ on the width w_2 of the resonator. (e) The effect of the coupling gap g on the intrinsic and extrinsic quality factors of a single-ring device. (f) Intrinsic optical quality factors measured at several stages in the fabrication process, including immediately after etching the LN waveguide, after annealing, and after cladding the device with PECVD silicon oxide and a second annealing step.

5.1 Transducer optimization

Figure 5.1a shows an image of the optimized device. The two optical racetrack resonators are inset to minimize the device area and reduce parasitic capacitance for the microwave resonator. As described in Chapter 3, decreasing the optical loss rate is one of the most effective ways to improve device performance, and previous work has shown that increasing the width of the optical waveguides is a straightforward approach to accomplish this [105]. However, this approach comes with several challenges. Because of the weak evanescent coupling in wide waveguides, this approach would require long coupling lengths between the resonators and between the bright resonator and the bus waveguide. Such long coupling lengths would make it more challenging to realize a high electrode coverage fraction α . Furthermore, waveguides wider than those used in Chapter 3 host multiple transverse optical modes, which can hybridize with the desired fundamental modes and act as parasitic loss mechanisms. Finally, efficiently coupling to multimode waveguides without excess loss is non-trivial due to coupling between transverse modes induced by the bus waveguide, an effect termed coupling ideality [161].

We avoid these challenges in our racetrack resonators by adiabatically tapering the waveguide width below the single-mode criterion in the coupling region, as shown in Fig. 5.1b, similar to recent work in other photonics platforms [162]. This ensures strong and ideal evanescent coupling and that only the fundamental modes are guided along the entire length of the resonator. Figure 5.1c shows that only TE fundamental optical modes are visible in the optical spectrum because the TM mode coupling is suppressed by the symmetric design of the coupling region and higher-order modes are unguided in the resonator. By tapering to a wide, multimode waveguide in the straight sections, high optical quality factors can still be achieved. Figure 5.1d shows that keeping a constant width $w_1=w_2=1\ \mu\text{m}$ leads to a suppressed optical quality factors $Q_i \sim 2 * 10^6$, but tapering the waveguide wider so that $w_2 \gtrsim 2.5\ \mu\text{m}$ results in improved quality factors $Q_i \sim 4 * 10^6$. By sweeping the coupling gap in Fig. 5.1e we observe that the intrinsic optical quality factor is not suppressed by strong extrinsic coupling, indicating our devices have high coupling ideality [161].

To further improve the optical quality factor we anneal our devices in an oxygen-flow furnace for 2 hours (2 hour ramp time) at 550°C after etching and cladding the device, which has been shown to reduce optical absorption loss in TFLN [157]. We confirm these results in Fig. 5.1f by measuring the median intrinsic optical quality factor at several steps in our fabrication process. Immediately after etching and cleaning the LN waveguide, we measure $Q_i \sim 0.5 * 10^6$. After a first annealing step the measured intrinsic quality factor improves to $Q_i \sim 6 * 10^6$. Cladding the device and annealing it again yields comparable intrinsic quality factors. In addition, we observe that this annealing step improves the low-frequency EO response, consistent with the results described in Chapter 4. Although it is unclear why annealing improves optical quality factors [157], we hypothesize that it may be due to the elimination (via crystal oxidation) of intrinsic polaron defects [155] that have wide absorption bands or the reversal of etch-induced crystal damage.

Figure 5.2a shows the fabrication procedure and electrode geometry for the optimized device (See D.3.2 for fabrication process details). This fabrication procedure is similar to the one used in the device described in Chapter 3, with the addition of a cladding etch process that is continued through the LN slab. This electrode geometry ensures that the niobium layer has direct contact with the LN slab, which improves the low-frequency EO response as described in Chapter 4. Additionally, this electrode geometry provides a roughly 2-fold enhancement in the electric field inside the waveguide over the generation I gate design used in Chapter 3, quantified by the d_{eff} parameter shown in Fig. 5.2. This enhancement is due to the wider waveguide and the direct contact between the electrode and the LN slab. Despite the enhancement of the electric field in this design, simulations of the microwave piezoelectric loss show that relatively low loss is possible, with Q_{PZE} as high as 2000 near 6 GHz

Figure 5.3 shows measurements of the optical and microwave transmission of the device. By sweeping the bias voltage in Fig. 5.3a, we observe the optical anticrossing and measure a minimum optical splitting of $2\mu = 4.95$ GHz. We also extract the intrinsic and extrinsic coupling rates of the bright and dark modes far from the anticrossing, and find that $\{\kappa_{i,\text{bright}}, \kappa_{i,\text{dark}}, \kappa_{e,\text{bright}}, \kappa_{e,\text{dark}}\}/2\pi = \{65, 39, 79, 2.8\}$ MHz for this set of modes. Especially in the case of

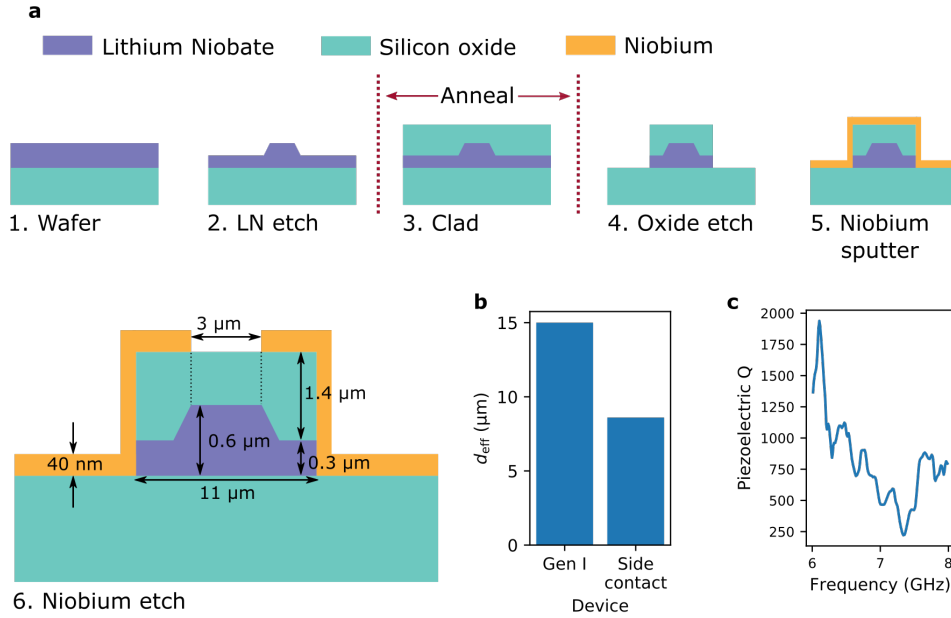


Figure 5.2: Design of a side-contact electrode geometry for the optimized transducer. (a) Device fabrication. 1-6 shows steps individual steps in the fabrication process. 6 also shows the geometry of the electrode region. 1: A commercial wafer with a 600 nm thin-film LN layer on a 4.7 μm thermal silicon oxide layer on top of a 525 μm silicon substrate. 2: LN waveguide is defined using a hydrogen silsesquioxane electron-beam mask and argon-based plasma etching. 3: Plasma-enhanced chemical vapor deposition is used to clad the LN waveguide with 1.4 μm of silicon oxide. Before and after this step we anneal the device as described earlier. 4: We etch through the cladding and slab layers using C₄F₈-based reactive ion etching and argon-based plasma etching. 5: A niobium thin film is conformally deposited using sputtering. 6: The niobium film is etched to define the microwave resonator using CF₄-based reactive ion etching. (b) Simulated effective capacitor gap d_{eff} for the generation I device described in Chapter 3 and the side-contact geometry shown here. (c) Simulated microwave quality factor due to piezoelectric loss using this get design.

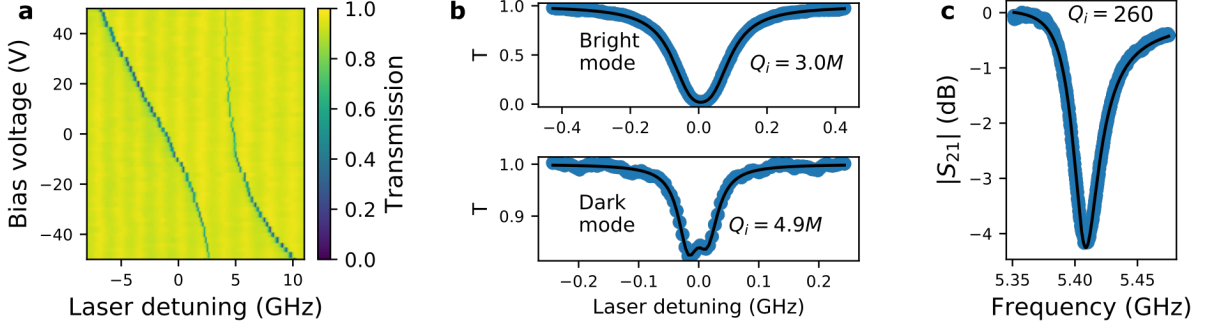


Figure 5.3: Characterization of optical and microwave resonators. (a) Optical transmission spectra near $\lambda=1565$ nm for different DC bias voltage settings, showing a minimum optical splitting of $2\mu = 4.95$ GHz. (b) Optical transmission near a bright (top) and far-detuned dark (bottom) optical mode near 1565 nm. (c) Microwave transmission spectrum taken at $T = 50$ mK showing the microwave resonance at 5.41 GHz. To remove background transmission fluctuations caused by impedance mismatch along the transmission line, here we plot the difference between the transmission with a strong laser excitation (about $30\mu\text{W}$ off-chip, where the microwave resonance is nearly completely extinguished due to quasiparticle generation) and the transmission without laser excitation.

the far-detuned and weakly coupled dark mode, we observe a clear splitting of the Lorentzian resonance lineshape, which is evidence of hybridization between the clockwise (CW) and counterclockwise (CCW) traveling wave modes of the ring resonator. Previous work has shown that this coupling can be treated analytically by a complex CW/CCW coupling rate κ_c with real and imaginary components that account for the direct and dissipatively-mediated coupling between the modes [163]. For the dark mode shown in Fig. 5.3b, this coupling rate is $\kappa_c/2\pi=(33 + 1.9i)$ MHz. The hybrid optical modes of our devices typically fall into the weak coupling limit where $\kappa_c \ll \kappa$. In this regime, only one near-Lorentzian resonance is observed, corresponding to an optical mode primarily propagating as a traveling wave mode in one direction, and the coupling can be treated as an additional loss mechanism, whereby

$$\kappa_i \approx \kappa'_i + \frac{\kappa_c^2}{\kappa}, \quad (5.1)$$

where κ'_i represents the intrinsic losses, not including coupling to the other propagation direction. For simplicity, here we report only κ'_i but include the effects of the directional coupling in models of the transduction efficiency.

Figure 5.3c shows the microwave transmission near the microwave resonance frequency

of 5.41 GHz. By fitting this microwave transmission spectrum, we infer loss rates of $\{\kappa_{m,i}, \kappa_{m,e}\}/2\pi = \{21, 13\}$ MHz.

5.2 Bias response under optical pumping

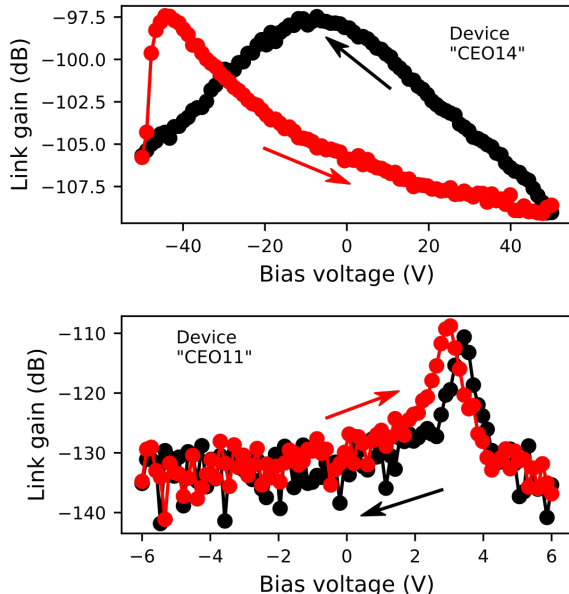


Figure 5.4: Comparison of the photonic link gain during bias voltage sweep of two different devices. The link gain is the measured gain between a microwave input signal into the dilution refrigerator and the microwave output signal measured after the modulated light output by the transducer is measured in a photoreceiver. This link gain is measured during a triangular bias voltage sweep, similar to the measurement described in Fig. 3.3b. Red and black curves show the measured link gain when sweeping voltage up and down in time, respectively. The top plot shows the results for the same device shown in Fig. 5.3 with an on-chip optical pump power of -18.8 dBm. The bottom plot shows the results for a nominally identical device with on-chip optical pump power of -15.2 dBm. Both measurements are performed with pump wavelength near 1570 nm.

Preliminary measurements of transduction efficiency during a bias voltage sweep are shown in Fig. 5.4. For the device labeled "CEO14" (the same device characterized in Fig. 5.3 above), the impact of the charge carrier effects described in Chapter 4 is significant. Even for the relatively large voltage sweep range of ± 50 V, we can barely tune through the optical resonance, and we observe significant hysteresis indicating that control over the optical mode splitting is limited. The origin of this limited control is not yet well understood, but the poor low-frequency EO response would make it challenging to use this device for the pair generation

experiments proposed in Chapter 6.

Another device labeled "CEO11" (Fig. 5.3, bottom) with a nearly identical fabrication procedure except for a modified cladding deposition procedure shows substantially improved response to the bias voltage - note the difference in bias voltage ran in the two plots. Unfortunately, this device has degraded optical quality factors ($Q_i \sim 2 * 10^6$) compared to our best devices, which we attribute to a low-quality cladding oxide recipe (See Appendix D.3.2 for details). The different cladding procedures could play a role in the differences observed in EO response between CEO11 and CEO14, but further work is required to study the reliability of the EO response across different devices. We note also that we observe an aging effect on the optical quality factors of device CEO14. During fabrication, we measured median intrinsic quality factors of $Q_i = 6.5 * 10^6$ and $6 * 10^6$ for bright and dark modes respectively. After several months of storage in ambient conditions, we measured reduced median quality factors of $Q_i = 2.9 * 10^6$ and $4.5 * 10^6$ for bright and dark modes. This may be related to the EO response aging effect observed in Fig. 4.5. Further work is required to determine the repeatability, dynamics, and causes of these aging effects.

In future work, we plan to perform calibrated transduction measurements like those shown in Fig. 5.4 to infer the g_0 parameter of the improved devices described here. That measurement will enable us to accurately gauge the feasibility of the measurements proposed in Chapter 6.

5.3 Characterization of thermal microwave noise

Added noise during transduction is a key metric for a quantum transducer. While the EO transduction scheme in principle can be performed with only quantum-limited noise, in practice other sources of noise can occur. The high carrier frequency and ability to filter the pump laser light means that the optical fields add negligible direct noise. However, absorption of the pump field in the optical waveguides, device packaging, and microwave resonator can create thermal baths with temperatures that exceed the base temperature of the dilution refriger-

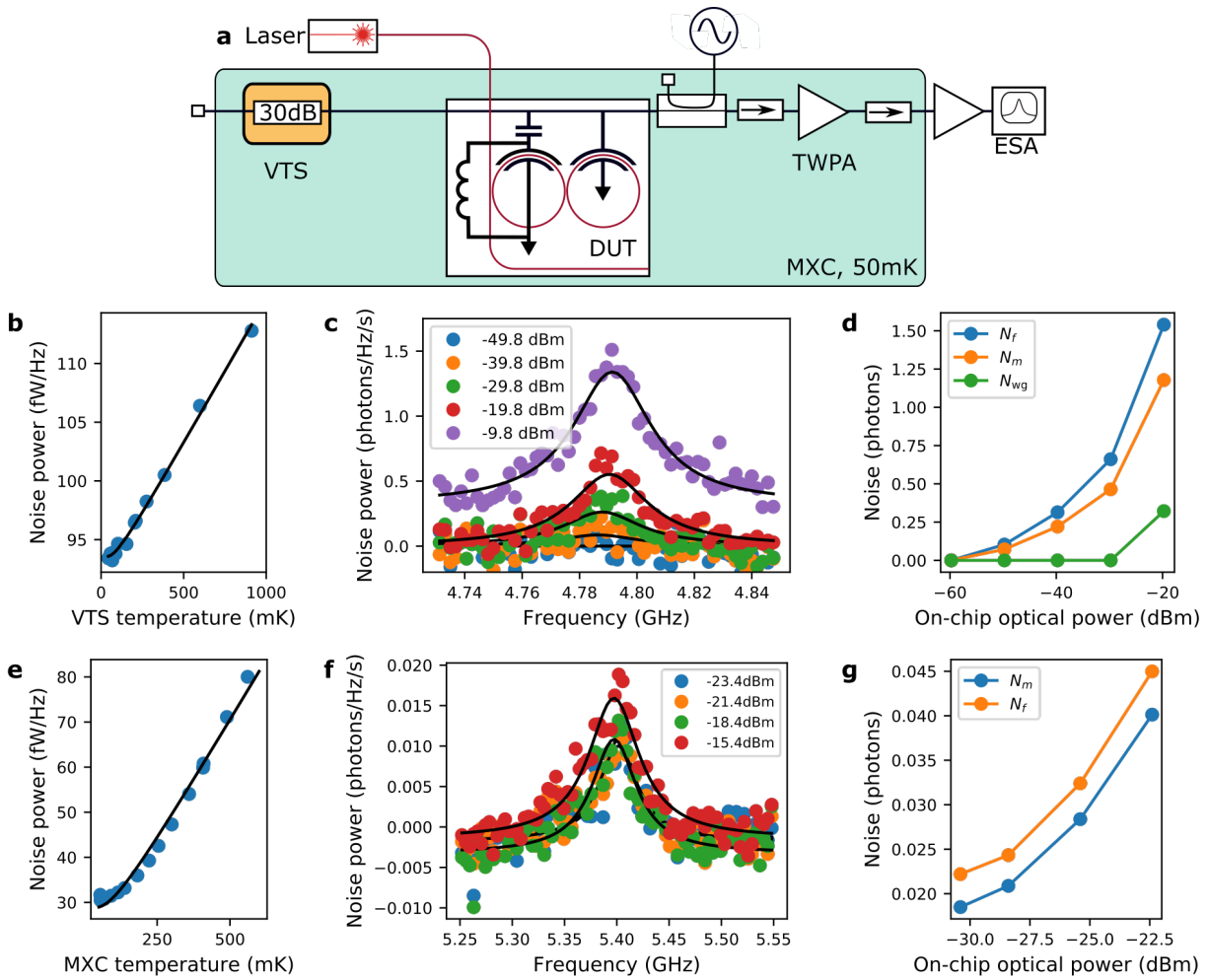


Figure 5.5: Measurement of thermal microwave noise. (a) Measurement setup to detect thermal noise from the microwave resonator. The device under test (DUT) is thermally anchored to the mixing chamber (MXC) plate of the dilution refrigerator cryostat, along with a traveling-wave parametric amplifier (TWPA). A variable temperature stage (VTS) is weakly thermally anchored to the MXC. The VTS temperature can be controlled using an onboard heater and temperature sensor to create a calibrated source of thermal radiation. A laser is used to send light into the DUT. The signal from the measurement chain is further amplified by gain stages at $T = 4$ K and room temperature and measured on an electrical spectrum analyzer (ESA). A microwave signal generator is used to create a pump field for the TWPA through a reflection coupler (20dB). Small white squares show 50Ω terminations and arrows denote microwave isolators. (b-d) show characterization of the Gen I device described in Chapter 3. (b) By sweeping the VTS temperature we generate a known noise power into our device, which we use to calibrate the amplifier chain. (c) Microwave noise spectra near the microwave resonance frequency for different on-chip optical powers. (d) Estimated thermal occupation of the output microwave field (N_m), the intrinsic loss bath of the microwave resonator N_f , and the extrinsic loss bath of the microwave resonator (N_{wg}) inferred from the measured noise spectra. (e-g) show similar measurements on the device presented in this chapter, with the exception that the calibration in (e) is performed by sweeping the MXC temperature.

erator, which can lead to excess thermal occupation of microwave mode. Previous work on similar devices with thin-film superconducting resonators [86, 164] has shown that the dominant source of noise is optical absorption in the superconductor, which generates a high-temperature quasiparticle bath that acts as a source of loss and noise in the microwave resonator. For quantum-regime transduction, the occupation of the microwave mode N_m should be small, i.e. $N_m \ll 1$. Broadband noise due to optical heating of the device, packaging, and coaxial lines is also observed in previous work [86], and can be modeled as a microwave waveguide thermal bath with occupancy N_{wg} .

In this section, we use a low-noise microwave amplifier chain to directly measure the thermal noise produced by our device under optical illumination with high SNR. Figure 5.5a shows the measurement setup we used to perform these measurements. We use a chain of low-noise amplifiers starting with a traveling wave parametric amplifier (TWPA) [165] to amplify the weak few-photon noise signals produced by our device and measure the noise spectrum on an electrical spectrum analyzer (ESA). To calibrate the ESA signal in units of noise quanta, we can control the temperature of a 30 dB attenuator on a variable temperature stage (VTS) that acts as a near-blackbody source of thermal noise. Weak thermal contact between the VTS and the mixing chamber plate (MXC) ensures that the VTS temperature can be controlled without heating the other devices, including the TWPA, connected to the MXC. The measured noise power P_{ESA} as a function of the VTS temperature T_{VTS} is

$$\frac{P_{\text{ESA}}(\omega)}{B} = G\hbar\omega \left(\frac{1}{2} \coth \left(\frac{\hbar\omega}{2k_b T_{\text{VTS}}} \right) + N_{\text{add}} + \frac{1}{2} \right), \quad (5.2)$$

where B is the measurement bandwidth, G is the amplifier chain gain referred to the output of the VTS attenuator, and N_{add} is the excess noise added by the amplifier chain. Figure 5.5b shows the dependence of the measured noise power on the VTS temperature. Fitting these data to Eq. 5.2 allows us to extract the gain $G = 92.5 \pm 0.08$ dB and added noise $N_{\text{add}} = 16.4 \pm 0.3$ quanta. Using this calibration, we can then convert the measured ESA signal to the thermal noise before the amplifier chain in units of photons/Hz/s using $N(\omega) = P_{\text{ESA}}(\omega)/(BG\hbar\omega) - N_{\text{add}} - 1/2$. Due to small fluctuations of the gain G over hour-long

timescales, in practice, we infer N_{Add} from a reference ESA measurement at base temperature immediately before sweeping the laser power. Note that this calibration procedure does not include the effects of loss between the output of the VTS attenuator and the microwave resonator. In future measurements, the cable loss between these devices can be independently estimated to improve the calibration accuracy, but we estimated the insertion loss to be < 1 dB, so this will not have a significant effect on the results.

The calibrated microwave noise spectrum is shown in Fig. 5.5c for a first-generation device similar to that described in Chapter 3 for different on-chip optical pump power levels¹. A noise peak with Lorentzian lineshape is observed with linewidth and frequency consistent with the transmission measurements of the microwave resonance. As the optical pump power is increased, the amplitude of the noise peak and background noise level both increase. By fitting these noise spectra to the model described in Section 2.2.4, we can infer the internal thermal bath occupancy of the intrinsic loss in the microwave resonator N_f , the microwave resonator itself N_m , and the microwave transmission line N_{wg} . These parameters are shown as a function of pump laser power in Fig. 5.5. The occupation of the microwave mode N_m is lower than the occupation of the intrinsic loss path N_f to which it is connected because the microwave resonator also has a loss channel to the comparatively cold N_{wg} bath.

Figures 5.5e-g show similar results for the improved device described in this chapter. In addition to the device enhancements described above, we also use a redesigned device packaging that provides extra optical shielding between the microwave resonator and optical coupling region (see Section D.2 for details). This improved optical packaging was motivated by the observation described in Chapter 3 that the optically-induced excess loss did not measurably change whether the laser was resonant with an optical mode of the device or not, suggesting that the dominant source of optically-induced microwave loss is the absorption of scattered light, not light in the optical resonators. Other work on aluminum nitride cavity EO transducers has produced similar results [86]. Furthermore, the niobium superconducting resonator used here should be less susceptible to quasiparticle loss because it has a kinetic inductance

¹Note here we use a different device than the one described in Chapter 3 due to the limited microwave bandwidth of the isolators used in our measurement chain.

that is roughly 10-fold smaller than that of the niobium nitride resonator used in Chapter 3. The noise measurements shown in Figs. 5.5f and g show that the measured microwave noise is roughly 10-fold lower in the improved device described here than in the first-generation device. However, due to a technical failure of the VTS, the data in Figs. 5.5f and g were calibrated using direct control of the MXC temperature. Thus these results need to be checked to compare the noise in these devices on equal footing. Nonetheless, the initial results shown here suggest the improved packaging and use of niobium superconducting film may improve the noise in our devices.

5.4 Discussion

Table 5.1 shows the measured and estimated properties of the optimized device described here, compared to the properties of the previous device shown in Chapter 3. With the improved optical and microwave resonator designs, we have demonstrated roughly 6-fold and 3-fold improvements in the loss rate of the optical mode and the EO interaction rate, respectively. However, it is important to note that the microwave linewidth is roughly 3-fold larger in the optimized device. We attribute this to a combination of relatively high piezoelectric loss at the frequency of the device described here, as well as higher dielectric loss in the silicon dioxide cladding that was optimized for reduced optical loss. This increased microwave loss means that the improvement in expected transduction efficiency is only a relatively modest factor of 20 for constant optical pump power, although the results in Fig. 5.5 suggest high optical pump powers can be used in these devices. For the pair generation and remote entanglement experiments proposed in Chapter 6, the rate of entanglement generation is independent of microwave linewidth in the high optical loss limit where $\kappa_{\text{opt}} \gg \kappa_m$. This means that the optimized device is particularly beneficial for those applications.

Table 5.1: Comparison of optimized transducer with previous design. Table shows the measured and estimated device parameters for the device described in Chapter 3 and the optimized device described here. Note that here we calculate the efficiency and cooperativity assuming resonant pumping, and that the two hybrid optical modes have identical loss parameters, leading to higher values than those measured in Chapter 3.

	Gen I device (Chapter 3)	Optimized device (Chapter 5)
$\omega_m/2\pi$	3.88 GHz	5.41 GHz
$2\mu/2\pi$	3.1 GHz	4.94 GHz
$\kappa_{\text{opt}}/2\pi$	580 MHz	90 MHz
$\kappa_m/2\pi$	11 MHz	34 MHz
$g_0/2\pi$	850 Hz	2.4 kHz
C (1 μW pump)	$2.7 * 10^{-6}$	$1.8 * 10^{-4}$
$\eta_{\text{on-chip}}$ (1 μW pump)	$5.0 * 10^{-6}$	$1.2 * 10^{-4}$

Chapter 6

Outlook: optically heralded generation of remote microwave entanglement

Across a wide variety of platforms, including the cavity electro-optic devices described in this dissertation, the microwave-optical transducers that have been demonstrated so far have not reached the capabilities required for direct transduction of quantum states [42, 73, 166]. Given the difficulty of avoiding the many loss mechanisms involved with the optical transmission of microwave states (including transduction efficiency, pump filtering, chip-to-fiber coupling, and attenuation in optical fiber networks), a direct scheme involving the transmission of quantum states between nodes appears challenging. It seems likely that instead, a realistic quantum network using microwave-optical transduction would use an optically-heralded approach, for example to create remote entanglement between nodes [93, 167]. This entanglement could then be used as a resource to perform teleportation of quantum states or gates. Alternatively, transduction schemes based on teleportation with continuous-variable entanglement have also been considered [120, 168], but these are more susceptible to hard-to-avoid optical loss.

In this chapter, we describe and estimate the performance of a simple scheme, based on the well-known proposal of Duan, Lukin, Cirac, and Zoller [11], for generating entanglement

between two remote microwave modes using an optical heralding signal. The use of optical heralding makes the fidelity of the resulting entangled state insensitive to optical loss and transducer efficiency, although these factors strongly control the rate at which entanglement can be generated [167]. We estimate the entanglement generation rates and fidelity that could be achieved for near-term cavity electro-optic transducers in thin-film lithium niobate. However, it is important to note that this scheme applies to a wide variety of quantum transduction schemes and devices [11].

This scheme is similar to recent work proposed in other quantum systems with optically active memories such as trapped ions and solid-state defects for the creation of distributed quantum networks through heralded optical photon detection [19, 30]. In particular, recent work using nitrogen-vacancy centers in diamond has demonstrated the use of optically heralded quantum networks to measure loop-hole free Bell inequalities [26], deterministic delivery of remote entanglement [169], and the creation of multi-node quantum networks [170]. While similar networks of superconducting qubits have been made using microwave channels [38, 171], the proposal described here could potentially enable large scale networks of superconducting qubits mediated by optical channels.

6.1 Heralded generation of remote microwave entanglement using cavity electro-optics

Figure 6.1 shows our proposed single-link system for optical generation of remote entanglement between superconducting qubits. Two transducers in separate nodes are pumped on the blue sideband in the weak-transduction regime to generate correlated microwave-optical photon pairs. The pump pulse generates entangled microwave-optical states in each node. In the weak pumping regime, these states can be approximated as

$$|\psi\rangle_{A,B} \sim |0_m 0_o\rangle_{A,B} + \sqrt{p} |1_m 1_o\rangle_{A,B}, \quad (6.1)$$

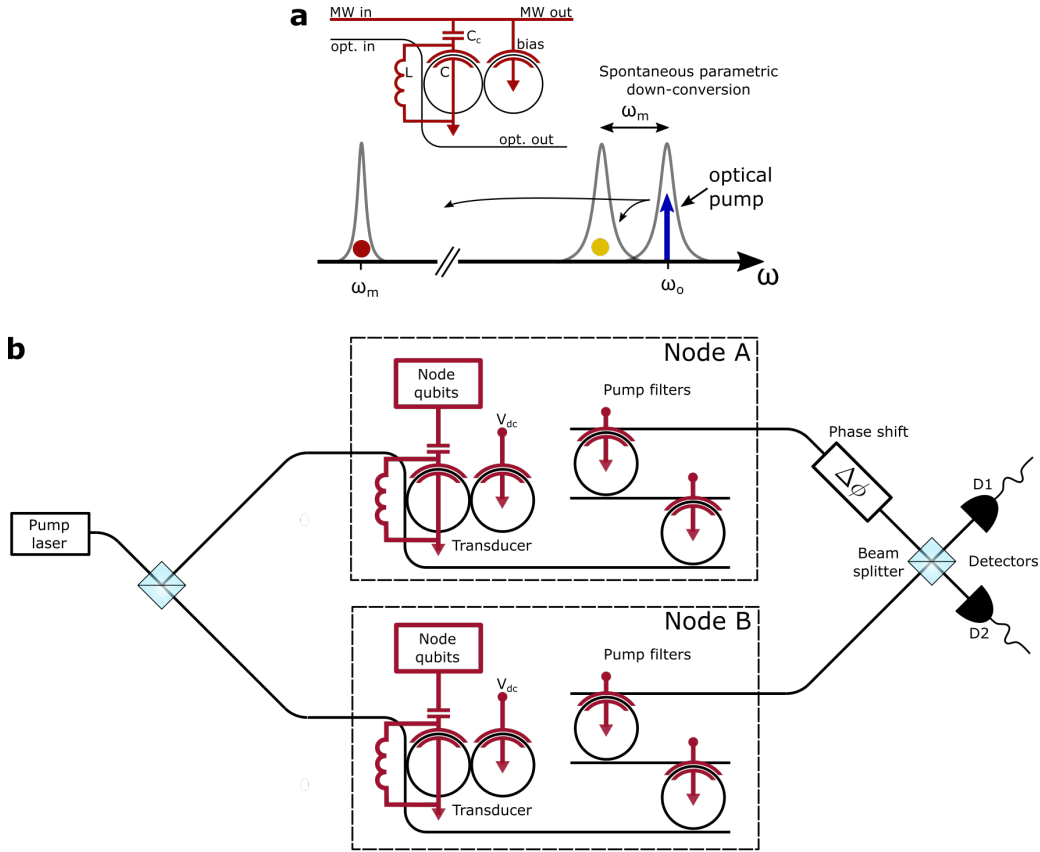


Figure 6.1: Remote entanglement of superconducting qubits using an optical channel. (a) Spontaneous parametric downconversion in an electro-optic transducer. Top: schematic of a photonic molecule cavity electro-optic microwave-optical transducer. Two evanescently coupled ring resonators form photonic molecule hybrid modes that can be frequency tuned by a bias capacitor. A lumped element LC resonator modulates the photonic molecule modes through the electro-optic effect. Bottom: Frequency-domain illustration of spontaneous parametric downconversion. An optical pump pulse tuned to the high-frequency optical resonator can generate correlated pairs of photons in the low-frequency optical resonator and microwave resonator by spontaneous downconversion. (b) Schematic diagram of the proposed system for optical generation of remote entanglement between superconducting qubits. A pump laser tuned to the blue optical mode can induce SPDC to create correlated microwave and optical photon pairs in two transducers in two remote nodes. On-chip pump filtering can be used to extinguish the optical pump with minimal loss of the down-converted optical signal photons. Combining the output optical channels of both nodes on a beamsplitter erases which-path information so that detection of a signal photon generates an entangled microwave bell state across the two nodes. The entangled microwave state can be transferred to superconducting qubits in each node for further distillation or processing.

where p is the pair generation probability, subscripts $\{m, o\}$ denote the microwave and optical resonators respectively, and subscripts $\{A, B\}$ denote the node. Assuming the loss rate of the transducer's microwave resonator is much smaller than that of the optical resonators, the

internal pair generation probability is given by $p = \frac{4g_0^2}{\kappa_o^2} N$, where g_0 is the electro-optic interaction rate, κ_o is the optical mode loss rate, and N is the number of photons in the pump pulse. Passing the optical outputs of the two nodes through a beam splitter erases which-path information and ensures, in the weak-pumping regime where $p \ll 1$, that detection of a signal optical photon at detector $D_{1,2}$ heralds the creation of the entangled bell state

$$|\Psi^\pm\rangle = \frac{1}{\sqrt{2}} \left(|0_m\rangle_A |1_m\rangle_B \pm e^{i\Delta\phi} |1_m\rangle_A |0_m\rangle_B \right). \quad (6.2)$$

The microwave state in the transducer resonator can then be collected in a superconducting qubit network located within each node through a transmission line, for example using stimulated two-photon Raman absorption [172]. After collection, the entanglement resource could be used by a quantum processor.

This scheme relies on the indistinguishability of signal optical photons arriving from the two transducers and the complete extinction of pump photons by a filter. The integrated electro-optic transducers described in this dissertation are particularly promising for this application because they support tunable optical modes and can be easily integrated with high-efficiency pump filters [124].

6.1.1 Entanglement generation rate

The entanglement generation rate R_{ent} is a key metric for the design, as entanglement distillation requires that this rate exceed the decoherence timescale of the node's quantum processor. For our architecture, the entanglement generation rate is $R_{\text{ent}} = \eta_{\text{opt}} p R$, where η_{opt} is the total detection efficiency of optical signal photons including all coupling and filtering losses, and R the entanglement attempt repetition rate.

The repetition rate is limited by the time required to reset the microwave resonator between entanglement attempts so that $R < \frac{\kappa_m}{10} \sim 1$ MHz, where κ_m is the microwave loss rate. The relatively fast decay time of the microwave resonator and correspondingly high maximum repetition rate is one of the benefits of an electro-optic approach – unlike other transduction

Table 6.1: Estimated remote entanglement performance for demonstrated (Gen I) and future (Gen II) electro-optic transducers. The Gen I device assumes demonstrated transducer parameters, and an estimated -28 dB detection efficiency from -10 dB fiber-chip coupling loss, -15 dB insertion loss from commercial fabry-perot filters, and -3 dB additional loss, including detector efficiency, fiber loss, etc. The Gen II devices assumes reasonable improvements in transducer parameters, some of which were described in Chapter 5, a reduction in chip-fiber coupling loss to -3 dB, and on-chip filtering with negligible insertion loss.

	Optical Q_i	g_0 (kHz)	R (MHz)	η_{opt} (dB)	Avg. pump (uW)	R_{ent} (kHz)
Gen I	10^6	0.5	1	-28	2.5	10^{-5}
Gen II	10^7	1.5	1	-6	2.5	7.5

approaches such as optomechanics, a direct electro-optic transducer does not require narrow-bandwidth intermediate states.

Pump power is also a key metric for our design for two reasons. First, intense optical pump powers can directly generate thermal microwave noise in the transducer through quasiparticle generation by optical absorption, leading to reduced entanglement fidelity, as described below. Second, high pump power requirements can overwhelm the cooling power of the cryostat, interfering with the operation of the quantum processor. As such it is critical to use a photonic platform with high nonlinearity and low optical loss, such as lithium niobate, to ensure a large pair generation probability p with relatively low pump power. This would enable the low-temperature operation of these devices even if multiple transducers are used in parallel.

Table 6.1 shows the predicted entanglement rate for our devices. Achieving high entanglement rates > 1 kHz requires modest improvements over previously demonstrated electro-optic transducers in lithium niobate [90, 92, 93]. The electro-optic interaction rate can be improved with relatively minor changes to the electrode geometry. The optical quality factor can be improved by more than 10-fold by using wider waveguides with weaker sidewall scattering, as demonstrated in Ref. [105].

The entanglement rate can also be enhanced using on-chip pump filters, which can have insertion loss much lower than off-chip filters [124, 173]. Filters sufficient for our application have not yet been demonstrated in thin-film lithium niobate, but the low loss of ring resonators in this platform makes high-extinction and low-loss filtering relatively straightforward. Figure 6.2 shows one possible filter design with $N_{filter} = 5$ tunable ring add/drop filters. The re-

quired -95 dB extinction can be achieved over a stop bandwidth of $SBW = 200$ MHz, with just -0.5 dB of insertion loss at a signal frequency 7 GHz from the pump frequency. The independent electro-optic tunability of the individual resonators ensures that small fabrication-induced variations in the resonant frequencies can be tuned away without additional heat load to the cryostat. While challenges with optical cross talk may limit the achievable extinction, cross talk of less than 80 dB has been demonstrated [173], and a small amount of off-chip filtering (with relatively low insertion loss) can be used to compensate for this crosstalk.

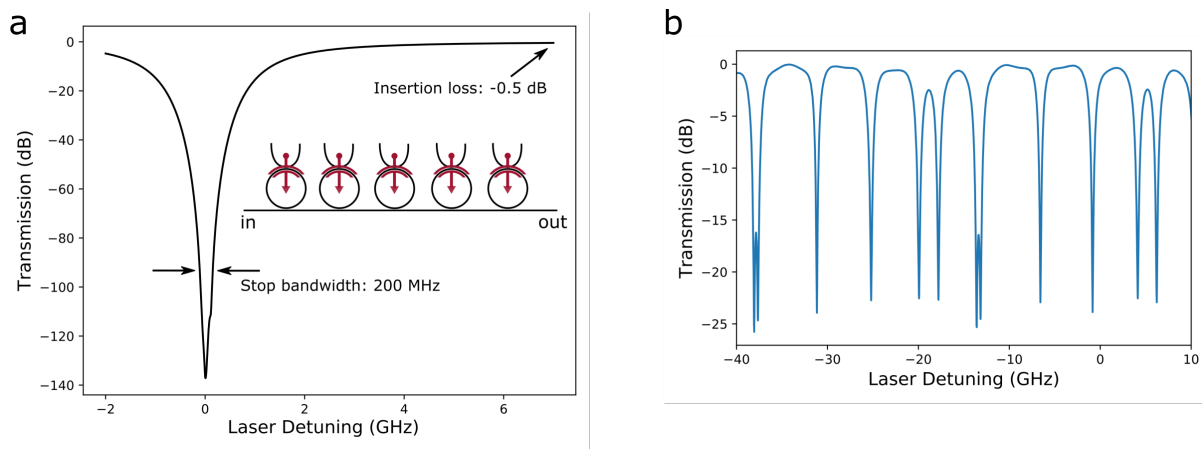


Figure 6.2: Performance of an on-chip integrated filter array based on tunable add/drop ring resonators. (a) The simulated transmission assumes intrinsic loss rates of each resonators of $\kappa_i/2\pi = 70$ kHz, and extrinsic coupling to both waveguides of $\kappa_e/2\pi = 1$ GHz with a standard deviation $\Delta\kappa_e/2\pi = 0.1$ GHz to include typical fabrication uncertainties. Resonance frequencies are also assumed to have standard deviation $\Delta f_0 = 50$ MHz to include the effects of imperfect voltage tuning. Inset: schematic of the filter array, showing the tuning capacitors (red) and optical waveguides (black). (b) Measured normalized transmission of a fabricated filter array with N_{filter} near 1580 nm before tuning filters to degeneracy. Each filter stage produces more than 20 dB of pump extinction. The FSR of the filters is roughly 36 GHz.

6.1.2 Entanglement fidelity

The fidelity of generated entanglement is another key metric, as a higher raw link fidelity reduces overhead in the superconducting quantum processor required for distillation. Our proposed entanglement link is susceptible to several sources of noise, including multi-pair generation which occurs with probability p conditional on the creation of at least one pair, the average thermal microwave occupancy P_m , microwave loss P_{loss} between the transducer and

superconducting quantum processor, false heralding with probability P_{false} due to dark counts or leaked pump light in the optical detectors, and phase errors with probability P_{phase} due to drift in the interferometer between the nodes. In the high-fidelity regime where all error probabilities are small, these error mechanisms can be considered independently and the resulting raw link fidelity is

$$F = |\langle \Psi_{\text{ideal}}^{\pm} | \Psi_{\text{real}}^{\pm} \rangle|^2 = 1 - p - 2P_m - \frac{3}{2}P_{\text{loss}} - P_{\text{false}} - P_{\text{phase}}. \quad (6.3)$$

These error mechanisms can be minimized using several approaches.

The multi-pair generation can be reduced by lowering pump power to ensure $p \ll 1$ [11]. Heralding rates can still be relatively high even in this case due to the large repetition rate available in our system.

The thermal microwave occupancy is difficult to predict from first principles but could be degraded due to absorption of pump light in the superconducting resonator or the device waveguides and packaging. The measurements described in Chapter 5, as well as other recent work on electro-optic transducers [85–87, 174], have shown that low-noise performance ($P_m < 1$) can still be achieved with relatively high average pump power $> 1\text{W}$, making direct absorption noise less of a concern. Electro-optic transducers may be able to support higher operation powers than some alternative platforms like optomechanics because they do not have low-frequency intermediate states, their fully cladded nature ensures strong thermal conductivity and they do not require colocalization of optical and mechanical modes. For a given pump power, the microwave noise can be reduced by exploring alternative superconductor materials with weak optical absorption and short quasiparticle lifetime [164], immersing devices in liquid helium [66], or using radiative cooling of the microwave mode [175]. Additionally, techniques for light blocking of superconducting qubits have been well studied [176] and could be applied to reduce the arrival of scattered light on the superconductor, similar to the package design described in Appendix D.2.

The microwave loss can be minimized using superconducting interconnects [169] and optimized protocols for conversion between flying microwave photons and superconducting qubit

Table 6.2: Target noise and loss metrics for achieving high-fidelity raw entanglement.

p	P_m	P_{loss}	P_{false}	P_{phase}	F
0.02	0.02	0.08	$\ll 10^{-3}$	0.01	> 0.8

systems [37, 172, 177, 178]. Overcoupling the transducer microwave resonator so that $\kappa_{m,e} \gg \kappa_{m,i}$ is also critical to minimizing microwave loss. The large loss rates $\kappa_m \sim 10$ MHz of currently demonstrated transducer microwave resonators may make efficient absorption challenging, and lower loss microwave resonators may need to be integrated with the transducer. Additionally, the lack of tunability inherent in the linear transducer microwave resonator means the output flying microwave photon cannot be shaped for optimal absorption. It may be possible to integrate nonlinear superconducting elements with the transducer to implement output photon shaping.

False heralding rates can be made negligible by using superconducting nanowire single-photon detectors with dark count rates < 10 Hz [179].

Finally, phase errors can be controlled with active stabilization of the optical path length of the interferometer [180].

We also note that other remote entanglement schemes based on multi-photon detection events can reduce the sensitivity to some types of noise [181–183], but these schemes come at the cost of reduced entanglement generation rates that scale as $R_{\text{ent}} \propto (\eta_{\text{opt}}p)^2$, making them impractical for our application.

Given these considerations, we predict the error rates shown in Table 6.2 are feasible targets for future system designs. These error levels would enable the generation of raw entanglement with high fidelity $F > 0.8$. Fidelity could be further improved using entanglement distillation techniques [167, 184] at the cost of reduced generation rate of useful entanglement pairs.

6.2 Future work

As shown in Table 6.1, the currently demonstrated performance of our transducer is not sufficient for useful entanglement generation, and several improvements described above are re-

quired.

First efforts could focus on using a transducer in the classical regime to generate microwave pulses from optical signals and capture those microwave pulses in a superconducting qubit system.

This set of experiments allows for testing a full node and will allow the direct investigation of several of the key engineering challenges. Calibration of pulse powers would allow the estimation of the microwave loss P_{loss} between transducer and qubit, as well as the thermal microwave noise. Monitoring qubit coherence properties during the measurement would provide insight into the compatibility of the superconducting qubit system with stray light created by the transducer. By initially using the transducer in the classical regime it is possible to study these questions with a high signal-to-noise ratio and without the need for a fully optimized transducer with integrated filtering.

Building on these initial experiments, with an improved transducer it would be possible to demonstrate the creation of the nonclassical microwave-optical photon states that are the key resource used in our remote entanglement scheme. One way to do so that has been employed with other quantum network platforms [23, 185] would involve measuring photon counting correlations between generated microwave and optical fields. In this experiment, an optical pump pulse would be sent into a transducer to generate photon pairs by spontaneous parametric downconversion as illustrated in Fig. 6.1a. One straightforward way to demonstrate the nonclassicality of these photon pairs is to measure the second-order correlation statistics $g_{ij}^{(2)} = \frac{\langle \hat{a}_i^\dagger \hat{a}_j^\dagger \hat{a}_i \hat{a}_j \rangle}{\langle \hat{a}_i^\dagger \hat{a}_i \rangle \langle \hat{a}_j^\dagger \hat{a}_j \rangle}$, where \hat{a}_i is the annihilation operator for the optical or microwave mode and $i = \{o, m\}$. Classically, it can be shown that the Cauchy-Schwartz type inequality

$$g_{mo}^{(2)} \leq \sqrt{g_{mm}^{(2)} g_{oo}^{(2)}} \quad (6.4)$$

holds. Breaking this inequality demonstrates creation of a nonclassical correlated microwave-optical photon state [23]. Recently developed methods for measuring the correlation function of microwave fields using low noise amplifiers [186] make this experiment relatively straightforward if a sufficiently high-performance transducer can be made.

The measured second-order cross correlation $g_{mo}^{(2)}$ serves as a useful figure of merit for the quality of the generated photon pair state, which would inform the decision to begin the investigation of a full, two-transducer single-link system. Sources of noise such as thermal occupation of the microwave mode, false optical detection events (due to leaked pump light or dark counts), and multi-pair generation events must be small to prevent degradation of the cross correlation $g_{om}^{(2)}$ and preserve the inequality in Eq. 6.4. The second-order cross correlation $g_{om}^{(2)}$ can be interpreted as a ratio of the average occupancy of the microwave mode after heralding an optical photon to the total average occupancy of the thermal mode:

$$g_{om}^{(2)} = \frac{\langle \hat{a}_o^\dagger \hat{a}_o^\dagger \hat{a}_m^\dagger \hat{a}_m \rangle}{\langle \hat{a}_o^\dagger \hat{a}_o \rangle \langle \hat{a}_m^\dagger \hat{a}_m \rangle} = \frac{\eta_{\text{opt}} p \langle \hat{a}_m^\dagger \hat{a}_m \rangle_{\text{heralded}}}{\eta_{\text{opt}} p \langle \hat{a}_m^\dagger \hat{a}_m \rangle}, \quad (6.5)$$

where $\eta_{\text{opt}} p$ is the heralding probability. In a simple model neglecting the impact of noise, the normalized pair generation probability is $\frac{p}{1+p}$ and $g_{om}^{(2)} = 1 + \frac{1}{p}$. Including the sources of noise above, the expected second-order cross correlation is

$$g_{om}^{(2)} = \frac{1 + P_m - P_{\text{false}}}{p + P_m}, \quad (6.6)$$

showing that the second-order cross correlation is a good metric for the practical noise level of pair generation.

The optical and microwave states are expected to be Gaussian and so that $g_{oo}^{(2)} = g_{mm}^{(2)} = 2$. Thus demonstration of nonclassical correlations requires that $g_{om}^{(2)} < 2$, which can be achieved if $\{P_{\text{false}}, P_m\} \lesssim 0.3$. This limit appears achievable based on the considerations listed above. It is interesting to note that non-classical correlations can still be demonstrated even in the case where $p \ll P_m$, i.e. where the average signal occupation is much smaller than the noise occupation. This is because the detection of an optical photon heralds the existence of a photon in the microwave resonator, assuming $P_{\text{false}} \ll 1$. This heralding ensures that the requirement to demonstrate non-classical correlations is $P_m \ll 1$, rather than the more difficult $P_m \ll p$.

The practical feasibility of this experiment to demonstrate non-classical electro-optic correlations is based on the ability to collect enough photon-counting events to measure the in-

equality of Eq. 6.4 with sufficient statistical power. To do so, the detection rate of SPDC photons must be high enough to overcome detector dark counts and enable sufficient counting statistics to be collected in a reasonable experimental time frame. Three correlations need to be measured in this experiment: $g_{mo}^{(2)}$, $g_{oo}^{(2)}$, and $g_{mm}^{(2)}$. Of these, we estimate that $g_{oo}^{(2)}$ will require the longest measurement time because the high optical insertion loss due to optical coupling and filtering makes optical photons more difficult to collect than microwave photons (for which near-quantum limited amplification can be used [165, 187]). Using Poisson statistics, the measurement time to achieve a given signal-to-noise ratio SNR in a measurement of $g_{oo}^{(2)}$ is $T = \frac{\text{SNR}^2}{\eta_{\text{opt}}^2 p^2 R}$. This indicates a reasonable measurement time of 3 hours for near-term performance parameters of SNR=10, $\eta_{\text{opt}} = -20$ dB, $p=0.01$, and $R=1$ MHz.

Verifying the nonclassical nature of the microwave-optical correlations would indicate the devices have reached a benchmark where entanglement generation should be possible. The key additional challenge of creating a full two-transducer system is ensuring that the optical states produced by the transducers in both nodes are indistinguishable. The tunability provided by the thin-film lithium niobate platform makes achieving this indistinguishability feasible. However, complete control of the resonance frequencies of both optical modes requires an additional DC tuning port in the capacitor, which may somewhat reduce the interaction strength g_0 of the transducer. Alternatively, frequency shifting devices could be used to ensure indistinguishability [188]. Characterization of the remote entanglement created by a single link system – using standard entanglement witness metrics [189] – would allow measurement of the entanglement generation rate R_{ent} and fidelity F , which are key parameters for the full system architecture.

Appendix A

Definitions

A.1 Acronyms

LN	Lithium niobate
TFLN	Thin-film lithium niobate
EO	Electro-optic(s)
CEO	Cavity electro-optic(s)
SPDC	Spontaneous parametric down conversion
SOI	Silicon-on-insulator
Q	Quality factor
TE, TM	Transverse-electric and transverse-magnetic
CPW	Coplanar waveguide
SNR	Signal-to-noise ratio
SMA	Subminiature version A - a type of coaxial cable connector
PCB	Printed circuit board
CW, CCW	Clockwise and counter-clockwise
ESA	Electrical spectrum analyzer
OSA	Optical spectrum analyzer
TWPA	Travelling wave parametric amplifier

MXC	Mixing chamber plate
VTS	Variable temperature source

A.2 Mathematical notation

ω (f)	Angular (ordinary) frequency
\hat{a}_k	Photon annihilation operator for optical-frequency mode k
\hat{b}	Photon annihilation operator for microwave-frequency mode
μ	Linear coupling rate between optical modes, producing frequency splitting
	2μ
G_i	Optical frequency shift per volt for physical ring i
$g_{i \neq 0}$	Vacuum electro-optic coupling rate for i th mode frequency shifting
g_0	Vacuum electro-optic coupling rate between hybrid modes
g	Pump-enhanced electro-optic coupling rate between hybrid modes
C	Effective capacitance of microwave resonator
C	Multiphoton cooperativity $C = \frac{4g^2}{\kappa_k \kappa_l}$
E	Electric field
r	Electro-optic coefficient
l	Optical resonator length
n	Index of refraction
n_g	Group index
n_{eff}	Mode effective phase index
α	Spatial (effective) fraction of a ring-resonator covered by electrodes
ϵ	material permittivity, ϵ^* denotes complex permittivity
δ	Intrinsic frequency detuning between two uncoupled optical modes
u, v	Hybrid optical mode constants
θ	Optical mode hybridization parameter
β	Non-degeneracy penalty factor in g_0 , $\beta = 2uv$ or geometry factor

V	Voltage or mode volume
d	Effective capacitor gap distance
Γ	Susceptibility of waveguide effective index to changes in core index
N, n	Average photon number
α_k	Coherent state amplitude of mode k
$\kappa_k, \kappa_{k,e}, \kappa_{k,i}$	Total, extrinsic, and intrinsic energy decay rate for mode k
$Q_k, Q_{k,e}, Q_{k,i}$	Total, extrinsic, and intrinsic quality factor rate for mode k , $Q_k = \omega_k / \kappa_k$
ν_k	Coupling ratio for mode k , $\nu_k = \kappa_{k,e} / \kappa_{k,i}$
ω_L	Laser frequency
Δ_k	Frequency detuning between mode k and laser $\Delta_k = \omega_L - \omega_k$
η	Insertion loss or efficiency
S_{ij}	Scattering matrix component
P	Optical pump power
G	Gain factor or transfer function
B	Bandwidth
T	Temperature
k_b	Boltzman's constant
σ	Conductivity
κ_s	Surface conductivity
p	Pair generation probability
$\Delta\phi$	Phase difference
R	Repetition rate or resistance
$g_{ij}^{(2)}$	Second order correlation function between modes i and j
P_i	Error probability for error source i
F	Fidelity

Appendix B

Additional theory results

B.1 Bidirectional resonator coupling

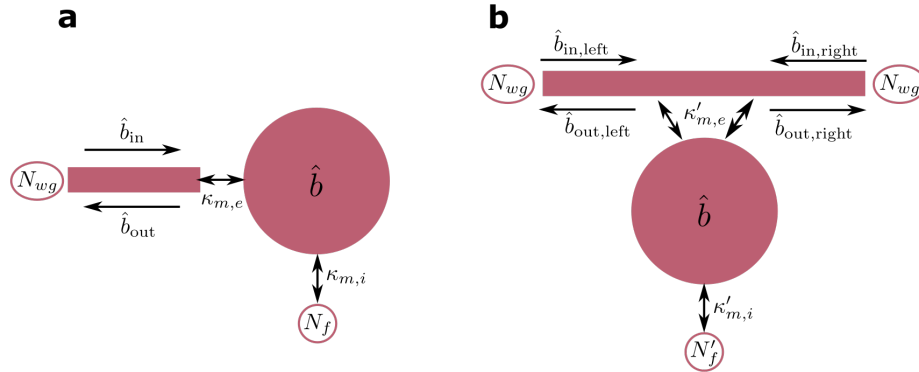


Figure B.1: Comparison of unidirectional (a) and bidirectional (b) coupling to a microwave mode \hat{b} .

The electro-optics theory in Chapter 2 was derived for resonators with unidirectional coupling, as illustrated schematically in Fig. B.1a. However, the microwave resonators in our device are capacitively coupled to a bidirectional transmission line, illustrated in Fig. B.1b. Nonetheless, all the results of Chapter 2 can be applied to the bidirectionally coupled microwave resonator used in our devices with the following substitutions

$$\kappa_{m,i} = \frac{\kappa'_{m,e}}{2} + \kappa'_{m,i} \quad (\text{B.1})$$

$$\kappa_{m,e} = \frac{\kappa'_{m,e}}{2} \quad (\text{B.2})$$

$$\hat{b}_{\text{in}} = \hat{b}_{\text{in,left}} \quad (\text{B.3})$$

$$\hat{b}_{\text{out}} = \hat{b}_{\text{out,right}} \quad (\text{B.4})$$

$$\hat{b}_f = \sqrt{\frac{\kappa'_{m,e}}{\kappa_{m,i}}} \hat{b}_{\text{in,right}} + \sqrt{\frac{\kappa'_{m,i}}{\kappa_{m,i}}} \hat{b}_f \quad (\text{B.5})$$

$$N_f = \frac{\kappa'_{m,e}}{\kappa_{m,i}} N_{wg} + \frac{\kappa'_{m,i}}{\kappa_{m,i}} N'_f \quad (\text{B.6})$$

where the primed quantities $\kappa'_{m,k}$, $k = \{i, e\}$ refer to the true intrinsic and extrinsic loss rates for the resonator and \hat{b}'_f is a super-mode operator that refers to the true intrinsic loss bath. The non-primed quantities are effective values for use in the unidirectional coupling model. Note that in the main text we refer to only the primed quantities when giving values for the loss rates.

B.2 Double resonance transduction

When the converter is operated far-detuned from the triple-resonance condition, a double-resonance transduction process can become a significant contribution to the total transduction efficiency. In this process, optical photons in the red optical mode can be scattered between the pump frequency and a blue-shifted sideband. This sideband field is far-detuned from the red optical mode relative to the mode's linewidth in our experiments, so the transduction efficiency for this process is low, but it can be larger than that of the triple-resonance process when the splitting between red and blue optical modes is much larger than the microwave frequency. This double-resonance process is the origin of the bias-voltage independent response for large negative voltages in Figs. 3.3b and 3.3c above. The nonlinear energy density that

describes this double-resonance process is [118]

$$U = \epsilon_0 \chi^{(2)} E_m E_-^2 \quad (\text{B.7})$$

which produces the Hamiltonian

$$H_I = \hbar g_{0,\text{dr}} \left(b a_-^\dagger a_- + b^\dagger a_-^\dagger a_- \right), \quad (\text{B.8})$$

where

$$g_{0,\text{dr}} = \frac{\chi^{(2)} \omega_{\text{opt}}}{d_{\text{eff}} V_{\text{opt}} n^2} \sqrt{\frac{\hbar \omega_m}{2C}} \int dV |\psi_+|^2 \psi_m. \quad (\text{B.9})$$

Following the usual linearization procedure for the strongly pumped a_- mode [190], we approximate $a_- \approx \langle a_- \rangle + \delta a_-$, where δa_- is a small fluctuating perturbation to the field in the red optical mode. Keeping terms of order $\langle a_- \rangle$, the linearized interaction Hamiltonian is

$$H_I = \hbar g_{\text{dr}} \left(\delta a_-^\dagger + \delta a_- \right) \left(b^\dagger + b \right), \quad (\text{B.10})$$

where $g_{\text{dr}} = g_{0,\text{dr}} \langle a_- \rangle$. This Hamiltonian contains both the desired beam-splitter terms and parametric amplification terms which cause optical down conversion, and since the pump is nearly resonant with the red optical mode, both types of terms are significant. In a frame where the optical mode rotates along with the laser, the semi-classical Heisenberg-Langevin equations of motion for double-resonance microwave-to-optical transduction are

$$\begin{aligned} \frac{d(\delta a_-)}{dt} &= - \left(-i\Delta_- + \frac{\kappa_-}{2} \right) \delta a_- - i g_{\text{dr}} \left(b + b^\dagger \right), \\ \frac{db}{dt} &= - \left(i\omega_m + \frac{\kappa_m}{2} \right) b - i g_{\text{dr}} \left(\delta a_- + \delta a_-^\dagger \right) + \sqrt{\kappa_{m,e}} b_{\text{in}} e^{-i\omega t}. \end{aligned} \quad (\text{B.11})$$

For simplicity, we assume that the double resonance process operates in the weak coupling regime, so that back-action of the optical fields on the microwave field can be neglected¹. We

¹i.e. the term $-i g_{\text{dr}} \left(\delta a_- + \delta a_-^\dagger \right)$ can be dropped

take the ansatz solution

$$\begin{aligned}\delta a_-(t) &= A_+ e^{-i\omega t} + A_- e^{i\omega t}, \\ b(t) &= B e^{-i\omega t},\end{aligned}\tag{B.12}$$

and find

$$\begin{aligned}B &= \frac{\sqrt{\kappa_{m,e}} b_{\text{in}}}{i(\omega_m - \omega) + \kappa_m/2} \\ A_{\pm} &= \frac{-i g_{\text{dr}} B}{-i(\Delta_- \pm \omega) + \kappa_-/2}.\end{aligned}\tag{B.13}$$

The transmitted optical sideband field due to double-resonance transduction is $\delta a_{\text{out}} = -\sqrt{\kappa_{-,e}} \delta a_-$, and hence the total apparent transduction efficiency², including both double- and triple- resonance transduction, is

$$\eta_{\text{oe}} = |S_{\text{eo}} - \sqrt{\kappa_{-,e}} A_+ - \sqrt{\kappa_{-,e}} A_-^*|^2.\tag{B.14}$$

²The existence of multiple optical sidebands in regimes where double-resonance transduction is significant means that transduction efficiency must be carefully defined. In our experiments, we measure only the transmission of a microwave signal from the transducer's input to the photoreceiver's output, and we cannot differentiate multiple optical sidebands. As such, we define transduction efficiency for multiple sidebands as the apparent transduction efficiency: i.e. the equivalent single-sideband transduction efficiency which would produce the observed signal. Note that this distinction between apparent and true transduction efficiency is significant only in far-detuned regimes of bias voltage sweeps, not near the triple-resonance condition where maximum transduction efficiency occurs.

Appendix C

Microwave resonators

C.1 Capacitive coupling

One of the benefits of using our thin-film lithium niobate platform is that a large number of the roughly 1 mm^2 can be fabricated on a single wafer. This scalability enables us to test several device geometries (e.g. different evanescent coupling gaps) simultaneously and could enable large-scale parallelization in the future.

However, the relatively large size of our microwave resonators means that capacitive coupling between them can be significant. We observed the effects of strong capacitive coupling in several test devices. The results of one chip are shown in Figure C.1. As shown in Fig. C.1a, the devices on this chip are closely spaced. This close spacing leads to resonance features in the transmission spectrum with widely varying extinction, shown in Fig. C.1b. Fitting these resonance features, we extract the external quality factor of the modes we observe at different frequencies in Fig. C.1c. These external quality factors vary almost 100-fold even though the devices on this chip have nearly identical coupling gaps to the bus coplanar waveguide (CPW).

We attribute this wide variation in the coupling strength of these modes to capacitive coupling between microwave resonators. If the coupling rates between devices are significant compared to the differences in the resonance frequency of individual devices, then large-scale hy-

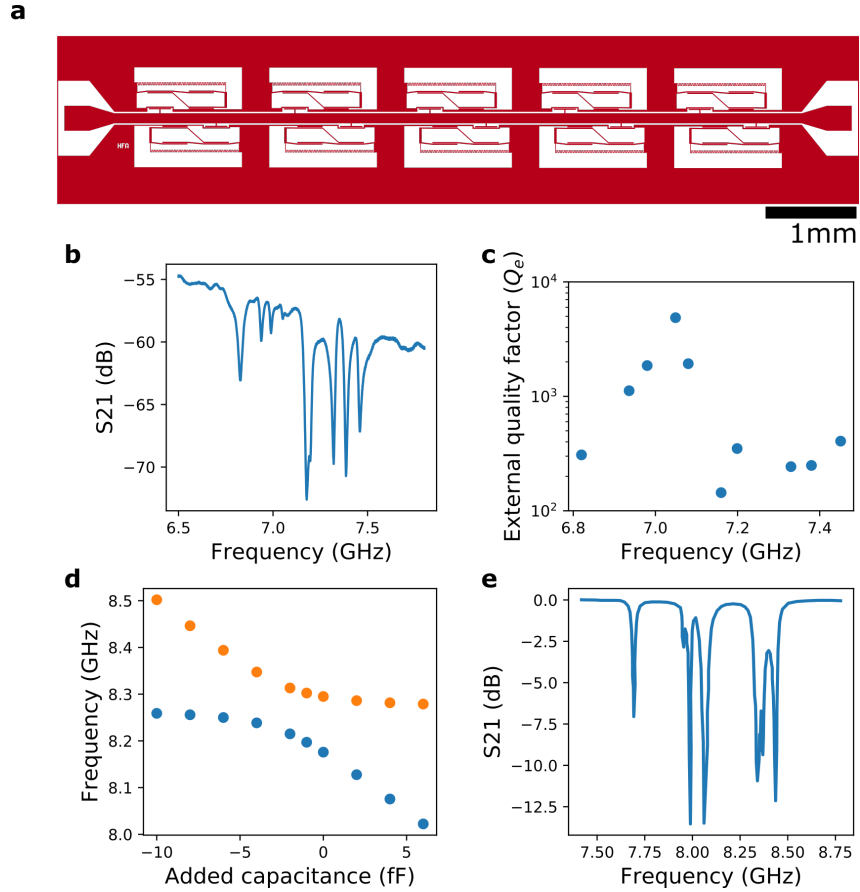


Figure C.1: Capacitive coupling of microwave resonators in a high-density transducer layout. (a) NbN superconductor layer layout of the device. (b) Measured microwave transmission spectrum at $T = 1.2$ K. (c) External quality factors extracted for the resonance features observed in the measured transmission spectrum. (d) Simulated resonance frequencies of two neighboring LC resonators for different values of added capacitance on the second resonator. We observed a clear anticrossing with minimum mode splitting of 100 MHz (e) Simulation of full device layout shown in (a). We observe qualitative similarities with the measured spectra above in (b).

brid modes will be created that have energy distributed across all or many of the physical resonators. These large-scale hybrid modes may have enhanced or reduced coupling to the bus CPW depending on the phase relationship between resonators in the mode. This effect of capacitive coupling has been observed for other closely-packed resonator devices [191]. If such hybrid modes are used for transduction, the efficiency could be significantly reduced due to the larger mode volume of the hybrid microwave modes.

To verify this understanding, we performed several simulations of the chip using Sonnet [192].

To estimate the strength of the capacitive coupling, we simulated two identical neighboring resonators and added an extra lumped-element capacitor to one of the resonators. By changing this added capacitance and simulating the resonance frequencies, we mapped out the anticrossing between the two resonator modes, as shown in Fig. C.1d. Based on the minimum splitting between hybrid modes, we estimate a capacitive coupling rate of

$$\frac{\mu}{2\pi} = \frac{C_{12}}{C_{11}} f_0 = 50 \text{ MHz}, \quad (\text{C.1})$$

where C_{12} is the coupling capacitance between two LC resonators, C_{11} is the total capacitance of one resonator, and f_0 is the resonance frequency of a single resonator. This coupling rate is significant compared to the designed frequency step between devices of $\Delta f_0 = 70$ MHz, lending credence to our interpretation.

To further verify this understanding, we performed a full simulation of the chip with all 10 devices. The simulated transmission spectrum is shown in Fig. C.1e and displays qualitative similarity to the measured results of Fig. C.1b in that the extinction of the resonance features varies widely. The quantitative differences are expected due to the random variability of the resonance frequency in fabricated devices: small changes in resonant frequencies can have significant effects on the large-scale hybrid modes.

To avoid the effects of capacitive coupling, we simulate the capacitive coupling rate between microwave resonators in the transducers described in the main text. In our final chips, we ensure that devices are separated in physical and frequency space sufficiently to make such

coupling negligible.

C.2 Niobium nitride resonator of Chapter 3

To minimize the microwave mode volume and maximize the single-photon interaction strength, we designed a superconducting quasi-lumped microwave LC resonator, which is (predominantly) capacitively coupled to a $50\ \Omega$ characteristic impedance coplanar waveguide. The niobium nitride superconducting film used to make the resonator has a relatively high sheet kinetic inductance of $\sim 5\ \text{pH}/\square$, which allows for a more compact inductor design. Using a method of moments simulation [192], we estimate the effective lumped capacitance and inductance by varying the magnitude of a small ideal capacitance added in parallel. The change in resonance frequency with added capacitance allows us to determine the total capacitance and inductance [132]. We simulate the lumped element circuit parameters to be $C = 120\ \text{fF}$, $L = 6.7\ \text{nH}$, and $\omega_m/2\pi = (LC)^{-1/2} = 5.6\ \text{GHz}$. We attribute the somewhat lower measured resonance frequency to variations in the as-fabricated geometry of the devices. In particular, the width of the meander inductor is narrower than designed due to a small degree of mask erosion.

We use a two-dimensional finite element model to simulate the piezoelectric loss of the microwave resonator. In this frequency-domain simulation, a voltage is applied to the capacitor electrodes at frequency ω , and the time-averaged electrostatic energy $E_{\text{electrostatic}}$ and acoustic power absorbed by the perfectly-matched layer P_{acoustic} are calculated. The quality factor set by piezoelectric loss is then given by

$$Q = \frac{\omega E_{\text{electrostatic}}}{P_{\text{acoustic}}}. \quad (\text{C.2})$$

The two-dimensional nature of the simulation means that acoustic modes with out-of-plane (i.e. along the waveguide) propagation or strain are neglected. Modes with an out-of-plane propagation direction couple weakly to the microwave resonator because the capacitor is much longer than the acoustic wavelength at the relevant $\sim\text{GHz}$ frequencies. Modes with out-of-

plane stress also couple weakly to the microwave resonator for X-cut lithium niobate because of lithium niobate’s piezoelectric coefficients. For example, when applying the electric field along the Z crystal axis in our device the d_{33} piezoelectric coefficient, which creates in-plane stress, dominates over other components.

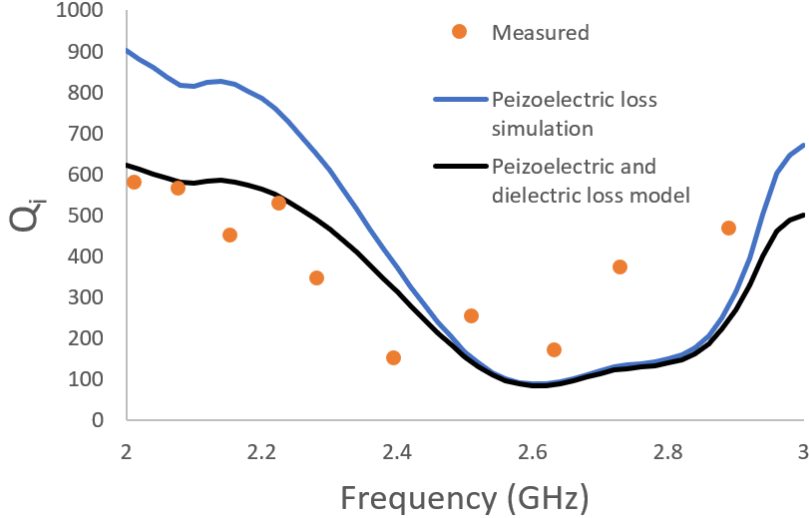


Figure C.2: Dependence of microwave resonator loss on resonance frequency. Measured data was inferred from transmission spectra ($T = 1$ K) of LC resonators similar to those described in the main text. The piezoelectric loss model is based on the two-dimensional simulations described above. The dielectric loss model adds an additional wideband loss corresponding to $Q_{\text{clad}} = 2000$

To verify the role of piezoelectric loss in our device, we fabricated an array of transducer devices without etched optical waveguides — i.e. just the microwave resonators on the material stack described in the main text. We created devices with microwave resonance frequencies varying from 2 to 3 GHz by varying the inductor size. Measuring transmission spectra at $T = 1$ K, we extract the intrinsic loss for the resonators, shown in Fig. C.2. The sharp and non-monotonic frequency dependence of the microwave loss is evidence of piezoelectric loss, as most other loss mechanisms vary slowly with frequency in this range. Our simulation results qualitatively match the sharp frequency dependence in the measured data but predict much higher maximum intrinsic quality factors. We attribute this discrepancy to additional wideband dielectric loss in the amorphous cladding material. To confirm this, we fabricated devices without lithium niobate or amorphous oxide layers on a high-resistivity silicon substrate and found intrinsic quality factors exceeding 10^4 .

C.2.1 Resonator nonlinearity

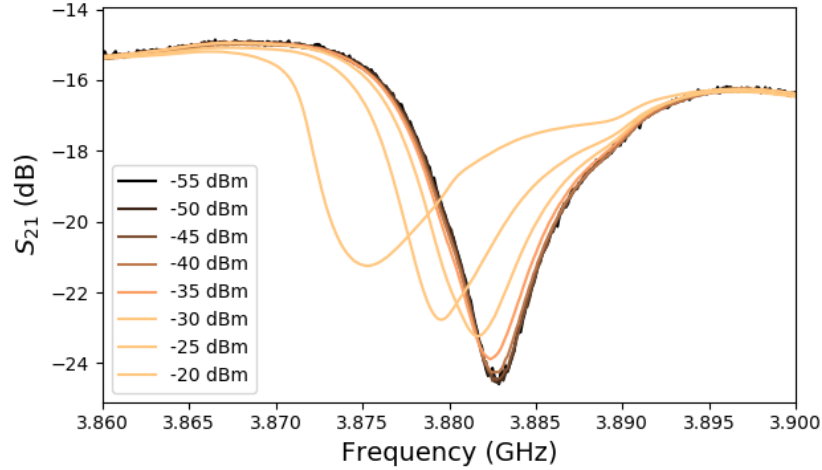


Figure C.3: Power dependent microwave transmission. Microwave input powers above about -40 dBm at port V1A (~ -48 dBm on-chip) produce distorted transmission spectra due to nonlinear dynamics. [131]

The superconducting NbN film is deposited using DC magnetron sputtering at room temperature with an RF bias on the substrate holder. The film has a thickness of ~ 44 nm, room-temperature sheet resistance of $52 \Omega/\text{square}$, and a transition temperature T_c of ~ 10 K. At high microwave powers, the superconducting resonator undergoes nonlinear oscillations [131], as shown in Fig. C.3. In the actual experiment, the drive power is kept below -30 dBm, and the nonlinear dynamics are therefore small.

Appendix D

Experimental methods

D.1 Setup for Chapter 3

Details of the measurement setup are shown in Figure D.1. To calibrate the transduction efficiency, we perform the following procedure before every set of measurements.

First, with the laser frequency detuned far from the optical resonance, we measure the optical power into and out of the device under test (DUT). After correcting for measured asymmetric losses in the optical fibers going into the cryostat, we assume the loss at both input and output grating couplers to be symmetric. Based on measurements of a large number of grating couplers, we estimate the coupler-to-coupler variation in insertion loss to be less than 0.4 dB. Next, we measure the optical power arriving at the output of the analysis arm using the DC power meter. These measurements allow us to estimate the optical insertion loss from the DUT to the end of the analysis arm $\eta_{\text{optical}} = \eta_{\text{coupler}} \cdot \eta_{\text{fiber}}$, as well as the on-chip optical power.

Next, we calibrate the response of the 10 GHz-bandwidth photoreceiver by using port V1 to generate a single optical sideband. We measure the signal in the analysis arm using the high-resolution optical spectrum analyzer (which allows us to directly measure the relative power of the sideband and carrier $P_{\text{sideband}}/P_{\text{pump}}$), the calibrated DC power meter (which measures the total power $P_{\text{sideband}} + P_{\text{pump}}$), and the 10 GHz photoreceiver. These measure-

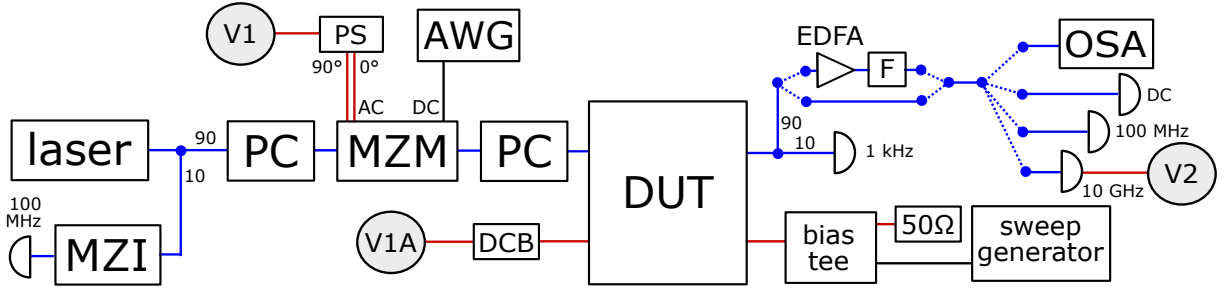


Figure D.1: Simplified diagram of the transduction measurement setup. Laser emission passes through polarization controllers (PC) and is modulated by a Mach-Zehnder modulator (MZM). A fraction of the emission is sent to a 100 MHz-bandwidth detector after passing through a Mach-Zehnder interferometer (MZI) of ~ 1 m path length difference to precisely track sweeps of laser wavelength. The MZM is arranged for either GHz-frequency optical single-sideband modulation using a phase-shifted (PS) dual drive through a high-frequency port, or low-frequency amplitude modulation through a bias port, controlled by an arbitrary waveform generator (AWG). Focusing grating couplers (≈ 10 dB insertion loss) couple light from optical fibers into the device under test (DUT), which is cooled to $T \approx 1$ K inside a closed-cycle cryostat. The light collected from the DUT is split into an analysis arm (90%) and a 1 kHz photoreceiver (10%), whose signal is used to lock the laser frequency to an optical mode. The analysis arm passes through several optical switches (dotted blue lines) which allow for optional and repeatable insertion of an erbium-doped fiber amplifier (EDFA) and optical filter (F, 0.2 nm bandwidth). The analysis arm can be sent to an optical spectrum analyzer (OSA) for sideband calibration, a DC optical power meter for power calibration, a 100 MHz photoreceiver for measuring transmission spectra, or a 10 GHz photoreceiver for detecting transduction. The bias voltage of the DUT is controlled by a sweep generator through a bias tee. A vector network analyzer (VNA) can be connected to microwave port V1A, which is protected by a DC block (DCB) capacitor, to excite the DUT. The upconverted optical signal can be detected at port V2. In an alternative measurement setup, the transmission of an optical sideband can be monitored by connecting the VNA to the optical single-sideband modulator (port V1).

ments allow us to estimate the detector response parameter $A_{\text{det.}}$, defined so that $P_{\text{det.}} = A_{\text{det.}} P_{\text{sideband}} P_{\text{pump}}$.

During the transduction measurement, when the laser frequency is locked to an optical mode, measurements of the total optical power and the 10 GHz photoreceiver response allow us to infer the power in the upconverted optical sideband P_{sideband} , based on the above photoreceiver calibration. The gain provided by the erbium-doped fiber amplifier (EDFA), if in use, can be estimated by measuring the photoreceiver response with and without the EDFA in the optical path. Finally, the calibrated transduction efficiency is given by

$$\eta = \frac{\omega_m P_{\text{sideband}}}{\omega_o P_{\text{in}} \eta_{\text{optical}} \eta_{\text{cable}}}, \quad (\text{D.1})$$

where P_{in} is the input microwave power at port V1A and η_{cable} is the measured insertion loss from port V1A to the DUT.

D.2 Device packaging and optical coupling

The method used to mount the chip in the cryogenic environment while also providing microwave and optical access is shown below in Fig. D.2.

We use grating couplers to couple light into the devices. We use adiabatic grating couplers with taper length of $400 \mu\text{m}$, a pitch of $0.75 \mu\text{m}$, and an un-etched region duty cycle of 0.25. With the fabrication procedure described below (see Section D.3.2), this design produces a minimum insertion loss (fiber-to-fiber) of $9.4 \pm 0.3 \text{ dB}$ (measured across $N=12$ devices) at 1568 nm , with a 3 dB bandwidth of roughly 40 nm .

Fig. D.2a shows a render of the chip mounting apparatus. A 3-axis stack of Attocube linear piezomotors is used to position an optical fiber array precisely over the grating couplers, allowing optimization of optical coupling even while the device is cold. This ability to reposition the optical fiber array throughout the experiments is useful because it allows us to compensate for temperature-induced movements during cooldown while also providing the ability to interrogate multiple devices on one chip. When the cryostat is closed, we do not have visual

access to the apparatus and our positioners are open-loop, i.e. do not provide built-in position sensors. To navigate around the chip with the optical fiber array in these conditions, we pattern fidelity marks into the superconductor layer of the chip near the grating couplers and monitor the optical transmission from one fiber to another as we move the fiber array. When the fiber array is positioned above an area of the chip without a superconductor layer, the light from the array travels through the chip and scatters off the silver paste on the backside of the chip. This diffuse reflection provides roughly 50 to 70 dB of optical return loss. When the fiber array is instead positioned over the reflective superconductor layer, any light that is reflected does so in a specular manner, and the return loss is above what can be measured on our detector. > 80 dB. Using this difference we can read out the fidelity marks by slowly scanning the fiber array across them.

We enclose the part of the chip containing the transducers in a nearly complete copper box (Fig. D.2a) to help protect the transducers from scattered light. The other part of the chip extends outside the box where optical coupling occurs. The copper box is built from three separate machined parts: a base, a collar that holds the SMA connectors, and a lid. This three-part design allows the chip to sit on a completely flat polished copper surface to maximize thermal conductance between the chip and base. The chip is glued down to the base using silver paste (PELCO No. 16047) and further secured lightly (excess pressure can break the chip) using two copper clips as shown in Fig. D.2b. Finally, the chip is wirebonded to the PCB that interposes between the chip and an SMA connector. The whole apparatus is then mounted to the mixing chamber plate of a Bluefors LD250 dilution refrigerator.

D.3 Device fabrication

In this section, we present the detailed fabrication procedure used to make the transducers described in Chapter 3 and 5.

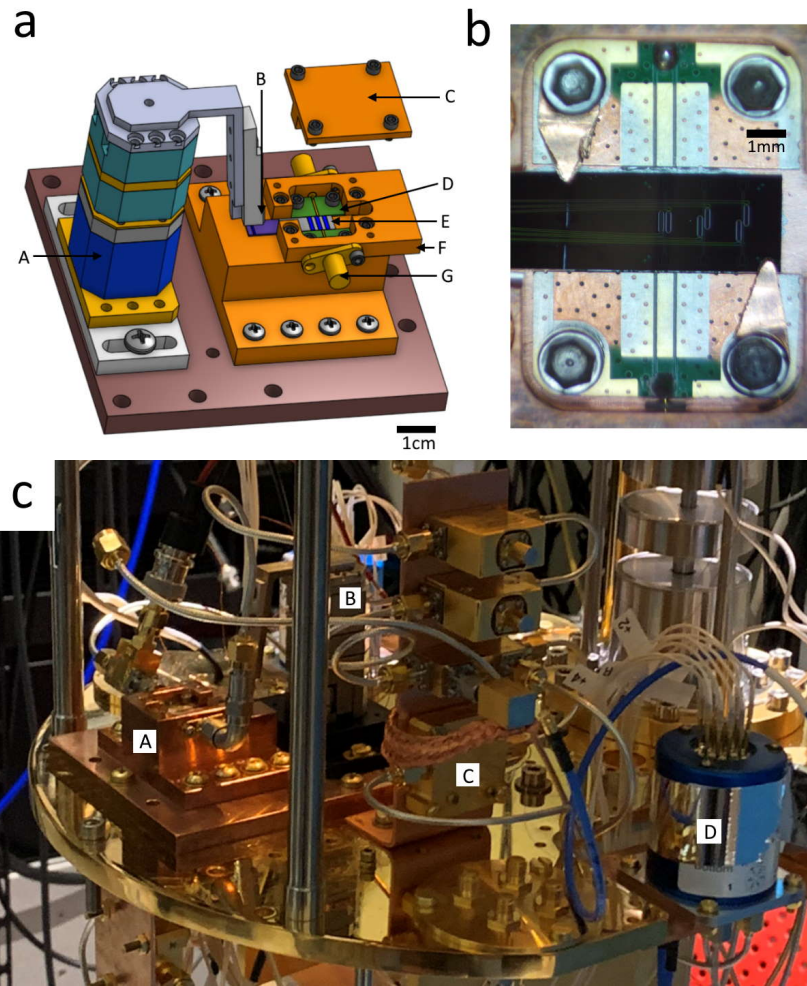


Figure D.2: Setup for packaging and mounting device from Chapter 5. (a) Render of the sample mounting and optical coupling hardware. A- 3-axis Attocube positioner stack. B- Optical fiber array. C- Package lid to block scattered light from the chip. D- High-frequency Rogers RO4350 printed circuit board to adapt between microwave connector and chip. E- chip. F- mounting "collar": building the microwave packaging box in two parts like this allows the chip to sit on a perfectly flat, polished surface. G- SMA connector. (b) Microscope image of the packaged chip before wirebonding. (c) Image of the mixing chamber plate. A- packaged device. B- Attocube stack. C- microwave amplifier chain. D- Coaxial switch.

D.3.1 Device fabrication for Chapter 3

Beginning with a diced and cleaned chip from a TFLN wafer (NanoLN) with a 600 nm-thick LN layer, 2 μm -thick buried oxide layer, and 525 μm -thick silicon substrate, we deposit roughly 20 nm of silicon nitride using plasma-enhanced chemical vapor deposition (PECVD). We then spin a layer of hydrogen silsesquioxane (Corning FOx-16) resist approximately 700 nm thick and use electron-beam lithography to pattern the optical waveguide layer. We write the patterns with a 4X multipass process to reduce loss from field stitching errors [193]. We etch the pattern 350nm into the LN layer using an optimized argon-based inductively-coupled plasma reactive ion etcher followed by cleaning in SC-1 solution and dilute HF to remove the etch re-deposition products and etch mask. We use PECVD to deposit a silicon dioxide cladding layer 1.5 μm thick to protect the waveguide. To improve the low-frequency response of the electro-optic bias capacitor, we use a C_3F_8 -based reactive ion plasma to etch through the cladding layer. We then use DC magnetron sputtering to deposit 44nm of niobium nitride and pattern this film using optical lithography and a CF_4 -based plasma etch.

D.3.2 Device fabrication for Chapter 5

The fabrication process proceeds similarly to that described above with the following differences. The initial chip is composed of a TFLN wafer with a 600 nm-thick LN layer, 4.7 μm -thick buried oxide layer, and 525 μm -thick silicon substrate. The thicker buried oxide layer improves grating coupler efficiency. After etching, we anneal the device for 2 hours in a tube furnace with an oxygen atmosphere at 520 $^\circ\text{C}$. We then use an optimized high-pressure, low-temperature PECVD process to deposit the cladding silicon dioxide and anneal the device again using the same procedure. To improve the electro-coupling (as described in Chapter 5), we etch through the top cladding layer as before, but switch to the argon-based plasma to also etch through the LN slab - see Fig. 5.2. Finally, we sputter a 40 nm layer of niobium and pattern it as before to complete the microwave resonator.

In Chapter 5, device "CEO11" uses a PECVD cladding procedure with the following settings: pressure: 8 mTorr, ICP power: 1320 W, O_2 gas flow: 18 sccm, and silane/He gas flow

rate 360 sccm. In contrast for device "CEO14" we use a PECVD cladding procedure with different settings: pressure: 8 mTorr, ICP power: 1500 W, O₂ gas flow: 21 sccm, and silane/He gas flow rate 300 sccm. As described in Chapter 5, we observe noticeably lower optical quality on device "CEO11".

References

- [1] Cisco, “Annual Internet Report (2018–2023) White Paper,” Mar. 2020.
- [2] K. C. Kao and G. A. Hockham, “Dielectric-fibre surface waveguides for optical frequencies,” *Proceedings of the Institution of Electrical Engineers*, vol. 113, pp. 1151–1158, July 1966.
- [3] C. K. Kao, “Nobel Lecture: Sand from centuries past: Send future voices fast,” *Reviews of Modern Physics*, vol. 82, pp. 2299–2303, Aug. 2010.
- [4] Y. Tamura, H. Sakuma, K. Morita, M. Suzuki, Y. Yamamoto, K. Shimada, Y. Honma, K. Sohma, T. Fujii, and T. Hasegawa, “The First 0.14-dB/km Loss Optical Fiber and its Impact on Submarine Transmission,” *Journal of Lightwave Technology*, vol. 36, pp. 44–49, Jan. 2018.
- [5] H. Kaushal, V. K. Jain, and S. Kar, *Free Space Optical Communication*. Springer, 1st ed. 2017 edition ed., Jan. 2017.
- [6] C. Brackett, “Dense wavelength division multiplexing networks: Principles and applications,” *IEEE Journal on Selected Areas in Communications*, vol. 8, pp. 948–964, Aug. 1990.
- [7] R. J. Mears, L. Reekie, I. M. Jauncey, and D. N. Payne, “Optical fiber amplifiers for 1.5- μm operation,” in *Optical Fiber Communication (1988)*, Paper ThD3, p. ThD3, Optica Publishing Group, Jan. 1988.
- [8] H. J. Kimble, “The quantum internet,” *Nature*, vol. 453, pp. 1023–1030, June 2008.
- [9] J. I. Cirac, P. Zoller, H. J. Kimble, and H. Mabuchi, “Quantum State Transfer and Entanglement Distribution among Distant Nodes in a Quantum Network,” *Physical Review Letters*, vol. 78, pp. 3221–3224, Apr. 1997.
- [10] H.-J. Briegel, W. Dür, J. I. Cirac, and P. Zoller, “Quantum Repeaters: The Role of Imperfect Local Operations in Quantum Communication,” *Physical Review Letters*, vol. 81, pp. 5932–5935, Dec. 1998.
- [11] L.-M. Duan, M. D. Lukin, J. I. Cirac, and P. Zoller, “Long-distance quantum communication with atomic ensembles and linear optics,” *Nature*, vol. 414, pp. 413–418, Nov. 2001.

- [12] M. K. Bhaskar, R. Riedinger, B. Machielse, D. S. Levonian, C. T. Nguyen, E. N. Knall, H. Park, D. Englund, M. Lončar, D. D. Sukachev, and M. D. Lukin, “Experimental demonstration of memory-enhanced quantum communication,” *Nature*, vol. 580, pp. 60–64, Apr. 2020.
- [13] V. Scarani, S. Iblisdir, N. Gisin, and A. Acín, “Quantum cloning,” *Reviews of Modern Physics*, vol. 77, pp. 1225–1256, Nov. 2005.
- [14] C. H. Bennet and G. Brassard, “Quantum cryptography: Public key distribution and coin tossing,” in *Proceedings of IEEE International Conference on Computers, Systems and Signal Processing*, vol. 175, (Bangalore, India), p. 8, IEEE, 1984.
- [15] E. Diamanti, H.-K. Lo, B. Qi, and Z. Yuan, “Practical challenges in quantum key distribution,” *npj Quantum Information*, vol. 2, pp. 1–12, Nov. 2016.
- [16] F. Xu, X. Ma, Q. Zhang, H.-K. Lo, and J.-W. Pan, “Secure quantum key distribution with realistic devices,” *Reviews of Modern Physics*, vol. 92, p. 025002, May 2020.
- [17] I. Devetak and A. Winter, “Distillation of secret key and entanglement from quantum states,” *Proceedings of the Royal Society A: Mathematical, Physical and Engineering Sciences*, vol. 461, pp. 207–235, Jan. 2005.
- [18] L. Jiang, J. M. Taylor, A. S. Sørensen, and M. D. Lukin, “Distributed quantum computation based on small quantum registers,” *Physical Review A*, vol. 76, p. 062323, Dec. 2007.
- [19] C. Monroe, R. Raussendorf, A. Ruthven, K. R. Brown, P. Maunz, L.-M. Duan, and J. Kim, “Large Scale Modular Quantum Computer Architecture with Atomic Memory and Photonic Interconnects,” *Physical Review A*, vol. 89, p. 022317, Feb. 2014.
- [20] N. H. Nickerson, J. F. Fitzsimons, and S. C. Benjamin, “Freely Scalable Quantum Technologies Using Cells of 5-to-50 Qubits with Very Lossy and Noisy Photonic Links,” *Physical Review X*, vol. 4, p. 041041, Dec. 2014.
- [21] B. B. Blinov, D. L. Moehring, L.-M. Duan, and C. Monroe, “Observation of entanglement between a single trapped atom and a single photon,” *Nature*, vol. 428, pp. 153–157, Mar. 2004.
- [22] C. M. Natarajan, M. G. Tanner, and R. H. Hadfield, “Superconducting nanowire single-photon detectors: Physics and applications,” *Superconductor Science and Technology*, vol. 25, p. 063001, Apr. 2012.
- [23] A. Kuzmich, W. P. Bowen, A. D. Boozer, A. Boca, C. W. Chou, L.-M. Duan, and H. J. Kimble, “Generation of nonclassical photon pairs for scalable quantum communication with atomic ensembles,” *Nature*, vol. 423, pp. 731–734, June 2003.
- [24] A. Reiserer, N. Kalb, G. Rempe, and S. Ritter, “A quantum gate between a flying optical photon and a single trapped atom,” *Nature*, vol. 508, pp. 237–240, Apr. 2014.
- [25] C. W. Chou, H. de Riedmatten, D. Felinto, S. V. Polyakov, S. J. van Enk, and H. J. Kimble, “Measurement-induced entanglement for excitation stored in remote atomic ensembles,” *Nature*, vol. 438, pp. 828–832, Dec. 2005.

- [26] B. Hensen, H. Bernien, A. E. Dréau, A. Reiserer, N. Kalb, M. S. Blok, J. Ruitenberg, R. F. L. Vermeulen, R. N. Schouten, C. Abellán, W. Amaya, V. Pruneri, M. W. Mitchell, M. Markham, D. J. Twitchen, D. Elkouss, S. Wehner, T. H. Taminiau, and R. Hanson, “Loophole-free Bell inequality violation using electron spins separated by 1.3 kilometres,” *Nature*, vol. 526, pp. 682–686, Oct. 2015.
- [27] A. Imamoglu, D. D. Awschalom, G. Burkard, D. P. DiVincenzo, D. Loss, M. Sherwin, and A. Small, “Quantum Information Processing Using Quantum Dot Spins and Cavity QED,” *Physical Review Letters*, vol. 83, pp. 4204–4207, Nov. 1999.
- [28] A. Reiserer and G. Rempe, “Cavity-based quantum networks with single atoms and optical photons,” *Reviews of Modern Physics*, vol. 87, pp. 1379–1418, Dec. 2015.
- [29] N. Sangouard, C. Simon, H. de Riedmatten, and N. Gisin, “Quantum repeaters based on atomic ensembles and linear optics,” *Reviews of Modern Physics*, vol. 83, pp. 33–80, Mar. 2011.
- [30] D. D. Awschalom, R. Hanson, J. Wrachtrup, and B. B. Zhou, “Quantum technologies with optically interfaced solid-state spins,” *Nature Photonics*, vol. 12, pp. 516–527, Sept. 2018.
- [31] I. Siddiqi, “Engineering high-coherence superconducting qubits,” *Nature Reviews Materials*, vol. 6, pp. 875–891, Oct. 2021.
- [32] F. Arute, K. Arya, R. Babbush, D. Bacon, J. C. Bardin, R. Barends, R. Biswas, S. Boixo, F. G. S. L. Brandao, D. A. Buell, B. Burkett, Y. Chen, Z. Chen, B. Chiaro, R. Collins, W. Courtney, A. Dunsworth, E. Farhi, B. Foxen, A. Fowler, C. Gidney, M. Giustina, R. Graff, K. Guerin, S. Habegger, M. P. Harrigan, M. J. Hartmann, A. Ho, M. Hoffmann, T. Huang, T. S. Humble, S. V. Isakov, E. Jeffrey, Z. Jiang, D. Kafri, K. Kechedzhi, J. Kelly, P. V. Klimov, S. Knysh, A. Korotkov, F. Kostritsa, D. Landhuis, M. Lindmark, E. Lucero, D. Lyakh, S. Mandrà, J. R. McClean, M. McEwen, A. Megrant, X. Mi, K. Michielsen, M. Mohseni, J. Mutus, O. Naaman, M. Neeley, C. Neill, M. Y. Niu, E. Ostby, A. Petukhov, J. C. Platt, C. Quintana, E. G. Rieffel, P. Roushan, N. C. Rubin, D. Sank, K. J. Satzinger, V. Smelyanskiy, K. J. Sung, M. D. Trevithick, A. Vainsencher, B. Villalonga, T. White, Z. J. Yao, P. Yeh, A. Zalcman, H. Neven, and J. M. Martinis, “Quantum supremacy using a programmable superconducting processor,” *Nature*, vol. 574, pp. 505–510, Oct. 2019.
- [33] N. Ofek, A. Petrenko, R. Heeres, P. Reinhold, Z. Leghtas, B. Vlastakis, Y. Liu, L. Frunzio, S. M. Girvin, L. Jiang, M. Mirrahimi, M. H. Devoret, and R. J. Schoelkopf, “Extending the lifetime of a quantum bit with error correction in superconducting circuits,” *Nature*, vol. 536, pp. 441–445, Aug. 2016.
- [34] M. Kjaergaard, M. E. Schwartz, J. Braumüller, P. Krantz, J. I.-J. Wang, S. Gustavsson, and W. D. Oliver, “Superconducting Qubits: Current State of Play,” *Annual Review of Condensed Matter Physics*, vol. 11, no. 1, pp. 369–395, 2020.
- [35] S. Krinner, S. Storz, P. Kurpiers, P. Magnard, J. Heinsoo, R. Keller, J. Lütolf, C. Eichler, and A. Wallraff, “Engineering cryogenic setups for 100-qubit scale superconducting circuit systems,” *EPJ Quantum Technology*, vol. 6, p. 2, Dec. 2019.

- [36] T. Brecht, W. Pfaff, C. Wang, Y. Chu, L. Frunzio, M. H. Devoret, and R. J. Schoelkopf, “Multilayer microwave integrated quantum circuits for scalable quantum computing,” *npj Quantum Information*, vol. 2, pp. 1–4, Feb. 2016.
- [37] J. Wenner, Y. Yin, Y. Chen, R. Barends, B. Chiaro, E. Jeffrey, J. Kelly, A. Megrant, J. Y. Mutus, C. Neill, P. J. J. O’Malley, P. Roushan, D. Sank, A. Vainsencher, T. C. White, A. N. Korotkov, A. N. Cleland, and J. M. Martinis, “Catching Time-Reversed Microwave Coherent State Photons with 99.4% Absorption Efficiency,” *Physical Review Letters*, vol. 112, p. 210501, May 2014.
- [38] P. Magnard, S. Storz, P. Kurpiers, J. Schär, F. Marxer, J. Lütolf, T. Walter, J.-C. Besse, M. Gabureac, K. Reuer, A. Akin, B. Royer, A. Blais, and A. Wallraff, “Microwave Quantum Link between Superconducting Circuits Housed in Spatially Separated Cryogenic Systems,” *Physical Review Letters*, vol. 125, p. 260502, Dec. 2020.
- [39] K. Reuer, J.-C. Besse, L. Wernli, P. Magnard, P. Kurpiers, G. J. Norris, A. Wallraff, and C. Eichler, “Realization of a Universal Quantum Gate Set for Itinerant Microwave Photons,” *Physical Review X*, vol. 12, p. 011008, Jan. 2022.
- [40] J. L. O’Brien, A. Furusawa, and J. Vučković, “Photonic quantum technologies,” *Nature Photonics*, vol. 3, pp. 687–695, Dec. 2009.
- [41] N. J. Lambert, A. Rueda, F. Sedlmeir, and H. G. L. Schwefel, “Coherent Conversion Between Microwave and Optical Photons—An Overview of Physical Implementations,” *Advanced Quantum Technologies*, vol. 3, no. 1, p. 1900077, 2020.
- [42] N. Lauk, N. Sinclair, S. Barzanjeh, J. P. Covey, M. Saffman, M. Spiropulu, and C. Simon, “Perspectives on quantum transduction,” *Quantum Science and Technology*, vol. 5, p. 020501, Mar. 2020.
- [43] S. Wehner, D. Elkouss, and R. Hanson, “Quantum internet: A vision for the road ahead,” *Science*, vol. 362, Oct. 2018.
- [44] H. Gevorgyan, A. Khilo, Y. Ehrlichman, M. A. Popović, and M. A. Popović, “Triply resonant coupled-cavity electro-optic modulators for RF to optical signal conversion,” *Optics Express*, vol. 28, pp. 788–815, Jan. 2020.
- [45] T. Bagci, A. Simonsen, S. Schmid, L. G. Villanueva, E. Zeuthen, J. Appel, J. M. Taylor, A. Sørensen, K. Usami, A. Schliesser, and E. S. Polzik, “Optical detection of radio waves through a nanomechanical transducer,” *Nature*, vol. 507, pp. 81–85, Mar. 2014.
- [46] M. de Cea, E. E. Wollman, A. H. Atabaki, D. J. Gray, M. D. Shaw, and R. J. Ram, “Photonic Readout of Superconducting Nanowire Single Photon Counting Detectors,” *Scientific Reports*, vol. 10, p. 9470, June 2020.
- [47] E. Zeuthen, A. Schliesser, A. S. Sørensen, and J. M. Taylor, “Figures of merit for quantum transducers,” *Quantum Science and Technology*, vol. 5, p. 034009, May 2020.
- [48] A. H. Safavi-Naeini and O. Painter, “Proposal for an optomechanical traveling wave phonon–photon translator,” *New Journal of Physics*, vol. 13, no. 1, p. 013017, 2011.

- [49] X. Han, X. Han, W. Fu, C.-L. Zou, L. Jiang, H. X. Tang, and H. X. Tang, “Microwave-optical quantum frequency conversion,” *Optica*, vol. 8, pp. 1050–1064, Aug. 2021.
- [50] R. W. Andrews, R. W. Peterson, T. P. Purdy, K. Cicak, R. W. Simmonds, C. A. Regal, and K. W. Lehnert, “Bidirectional and efficient conversion between microwave and optical light,” *Nature Physics*, vol. 10, p. 321, Apr. 2014.
- [51] A. P. Higginbotham, P. S. Burns, M. D. Urmey, R. W. Peterson, N. S. Kampel, B. M. Brubaker, G. Smith, K. W. Lehnert, and C. A. Regal, “Harnessing electro-optic correlations in an efficient mechanical converter,” *Nature Physics*, vol. 14, pp. 1038–1042, Oct. 2018.
- [52] L. Midolo, A. Schliesser, and A. Fiore, “Nano-opto-electro-mechanical systems,” *Nature Nanotechnology*, vol. 13, pp. 11–18, Jan. 2018.
- [53] A. H. Safavi-Naeini, D. V. Thourhout, R. Baets, and R. V. Laer, “Controlling phonons and photons at the wavelength scale: Integrated photonics meets integrated photonics,” *Optica*, vol. 6, pp. 213–232, Feb. 2019.
- [54] J. Bochmann, A. Vainsencher, D. D. Awschalom, and A. N. Cleland, “Nanomechanical coupling between microwave and optical photons,” *Nature Physics*, vol. 9, pp. 712–716, Nov. 2013.
- [55] L. Fan, X. Sun, C. Xiong, C. Schuck, and H. X. Tang, “Aluminum nitride piezo-acousto-photonic crystal nanocavity with high quality factors,” *Applied Physics Letters*, vol. 102, p. 153507, Apr. 2013.
- [56] K. C. Balram, M. I. Davanço, J. D. Song, and K. Srinivasan, “Coherent coupling between radiofrequency, optical and acoustic waves in piezo-optomechanical circuits,” *Nature Photonics*, vol. 10, pp. 346–352, May 2016.
- [57] A. Vainsencher, K. J. Satzinger, G. A. Peairs, and A. N. Cleland, “Bi-directional conversion between microwave and optical frequencies in a piezoelectric optomechanical device,” *Applied Physics Letters*, vol. 109, p. 033107, July 2016.
- [58] W. Jiang, C. J. Sarabalis, Y. D. Dahmani, R. N. Patel, F. M. Mayor, T. P. McKenna, R. Van Laer, and A. H. Safavi-Naeini, “Efficient bidirectional piezo-optomechanical transduction between microwave and optical frequency,” *Nature Communications*, vol. 11, pp. 1–7, Mar. 2020.
- [59] M. Forsch, R. Stockill, A. Wallucks, I. Marinković, C. Gärtner, R. A. Norte, F. van Otten, A. Fiore, K. Srinivasan, and S. Gröblacher, “Microwave-to-optics conversion using a mechanical oscillator in its quantum ground state,” *Nature Physics*, vol. 16, pp. 69–74, Jan. 2020.
- [60] L. Shao, M. Yu, S. Maity, N. Sinclair, L. Zheng, C. Chia, A. Shams-Ansari, C. Wang, M. Zhang, K. Lai, and M. Lončar, “Microwave-to-optical conversion using lithium niobate thin-film acoustic resonators,” *Optica*, vol. 6, p. 1498, Dec. 2019.
- [61] X. Han, W. Fu, C. Zhong, C.-L. Zou, Y. Xu, A. A. Sayem, M. Xu, S. Wang, R. Cheng, L. Jiang, and H. X. Tang, “Cavity piezo-mechanics for superconducting-nanophotonic quantum interface,” *Nature Communications*, vol. 11, p. 3237, June 2020.

- [62] V. S. Ilchenko, A. A. Savchenkov, A. B. Matsko, and L. Maleki, “Whispering-gallery-mode electro-optic modulator and photonic microwave receiver,” *Journal of the Optical Society of America B*, vol. 20, p. 333, Feb. 2003.
- [63] D. V. Strekalov, A. A. Savchenkov, A. B. Matsko, and N. Yu, “Efficient upconversion of subterahertz radiation in a high-Q whispering gallery resonator,” *Optics Letters*, vol. 34, p. 713, Mar. 2009.
- [64] A. Rueda, F. Sedlmeir, M. C. Collodo, U. Vogl, B. Stiller, G. Schunk, D. V. Strekalov, C. Marquardt, J. M. Fink, O. Painter, G. Leuchs, and H. G. L. Schwefel, “Efficient microwave to optical photon conversion: An electro-optical realization,” *Optica*, vol. 3, pp. 597–604, June 2016.
- [65] J. D. Witmer, J. A. Valery, P. Arrangoiz-Arriola, C. J. Sarabalis, J. T. Hill, and A. H. Safavi-Naeini, “High-Q photonic resonators and electro-optic coupling using silicon-on-lithium-niobate,” *Scientific Reports*, vol. 7, Dec. 2017.
- [66] L. Fan, C.-L. Zou, R. Cheng, X. Guo, X. Han, Z. Gong, S. Wang, and H. X. Tang, “Superconducting cavity electro-optics: A platform for coherent photon conversion between superconducting and photonic circuits,” *Science Advances*, vol. 4, p. eaar4994, Aug. 2018.
- [67] J. D. Witmer, T. P. McKenna, W. Jiang, P. Arrangoiz-Arriola, E. A. Wollack, R. Van Laer, and A. H. Safavi-Naeini, “On-Chip Microwave-to-Optical Photon Conversion for Quantum Networks,” in *Quantum Information and Measurement (QIM) V: Quantum Technologies*, (Rome), p. T5A.10, OSA, 2019.
- [68] T. Vogt, C. Gross, J. Han, S. B. Pal, M. Lam, M. Kiffner, and W. Li, “Efficient microwave-to-optical conversion using Rydberg atoms,” *Physical Review A*, vol. 99, p. 023832, Feb. 2019.
- [69] J. Han, T. Vogt, C. Gross, D. Jaksch, M. Kiffner, and W. Li, “Coherent Microwave-to-Optical Conversion via Six-Wave Mixing in Rydberg Atoms,” *Physical Review Letters*, vol. 120, p. 093201, Mar. 2018.
- [70] X. Fernandez-Gonzalvo, Y.-H. Chen, C. Yin, S. Rogge, and J. J. Longdell, “Coherent frequency up-conversion of microwaves to the optical telecommunications band in an Er:YSO crystal,” *Physical Review A*, vol. 92, p. 062313, Dec. 2015.
- [71] J. G. Bartholomew, J. Rochman, T. Xie, J. M. Kindem, A. Ruskuc, I. Craiciu, M. Lei, and A. Faraon, “On-chip coherent microwave-to-optical transduction mediated by ytterbium in YVO 4,” *Nature Communications*, vol. 11, p. 3266, June 2020.
- [72] R. Hisatomi, A. Osada, Y. Tabuchi, T. Ishikawa, A. Noguchi, R. Yamazaki, K. Usami, and Y. Nakamura, “Bidirectional conversion between microwave and light via ferromagnetic magnons,” *Physical Review B*, vol. 93, p. 174427, May 2016.
- [73] M. Mirhosseini, A. Sipahigil, M. Kalaei, and O. Painter, “Superconducting qubit to optical photon transduction,” *Nature*, vol. 588, pp. 599–603, Dec. 2020.

- [74] S. M. Meenehan, J. D. Cohen, S. Gröblacher, J. T. Hill, A. H. Safavi-Naeini, M. Aspelmeyer, and O. Painter, “Silicon optomechanical crystal resonator at millikelvin temperatures,” *Physical Review A*, vol. 90, July 2014.
- [75] S. M. Meenehan, J. D. Cohen, G. S. MacCabe, F. Marsili, M. D. Shaw, and O. Painter, “Pulsed Excitation Dynamics of an Optomechanical Crystal Resonator near Its Quantum Ground State of Motion,” *Physical Review X*, vol. 5, Oct. 2015.
- [76] M. Tsang, “Cavity quantum electro-optics,” *Physical Review A*, vol. 81, p. 063837, June 2010.
- [77] M. Tsang, “Cavity quantum electro-optics. II. Input-output relations between traveling optical and microwave fields,” *Physical Review A*, vol. 84, Oct. 2011.
- [78] C. Javerzac-Galy, K. Plekhanov, N. R. Bernier, L. D. Toth, A. K. Feofanov, and T. J. Kippenberg, “On-chip microwave-to-optical quantum coherent converter based on a superconducting resonator coupled to an electro-optic microresonator,” *Physical Review A*, vol. 94, Nov. 2016.
- [79] J. D. Witmer, T. P. McKenna, P. Arrangoiz-Arriola, R. V. Laer, E. A. Wollack, F. Lin, A. K.-Y. Jen, J. Luo, and A. H. Safavi-Naeini, “A silicon-organic hybrid platform for quantum microwave-to-optical transduction,” *Quantum Science and Technology*, vol. 5, p. 034004, Apr. 2020.
- [80] A. B. Matsko, L. Maleki, A. A. Savchenkov, and V. S. Ilchenko, “Whispering gallery mode based optoelectronic microwave oscillator,” *Journal of Modern Optics*, vol. 50, pp. 2523–2542, Oct. 2003.
- [81] S. Harris, “Tunable optical parametric oscillators,” *Proceedings of the IEEE*, vol. 57, pp. 2096–2113, Dec. 1969.
- [82] J. M. Dobrindt and T. J. Kippenberg, “Theoretical Analysis of Mechanical Displacement Measurement Using a Multiple Cavity Mode Transducer,” *Physical Review Letters*, vol. 104, Jan. 2010.
- [83] M. Soltani, M. Zhang, C. Ryan, G. J. Ribeill, C. Wang, and M. Loncar, “Efficient quantum microwave-to-optical conversion using electro-optic nanophotonic coupled resonators,” *Physical Review A*, vol. 96, p. 043808, Oct. 2017.
- [84] W. Hease, A. Rueda, R. Sahu, M. Wulf, G. Arnold, H. G. L. Schwefel, and J. M. Fink, “Cavity quantum electro-optics: Microwave-telecom conversion in the quantum ground state,” *arXiv:2005.12763 [physics, physics:quant-ph]*, May 2020.
- [85] S. Mobassem, N. J. Lambert, A. Rueda, J. M. Fink, G. Leuchs, and H. G. L. Schwefel, “Thermal noise in electro-optic devices at cryogenic temperatures,” *Quantum Science and Technology*, vol. 6, p. 045005, July 2021.
- [86] W. Fu, M. Xu, X. Liu, C.-L. Zou, C. Zhong, X. Han, M. Shen, Y. Xu, R. Cheng, S. Wang, L. Jiang, and H. X. Tang, “Cavity electro-optic circuit for microwave-to-optical conversion in the quantum ground state,” *Physical Review A*, vol. 103, p. 053504, May 2021.

- [87] R. Sahu, W. Hease, A. Rueda, G. Arnold, L. Qiu, and J. M. Fink, “Quantum-enabled operation of a microwave-optical interface,” *Nature Communications*, vol. 13, p. 1276, Mar. 2022.
- [88] Liu Qiu, Rishabh Sahu, William Hease, Georg Arnold, and Johannes Fink, “Dynamical Control in Cavity Electro-Optics,” in *Bulletin of the American Physical Society, 2022*, (Chicago), Mar. 2022.
- [89] V. S. Ilchenko, A. A. Savchenkov, A. B. Matsko, and L. Maleki, “Nonlinear optics and crystalline whispering gallery mode cavities,” *Physical review letters*, vol. 92, no. 4, p. 043903, 2004.
- [90] Y. Xu, A. A. Sayem, L. Fan, C.-L. Zou, S. Wang, R. Cheng, W. Fu, L. Yang, M. Xu, and H. X. Tang, “Bidirectional interconversion of microwave and light with thin-film lithium niobate,” *Nature Communications*, vol. 12, p. 4453, July 2021.
- [91] J. D. Witmer, T. P. McKenna, P. Arrangoiz-Arriola, R. Van Laer, E. A. Wollack, F. Lin, A. K.-Y. Jen, J. Luo, and A. H. Safavi-Naeini, “A silicon-organic hybrid platform for quantum microwave-to-optical transduction,” *arXiv:1912.10346 [physics, physics:quant-ph]*, Dec. 2019.
- [92] J. Holzgrafe, N. Sinclair, N. Sinclair, D. Zhu, D. Zhu, A. Shams-Ansari, M. Colangelo, Y. Hu, Y. Hu, M. Zhang, M. Zhang, K. K. Berggren, and M. Lončar, “Cavity electro-optics in thin-film lithium niobate for efficient microwave-to-optical transduction,” *Optica*, vol. 7, pp. 1714–1720, Dec. 2020.
- [93] T. P. McKenna, T. P. McKenna, J. D. Witmer, J. D. Witmer, R. N. Patel, W. Jiang, R. V. Laer, P. Arrangoiz-Arriola, E. A. Wollack, J. F. Herrmann, and A. H. Safavi-Naeini, “Cryogenic microwave-to-optical conversion using a triply resonant lithium-niobate-on-sapphire transducer,” *Optica*, vol. 7, pp. 1737–1745, Dec. 2020.
- [94] D. Zhu, L. Shao, M. Yu, R. Cheng, B. Desiatov, C. J. Xin, Y. Hu, J. Holzgrafe, S. Ghosh, A. Shams-Ansari, E. Puma, N. Sinclair, N. Sinclair, C. Reimer, M. Zhang, and M. Lončar, “Integrated photonics on thin-film lithium niobate,” *Advances in Optics and Photonics*, vol. 13, pp. 242–352, June 2021.
- [95] E. Wooten, K. Kissa, A. Yi-Yan, E. Murphy, D. Lafaw, P. Hallemeier, D. Maack, D. Atanasio, D. Fritz, G. McBrien, and D. Bossi, “A review of lithium niobate modulators for fiber-optic communications systems,” *IEEE Journal of Selected Topics in Quantum Electronics*, vol. 6, pp. 69–82, Jan. 2000.
- [96] M. Bruel, “Silicon on insulator material technology,” *Electronics Letters*, vol. 31, pp. 1201–1202, July 1995.
- [97] M. Levy, R. M. Osgood, R. Liu, L. E. Cross, G. S. Cargill, A. Kumar, and H. Bakhru, “Fabrication of single-crystal lithium niobate films by crystal ion slicing,” *Applied Physics Letters*, vol. 73, pp. 2293–2295, Oct. 1998.
- [98] L. Cai, Y. Wang, and H. Hu, “Low-loss waveguides in a single-crystal lithium niobate thin film,” *Optics Letters*, vol. 40, pp. 3013–3016, July 2015.

- [99] A. Rao, A. Patil, J. Chiles, M. Malinowski, S. Novak, K. Richardson, P. Rabiei, and S. Fathpour, “Heterogeneous microring and Mach-Zehnder modulators based on lithium niobate and chalcogenide glasses on silicon,” *Optics Express*, vol. 23, pp. 22746–22752, Aug. 2015.
- [100] R. Wu, M. Wang, J. Xu, J. Qi, W. Chu, Z. Fang, J. Zhang, J. Zhou, L. Qiao, Z. Chai, J. Lin, and Y. Cheng, “Long Low-Loss-Litium Niobate on Insulator Waveguides with Sub-Nanometer Surface Roughness,” *Nanomaterials*, vol. 8, p. 910, Nov. 2018.
- [101] H. Hu, A. P. Milenin, R. B. Wehrspohn, H. Hermann, and W. Sohler, “Plasma etching of proton-exchanged lithium niobate,” *Journal of Vacuum Science & Technology A*, vol. 24, pp. 1012–1015, July 2006.
- [102] F. Chen, “Photonic guiding structures in lithium niobate crystals produced by energetic ion beams,” *Journal of Applied Physics*, vol. 106, p. 081101, Oct. 2009.
- [103] C. Wang, M. Zhang, X. Chen, M. Bertrand, A. Shams-Ansari, S. Chandrasekhar, P. Winzer, and M. Lončar, “Integrated lithium niobate electro-optic modulators operating at CMOS-compatible voltages,” *Nature*, vol. 562, p. 101, Oct. 2018.
- [104] H. Nagata, N. Mitsugi, K. Shima, M. Tamai, and E. M. Haga, “Growth of crystalline LiF on CF₄ plasma etched LiNbO₃ substrates,” *Journal of Crystal Growth*, vol. 187, pp. 573–576, May 1998.
- [105] M. Zhang, C. Wang, R. Cheng, A. Shams-Ansari, and M. Lončar, “Monolithic ultra-high-Q lithium niobate microring resonator,” *Optica*, vol. 4, pp. 1536–1537, Dec. 2017.
- [106] M. Zhang, B. Buscaino, C. Wang, A. Shams-Ansari, C. Reimer, R. Zhu, J. M. Kahn, and M. Lončar, “Broadband electro-optic frequency comb generation in a lithium niobate microring resonator,” *Nature*, vol. 568, pp. 373–377, Apr. 2019.
- [107] J. Lu, J. B. Surya, X. Liu, A. W. Bruch, Z. Gong, Y. Xu, and H. X. Tang, “Periodically poled thin-film lithium niobate microring resonators with a second-harmonic generation efficiency of 250,000%/W,” *Optica*, vol. 6, pp. 1455–1460, Dec. 2019.
- [108] L. Shao, S. Maity, L. Zheng, L. Wu, A. Shams-Ansari, Y.-I. Sohn, E. Puma, M. Gadalla, M. Zhang, C. Wang, E. Hu, K. Lai, and M. Lončar, “Phononic Band Structure Engineering for High-Q Gigahertz Surface Acoustic Wave Resonators on Lithium Niobate,” *Physical Review Applied*, vol. 12, p. 014022, July 2019.
- [109] T. I. Fossen and H. Nijmeijer, eds., *Parametric Resonance in Dynamical Systems*. Springer, 2012th edition ed., Dec. 2011.
- [110] M. Aspelmeyer, T. J. Kippenberg, and F. Marquardt, “Cavity optomechanics,” *Reviews of Modern Physics*, vol. 86, pp. 1391–1452, Dec. 2014.
- [111] D. Lachance-Quirion, Y. Tabuchi, A. Gloppe, K. Usami, and Y. Nakamura, “Hybrid quantum systems based on magnonics,” *Applied Physics Express*, vol. 12, p. 070101, June 2019.
- [112] P. Kinsler and P. D. Drummond, “Quantum dynamics of the parametric oscillator,” *Physical Review A*, vol. 43, pp. 6194–6208, June 1991.

- [113] C. M. Caves, “Quantum-mechanical noise in an interferometer,” *Physical Review D*, vol. 23, pp. 1693–1708, Apr. 1981.
- [114] A. B. Matsko, A. A. Savchenkov, V. S. Ilchenko, D. Seidel, and L. Maleki, “On fundamental quantum noises of whispering gallery mode electro-optic modulators,” *Optics Express*, vol. 15, pp. 17401–17409, Dec. 2007.
- [115] A. Guarino, G. Poberaj, D. Rezzonico, R. Degl’Innocenti, and P. Günter, “Electro-optically tunable microring resonators in lithium niobate,” *Nature Photonics*, vol. 1, pp. 407–410, July 2007.
- [116] A. Honardoost, R. Safian, A. Rao, and S. Fathpour, “High-Speed Modeling of Ultracompact Electrooptic Modulators,” *Journal of Lightwave Technology*, vol. 36, pp. 5893–5902, Dec. 2018.
- [117] J.-m. Liu, *Photonic Devices*. Cambridge: Cambridge University Press, 2005.
- [118] J. A. Armstrong, N. Bloembergen, J. Ducuing, and P. S. Pershan, “Interactions between Light Waves in a Nonlinear Dielectric,” *Physical Review*, vol. 127, pp. 1918–1939, Sept. 1962.
- [119] H. A. Haus, *Electromagnetic Noise and Quantum Optical Measurements*. Springer, soft-cover version of original hardcover edition 2000 ed., Dec. 2012.
- [120] A. Rueda, W. Hease, S. Barzanjeh, and J. M. Fink, “Electro-optic entanglement source for microwave to telecom quantum state transfer,” *npj Quantum Information*, vol. 5, pp. 1–11, Nov. 2019.
- [121] C. W. Gardiner and M. J. Collett, “Input and output in damped quantum systems: Quantum stochastic differential equations and the master equation,” *Physical Review A*, vol. 31, pp. 3761–3774, June 1985.
- [122] A. Yariv, “Universal relations for coupling of optical power between microresonators and dielectric waveguides,” *Electronics Letters*, vol. 36, pp. 321–322, Feb. 2000.
- [123] M. Zhang, C. Wang, Y. Hu, b, T. Ren, S. Fan, and M. Lončar, “Electronically programmable photonic molecule,” *Nature Photonics*, vol. 13, pp. 36–40, Jan. 2019.
- [124] C. Wang, M. Zhang, M. Yu, R. Zhu, H. Hu, and M. Loncar, “Monolithic lithium niobate photonic circuits for Kerr frequency comb generation and modulation,” *Nature Communications*, vol. 10, Dec. 2019.
- [125] A. E. Dane, A. N. McCaughan, D. Zhu, Q. Zhao, C.-S. Kim, N. Calandri, A. Agarwal, F. Bellei, and K. K. Berggren, “Bias sputtered NbN and superconducting nanowire devices,” *Applied Physics Letters*, vol. 111, p. 122601, Sept. 2017.
- [126] M. Scigliuzzo, L. E. Bruhat, A. Bengtsson, J. J. Burnett, A. F. Roudsari, and P. Delsing, “Phononic loss in superconducting resonators on piezoelectric substrates,” *New Journal of Physics*, vol. 22, p. 053027, May 2020.

- [127] A. D. O’Connell, M. Ansmann, R. C. Bialczak, M. Hofheinz, N. Katz, E. Lucero, C. McKenney, M. Neeley, H. Wang, E. M. Weig, A. N. Cleland, and J. M. Martinis, “Microwave dielectric loss at single photon energies and millikelvin temperatures,” *Applied Physics Letters*, vol. 92, p. 112903, Mar. 2008.
- [128] P. Günter and J.-P. Huignard, eds., *Photorefractive Materials and Their Applications 1: Basic Effects*. No. 113 in Springer Series in Optical Sciences, New York, NY: Springer, 2006.
- [129] H. Jiang, R. Luo, H. Liang, X. Chen, Y. Chen, and Q. Lin, “Fast response of photorefraction in lithium niobate microresonators,” *Optics Letters*, vol. 42, p. 3267, Sept. 2017.
- [130] M. Li, H. Liang, R. Luo, Y. He, J. Ling, and Q. Lin, “Photon-level tuning of photonic nanocavities,” *Optica*, vol. 6, pp. 860–863, July 2019.
- [131] B. Abdo, E. Segev, O. Shtempluck, and E. Buks, “Nonlinear dynamics in the resonance line shape of NbN superconducting resonators,” *Physical Review B*, vol. 73, p. 134513, Apr. 2006.
- [132] J. M. Fink, M. Kalaei, A. Pitanti, R. Norte, L. Heinzle, M. Davanço, K. Srinivasan, and O. Painter, “Quantum electromechanics on silicon nitride nanomembranes,” *Nature Communications*, vol. 7, p. 12396, Aug. 2016.
- [133] J. Zmuidzinas, “Superconducting Microresonators: Physics and Applications,” *Annual Review of Condensed Matter Physics*, vol. 3, no. 1, pp. 169–214, 2012.
- [134] M. Li, J. Ling, Y. He, U. A. Javid, S. Xue, and Q. Lin, “Lithium niobate photonic-crystal electro-optic modulator,” *Nature Communications*, vol. 11, p. 4123, Aug. 2020.
- [135] M. Xu, M. He, H. Zhang, J. Jian, Y. Pan, X. Liu, L. Chen, X. Meng, H. Chen, Z. Li, X. Xiao, S. Yu, S. Yu, and X. Cai, “High-performance coherent optical modulators based on thin-film lithium niobate platform,” *Nature Communications*, vol. 11, p. 3911, Aug. 2020.
- [136] S. Sun, M. He, M. Xu, S. Gao, Z. Chen, X. Zhang, Z. Ruan, X. Wu, L. Zhou, L. Liu, C. Lu, C. Guo, L. Liu, S. Yu, and X. Cai, “Bias-drift-free Mach–Zehnder modulators based on a heterogeneous silicon and lithium niobate platform,” *Photonics Research*, vol. 8, p. 1958, Dec. 2020.
- [137] S. Yamada and M. Minakata, “DC Drift Phenomena in LiNbO₃ Optical Waveguide Devices,” *Japanese Journal of Applied Physics*, vol. 20, pp. 733–737, Apr. 1981.
- [138] C. M. Gee, G. D. Thurmond, H. Blauvelt, and H. W. Yen, “Minimizing dc drift in LiNbO₃ waveguide devices,” *Applied Physics Letters*, vol. 47, pp. 211–213, Aug. 1985.
- [139] R. A. Becker, “Circuit effect in LiNbO₃ channel-waveguide modulators,” *Optics Letters*, vol. 10, p. 417, Aug. 1985.
- [140] H. Nagata, “Progress and problems in reliability of Ti:LiNbO₃ optical intensity modulators,” *Optical Engineering*, vol. 34, p. 3284, Nov. 1995.

- [141] H. Nagata, J. Ichikawa, N. Mitsugi, T. Sakamoto, T. Shinriki, H. Honda, and M. Kobayashi, “Improved Long-Term DC Drift in OH-Reduced Lithium Niobate Optical Intensity Modulators,” *Applied Optics*, vol. 35, p. 6828, Dec. 1996.
- [142] J. P. Salvestrini, L. Guilbert, M. Fontana, M. Abarkan, and S. Gille, “Analysis and Control of the DC Drift in LiNbO₃ Based Mach–Zehnder Modulators,” *Journal of Lightwave Technology*, vol. 29, pp. 1522–1534, May 2011.
- [143] H. Park, W.-Y. Hwang, and J.-J. Kim, “Origin of direct current drift in electro-optic polymer modulator,” *Applied Physics Letters*, vol. 70, pp. 2796–2798, May 1997.
- [144] H. Zhang, *Linear and Non-Linear Electro-optics in a Semiconductor*. PhD thesis, University of Colorado, 2012.
- [145] J. Holzgrafe, N. Sinclair, N. Sinclair, D. Zhu, D. Zhu, A. Shams-Ansari, M. Colangelo, Y. Hu, M. Zhang, M. Zhang, K. K. Berggren, and M. Loncar, “Toward Efficient Microwave-Optical Transduction using Cavity Electro-Optics in Thin-Film Lithium Niobate,” in *Conference on Lasers and Electro-Optics (2020), Paper FTh4D.5*, p. FTh4D.5, Optical Society of America, May 2020.
- [146] T. Granzow, “Polaron-mediated low-frequency dielectric anomaly in reduced LiNbO₃:Ti,” *Applied Physics Letters*, vol. 111, p. 022903, July 2017.
- [147] Andrew Jonscher, “Dielectric Relaxation in solids,” *Journal of Physics D: Applied Physics*, vol. 32, p. R57, 1999.
- [148] A. Youssefi, I. Shomroni, Y. J. Joshi, N. R. Bernier, A. Lukashchuk, P. Uhrich, L. Qiu, and T. J. Kippenberg, “A cryogenic electro-optic interconnect for superconducting devices,” *Nature Electronics*, vol. 4, pp. 326–332, May 2021.
- [149] A. M. Glass, K. Nassau, and T. J. Negran, “Ionic conductivity of quenched alkali niobate and tantalate glasses,” *Journal of Applied Physics*, vol. 49, pp. 4808–4811, Sept. 1978.
- [150] Y. Xu, A. A. Sayem, C.-L. Zou, L. Fan, R. Cheng, and H. X. Tang, “Photorefractive-induced Bragg scattering in cryogenic lithium niobate ring resonators,” *Optics Letters*, vol. 46, p. 432, Jan. 2021.
- [151] Y. Xu, M. Shen, J. Lu, J. B. Surya, A. A. Sayem, and H. X. Tang, “Mitigating photorefractive effect in thin-film lithium niobate microring resonators,” *Optics Express*, vol. 29, pp. 5497–5504, Feb. 2021.
- [152] H. Jhans, J. M. Honig, and C. N. R. Rao, “Optical properties of reduced LiNbO₃,” *Journal of Physics C: Solid State Physics*, vol. 19, pp. 3649–3658, July 1986.
- [153] P. F. Bordui, D. H. Jundt, E. M. Standifer, R. G. Norwood, R. L. Sawin, and J. D. Galipeau, “Chemically reduced lithium niobate single crystals: Processing, properties and improved surface acoustic wave device fabrication and performance,” *Journal of Applied Physics*, vol. 85, pp. 3766–3769, Apr. 1999.

- [154] S. Jen and R. Bobkowsky, “Black lithium niobate SAW device fabrication and performance evaluation,” in *2000 IEEE Ultrasonics Symposium. Proceedings. An International Symposium (Cat. No.00CH37121)*, vol. 1, pp. 269–273 vol.1, Oct. 2000.
- [155] O. F. Schirmer, M. Imlau, C. Merschjann, and B. Schoke, “Electron small polarons and bipolarons in LiNbO_3 ,” *Journal of Physics: Condensed Matter*, vol. 21, p. 123201, Mar. 2009.
- [156] I. Idris and O. Sugiura, “Film Characteristics of Low-Temperature Plasma-Enhanced Chemical Vapor Deposition Silicon Dioxide Using Tetraisocyanatesilane and Oxygen,” *Japanese Journal of Applied Physics*, vol. 37, pp. 6562–6568, Dec. 1998.
- [157] A. Shams-Ansari, G. Huang, L. He, L. He, M. Churaev, P. Kharel, Z. Tan, J. Holzgrafe, R. Cheng, D. Zhu, J. Liu, B. Desiatov, M. Zhang, M. Zhang, T. J. Kippenberg, and M. Lončar, “Probing the Limits of Optical Loss in Ion-Sliced Thin-film Lithium Niobate,” in *Conference on Lasers and Electro-Optics (2021), Paper STh4J.4*, p. STh4J.4, Optica Publishing Group, May 2021.
- [158] D. Sugak, Y. Zhydachevskii, Y. Sugak, O. Buryy, S. Ubizskii, I. Solskii, M. Schrader, and K.-D. Becker, “*In Situ* investigation of optical absorption changes in LiNbO_3 during reducing/oxidizing high-temperature treatments,” *Journal of Physics: Condensed Matter*, vol. 19, p. 086211, Feb. 2007.
- [159] T. Volk and M. Wöhlecke, *Lithium Niobate: Defects, Photorefraction and Ferroelectric Switching*. No. 115 in Springer Series in Materials Science, Berlin: Springer, 2008.
- [160] M. Seino, T. Nakazawa, T. Yamane, Y. Kubota, M. Doi, K. Sugeta, and T. Kurahashi, “Optical waveguide device,” Apr. 1995.
- [161] M. H. P. Pfeiffer, J. Liu, M. Geiselmann, and T. J. Kippenberg, “Coupling Ideality of Integrated Planar High-Q Microresonators,” *Physical Review Applied*, vol. 7, p. 024026, Feb. 2017.
- [162] A. Biberman, E. Timurdogan, W. A. Zortman, D. C. Trotter, and M. R. Watts, “Adiabatic microring modulators,” *Optics Express*, vol. 20, pp. 29223–29236, Dec. 2012.
- [163] Q. Li, A. A. Eftekhari, Z. Xia, and A. Adibi, “Unified approach to mode splitting and scattering loss in high-Q whispering-gallery-mode microresonators,” *Physical Review A*, vol. 88, p. 033816, Sept. 2013.
- [164] S. Meesala, J. Banker, S. Wood, A. Sipahigil, D. Lake, P. Chiappina, A. Beyer, M. Shaw, O. Painter, and O. Painter, “Effects of Laser Illumination on Superconducting Circuits for Quantum Transduction,” in *Conference on Lasers and Electro-Optics (2021), Paper FTh2P.7*, p. FTh2P.7, Optica Publishing Group, May 2021.
- [165] C. Macklin, K. O’Brien, D. Hover, M. E. Schwartz, V. Bolkhovskiy, X. Zhang, W. D. Oliver, and I. Siddiqi, “A near-quantum-limited Josephson traveling-wave parametric amplifier,” *Science*, vol. 350, pp. 307–310, Oct. 2015.
- [166] F. Lecocq, F. Quinlan, K. Cicak, J. Aumentado, S. A. Diddams, and J. D. Teufel, “Control and readout of a superconducting qubit using a photonic link,” *Nature*, vol. 591, pp. 575–579, Mar. 2021.

- [167] S. Krastanov, H. Raniwala, J. Holzgrafe, K. Jacobs, M. Lončar, M. J. Reagor, and D. R. Englund, “Optically Heralded Entanglement of Superconducting Systems in Quantum Networks,” *Physical Review Letters*, vol. 127, p. 040503, July 2021.
- [168] J. Wu, C. Cui, L. Fan, and Q. Zhuang, “Deterministic Microwave-Optical Transduction Based on Quantum Teleportation,” *Physical Review Applied*, vol. 16, p. 064044, Dec. 2021.
- [169] P. C. Humphreys, N. Kalb, J. P. J. Morits, R. N. Schouten, R. F. L. Vermeulen, D. J. Twitchen, M. Markham, and R. Hanson, “Deterministic delivery of remote entanglement on a quantum network,” *Nature*, vol. 558, pp. 268–273, June 2018.
- [170] M. Pompili, S. L. N. Hermans, S. Baier, H. K. C. Beukers, P. C. Humphreys, R. N. Schouten, R. F. L. Vermeulen, M. J. Tiggelman, L. dos Santos Martins, B. Dirkse, S. Wehner, and R. Hanson, “Realization of a multinode quantum network of remote solid-state qubits,” *Science*, vol. 372, pp. 259–264, Apr. 2021.
- [171] P. Kurpiers, P. Magnard, T. Walter, B. Royer, M. Pechal, J. Heinsoo, Y. Salathé, A. Akin, S. Storz, J.-C. Besse, S. Gasparinetti, A. Blais, and A. Wallraff, “Deterministic quantum state transfer and remote entanglement using microwave photons,” *Nature*, vol. 558, pp. 264–267, June 2018.
- [172] P. Campagne-Ibarcq, E. Zolys-Geller, A. Narla, S. Shankar, P. Reinhold, L. D. Burkhardt, C. J. Axline, W. Pfaff, L. Frunzio, R. J. Schoelkopf, and M. H. Devoret, “Deterministic remote entanglement of superconducting circuits through microwave two-photon transitions,” *Physical Review Letters*, vol. 120, p. 200501, May 2018.
- [173] M. Piekarek, D. Bonneau, S. Miki, T. Yamashita, M. Fujiwara, M. Sasaki, H. Terai, M. G. Tanner, C. M. Natarajan, R. H. Hadfield, J. L. O’Brien, and M. G. Thompson, “High-extinction ratio integrated photonic filters for silicon quantum photonics,” *Optics Letters*, vol. 42, p. 815, Feb. 2017.
- [174] W. Hease, A. Rueda, R. Sahu, M. Wulf, G. Arnold, H. G. Schwefel, and J. M. Fink, “Bidirectional Electro-Optic Wavelength Conversion in the Quantum Ground State,” *PRX Quantum*, vol. 1, p. 020315, Nov. 2020.
- [175] M. Xu, X. Han, C.-L. Zou, W. Fu, Y. Xu, C. Zhong, L. Jiang, and H. X. Tang, “Radiative cooling of a superconducting resonator,” *Physical Review Letters*, vol. 124, p. 033602, Jan. 2020.
- [176] J. M. Kreikebaum, A. Dove, W. Livingston, E. Kim, and I. Siddiqi, “Optimization of infrared and magnetic shielding of superconducting TiN and Al coplanar microwave resonators,” *Superconductor Science and Technology*, vol. 29, p. 104002, Aug. 2016.
- [177] C. J. Axline, L. D. Burkhardt, W. Pfaff, M. Zhang, K. Chou, P. Campagne-Ibarcq, P. Reinhold, L. Frunzio, S. M. Girvin, L. Jiang, M. H. Devoret, and R. J. Schoelkopf, “On-demand quantum state transfer and entanglement between remote microwave cavity memories,” *Nature Physics*, vol. 14, pp. 705–710, July 2018.

- [178] P. Kurpiers, P. Magnard, T. Walter, B. Royer, M. Pechal, J. Heinsoo, Y. Salathé, A. Akin, S. Storz, J.-C. Besse, S. Gasparinetti, A. Blais, and A. Wallraff, “Deterministic quantum state transfer and remote entanglement using microwave photons,” *Nature*, vol. 558, pp. 264–267, June 2018.
- [179] E. A. Dauler, M. E. Grein, A. J. Kerman, F. Marsili, S. Miki, S. W. Nam, M. D. Shaw, H. Terai, V. B. Verma, and T. Yamashita, “Review of superconducting nanowire single-photon detector system design options and demonstrated performance,” *Optical Engineering*, vol. 53, p. 081907, June 2014.
- [180] R. Riedinger, A. Wallucks, I. Marinković, C. Löschnauer, M. Aspelmeyer, S. Hong, and S. Gröblacher, “Remote quantum entanglement between two micromechanical oscillators,” *Nature*, vol. 556, pp. 473–477, Apr. 2018.
- [181] S. D. Barrett and P. Kok, “Efficient high-fidelity quantum computation using matter qubits and linear optics,” *Physical Review A*, vol. 71, p. 060310, June 2005.
- [182] E. T. Campbell and S. C. Benjamin, “Measurement-Based Entanglement under Conditions of Extreme Photon Loss,” *Physical Review Letters*, vol. 101, p. 130502, Sept. 2008.
- [183] D. Hucul, I. V. Inlek, G. Vittorini, C. Crocker, S. Debnath, S. M. Clark, and C. Monroe, “Modular entanglement of atomic qubits using photons and phonons,” *Nature Physics*, vol. 11, pp. 37–42, Jan. 2015.
- [184] N. Kalb, A. A. Reiserer, P. C. Humphreys, J. J. W. Bakermans, S. J. Kamerling, N. H. Nickerson, S. C. Benjamin, D. J. Twitchen, M. Markham, and R. Hanson, “Entanglement distillation between solid-state quantum network nodes,” *Science*, vol. 356, pp. 928–932, June 2017.
- [185] R. Riedinger, S. Hong, R. A. Norte, J. A. Slater, J. Shang, A. G. Krause, V. Anant, M. Aspelmeyer, and S. Gröblacher, “Non-classical correlations between single photons and phonons from a mechanical oscillator,” *Nature*, vol. 530, pp. 313–316, Feb. 2016.
- [186] D. Bozyigit, C. Lang, L. Steffen, J. M. Fink, C. Eichler, M. Baur, R. Bianchetti, P. J. Leek, S. Filipp, M. P. da Silva, A. Blais, and A. Wallraff, “Antibunching of microwave-frequency photons observed in correlation measurements using linear detectors,” *Nature Physics*, vol. 7, pp. 154–158, Feb. 2011.
- [187] J. Aumentado, “Superconducting Parametric Amplifiers: The State of the Art in Josephson Parametric Amplifiers,” *IEEE Microwave Magazine*, vol. 21, pp. 45–59, Aug. 2020.
- [188] Y. Hu, M. Yu, D. Zhu, N. Sinclair, A. Shams-Ansari, L. Shao, J. Holzgrafe, E. Puma, M. Zhang, and M. Lončar, “On-chip electro-optic frequency shifters and beam splitters,” *Nature*, vol. 599, pp. 587–593, Nov. 2021.
- [189] K. Borkje, A. Nunnenkamp, and S. M. Girvin, “Proposal for entangling remote micromechanical oscillators via optical measurements,” *arXiv:1103.2368 [cond-mat, physics:quant-ph]*, Sept. 2011.

- [190] M. Aspelmeyer, T. J. Kippenberg, and F. Marquardt, “Cavity optomechanics,” *Reviews of Modern Physics*, vol. 86, pp. 1391–1452, Dec. 2014.
- [191] O. Noroozian, P. K. Day, B. H. Eom, H. G. Leduc, and J. Zmuidzinas, “Crosstalk Reduction for Superconducting Microwave Resonator Arrays,” *IEEE Transactions on Microwave Theory and Techniques*, vol. 60, pp. 1235–1243, May 2012.
- [192] “Sonnet Software Inc.” <http://www.sonnetsoftware.com/>.
- [193] X. Ji, F. A. S. Barbosa, S. P. Roberts, A. Dutt, J. Cardenas, Y. Okawachi, A. Bryant, A. L. Gaeta, and M. Lipson, “Ultra-low-loss on-chip resonators with sub-milliwatt parametric oscillation threshold,” *Optica*, vol. 4, pp. 619–624, June 2017.